



# Hierarchical structured Ti-doped CeO<sub>2</sub> stabilized CoMn<sub>2</sub>O<sub>4</sub> for enhancing the low-temperature NH<sub>3</sub>-SCR performance within highly H<sub>2</sub>O and SO<sub>2</sub> resistance

Ning Luo <sup>a</sup>, Fengyu Gao <sup>a,\*</sup>, Hengheng Liu <sup>a</sup>, Tingkai Xiong <sup>a</sup>, Jiajun Wen <sup>a</sup>, Erhong Duan <sup>b</sup>, Chengzhi Wang <sup>c</sup>, Shunzheng Zhao <sup>a</sup>, Honghong Yi <sup>a</sup>, Xiaolong Tang <sup>a,\*</sup>

<sup>a</sup> Beijing Key Laboratory of Resource-oriented Treatment of Industrial Pollutants, School of Energy and Environmental Engineering, University of Science and Technology Beijing, Beijing 100083, PR China

<sup>b</sup> School of Environmental Science and Engineering, Hebei University of Science and Technology, Shijiazhuang, Hebei 050018, PR China

<sup>c</sup> Institute of Chemistry, Henan Academy of Sciences, Zhengzhou, Henan 450046, PR China



## ARTICLE INFO

### Keywords:

Low-temperature SCR  
Supported catalyst  
CoMn<sub>2</sub>O<sub>4</sub> spinel  
CeTiO<sub>x</sub> lamellar  
SO<sub>2</sub> resistance mechanism

## ABSTRACT

Developing effective and stable catalysts for low-temperature selective catalytic reduction (SCR) of NO<sub>x</sub> remains challenging. Herein, we constructed a hierarchical structure by loading CoMn<sub>2</sub>O<sub>4</sub> onto Ti-doped CeO<sub>2</sub>, that CoMn<sub>2</sub>O<sub>4</sub>/CeTiO<sub>x</sub> catalyst has shown superior deNO<sub>x</sub> activity (>95% at 100–225 °C), prominent reaction activation energy (28.8 ± 0.9 kJ mol<sup>-1</sup>) and outstanding stability (>75% at 100–200 °C within H<sub>2</sub>O and SO<sub>2</sub>). The “low-temperature active sites” and “dual anti-poisoning sites” contribute to excellent activity and stability. Firstly, the hierarchical structure boosts generation of active metal-support interface, which is conducive to oxygen migration (including adsorbed oxygen (O<sub>ads</sub>), lattice oxygen (O<sub>lat</sub>) and oxygen vacancy (O<sub>v</sub>)) and metal charge transfer (Mn<sup>2+/3+</sup>+Ce<sup>4+</sup>↔Mn<sup>3+/4+</sup>+Ce<sup>3+</sup>, Ti<sup>4+</sup>+Ce<sup>3+</sup>↔Ce<sup>4+</sup>+Ti<sup>3+</sup>). This is the key to breaking through the limits of catalytic activity stability. Secondly, enhanced surface acidity favors NH<sub>3</sub> adsorption and activation, which accelerates -NH<sub>2</sub>/NH concatenate with NO<sub>x</sub> through Eley-Rideal mechanism to generate N<sub>2</sub> and H<sub>2</sub>O. Thirdly, the dual strong SO<sub>2</sub> affinity sites by Ti-induced CeO<sub>2</sub> crystal reconstruction retard the active center affected by the sulfate species, which contributes to striking stability. This work highlights the importance of design of isolated active sites to improve SO<sub>2</sub> and H<sub>2</sub>O endurance.

## 1. Introduction

A growing body of research shows that air pollution causes significant economic and health losses and that there is a clear association between exposure to air pollution and increased mortality [1–3]. To reduce the health impacts of air pollution, WHO has published the first edition of the < WHO European Air Quality Standards > in 1987, which were updated globally in 2005 and further updated in 2021 [4]. At the same time, the Chinese government has implemented strict environmental regulations in the past few years to improve air quality [5,6]. Since the urgent demand to mitigate the ozone, haze and light pollution during the 14th Five-Year Plan period in China, one of the major precursors, nitrogen oxides (NO<sub>x</sub>, including NO and NO<sub>2</sub>) have been more strictly controlled [7,8]. Among all treatment techniques, selective catalytic reduction with NH<sub>3</sub> (NH<sub>3</sub>-SCR) represents high-effective for

eliminating NO<sub>x</sub> emission and has been used successfully for many years to control exhaust gas from industrial sources [9]. To avoid the formation of sulfated ammonium salt, the general operating temperature of commercial V<sub>2</sub>O<sub>5</sub>-WO<sub>3</sub>(MoO<sub>3</sub>)/TiO<sub>2</sub> is above 320 °C, while the dew point of ammonium bisulfate is above 280 °C (no effect on the SCR reaction, but can produce ammonium bisulfate by thermal decomposition), and ammonium bisulfate is about 280–320 °C [10]. Meanwhile, the application of V<sub>2</sub>O<sub>5</sub>-WO<sub>3</sub>(MoO<sub>3</sub>)/TiO<sub>2</sub> catalysts is limited as their post-use status has been classified as waste hazardous for management in China (National Hazardous Waste List 000014672/2020-01495 HW50 772-007-50). Therefore, low-temperature selective catalytic reduction (SCR) downstream of a desulfurized has aroused extensive concern, which can avoid fly ash erosion and undesirable SO<sub>3</sub> generation. Thus, developing catalysts with high activity in the low-temperature (LT) window is urgently needed.

\* Corresponding authors.

E-mail addresses: [ahnuhkao@163.com](mailto:ahnuhkao@163.com) (F. Gao), [txiaolong@126.com](mailto:txiaolong@126.com) (X. Tang).

Transition metal oxides (TMOs) have been extensively studied for LT-SCR due to their low cost and promising activity, which possess the advantages of variable valence states and adjustable occupancy orbits in REDOX reactions, and are the most potential candidates to replace precious metals [11]. The reported catalytic systems mainly include Mn-based [12], Ce-based [13], Cu-based [14], Fe-based [15], and multi-element composite catalyst systems [16,17]. Among them, Mn-based catalysts show a possible double-exchange behavior between  $Mn^{3+}$  and  $Mn^{4+}$  and exhibit unique catalytic redox performance, and thus, Mn-based materials contain large amounts of surface active oxygen species, which has attracted much attention in investigations of the LT-SCR [18,19]. Especially, the Mn-based spinel structure, referring to the composition  $AB_2O_4$  (where A and B are metal ions in tetrahedral and octahedral positions, respectively), exhibits excellent reducibility, strong surface acidity, high surface oxygen concentration and structural stability [20], and have been attracted for LT-SCR [21,22]. Spinel catalyst contains a large amount of reactive oxygen species and abundant acid sites, which is conducive to the adsorption and reduction of NO [23]. Our research team have found that the oxygen vacancy on the cobalt-manganese spinel is an important active site for REDOX reactions, which promotes the reduction and electron mobility of the catalyst ( $Co^{3+} + Mn^{3+} \leftrightarrow Co^{2+} + Mn^{4+}$ ) [24]. On this basis, team members continue to create Mn-Co spinel nanospheres, nanorods, nanoflakes, nano-flowers, and other objects based on this foundation [25,26]. It is indisputable that Co-Mn spinel oxides exhibit stronger sulfur resistance than Co-MnO<sub>x</sub> complex oxides that have been studied previously [27]. This may be due to the stable stereoscopic structure of spinel, which protects the active site. However, there still exists several hurdles to long-term stable LT-SCR catalytic reactions, which is also the problem faced by current LT deNO<sub>x</sub> catalysts. On the one hand, the excess oxygen concentration gives rise to the oxidation of the reductant NH<sub>3</sub>, which urges related efforts such as developing the by-product N<sub>2</sub>O to reduce the N<sub>2</sub> selectivity [28]. On the other hand, the metal active component is facile to aggregate and poison by SO<sub>2</sub> and H<sub>2</sub>O at low temperatures for a relatively long time, resulting from the lack of appropriate metal-support interaction and antitoxic site, which leads to unsatisfied catalytic stability. According to the scenario, the H<sub>2</sub>O and SO<sub>2</sub> influence mechanism on the SCR reaction can be classified as reversible or irreversible effects. The reversible effect primarily relates to the competitive adsorption between H<sub>2</sub>O or SO<sub>2</sub> and the reaction species (NO and NH<sub>3</sub>) [29]. And the irreversible effect on water is adsorption and decomposition on the surface of the catalyst, forming more hydroxyl groups, and for SO<sub>2</sub> to sulfate the metal active component, or in the presence of H<sub>2</sub>O, accelerating the reaction with NH<sub>3</sub> to form a deposition of sulfated ammonium salt, thereby blocking the transport of the active site and/or reactants [30,31]. Therefore, the development and pursuit of highly efficient and controllable structures that make LT-SCR highly reactive, selective and stable remains a daunting challenge.

According to studies, the adsorption of SO<sub>2</sub> on metal oxide catalysts occurs due to the surface-bound metal cations donating electrons, and the surrounding oxygen is always involved in the process of oxidizing SO<sub>2</sub> into sulfate. So, the key to increasing SO<sub>2</sub> tolerance at low temperatures is appropriate reoxidation and reduction performance [32, 33]. By changing the electrical characteristics of the oxide carrier, the strong metal-carrier interaction can be adjusted, the adsorption capacity of the active site for NH<sub>3</sub> and NO can be controlled, and the adsorption and oxidation of SO<sub>2</sub> can be weakened. Ceria has shown a potential promotional effect on the LT-SCR, benefiting from abundant surface oxygen vacancy (O<sub>v</sub>), which serves as the adsorption and activation sites of SO<sub>2</sub> to protect the active components from being poisoned [34]. Ceria is also widely applied as the support, this reverse design allows cerium dioxide not only to disperse the active species but also has the potential to modulate the electronic and REDOX properties of the dispersed species on the surface. It is worth noting that the reaction pathway can be optimized even in the presence of SO<sub>2</sub> due to the cerium sulfate, one of the toxic substances, can be used as an active site and does not affect the

adsorption of NH<sub>3</sub>. And the SCR reaction based on Eley-Rideal (E-H) mechanism can be carried out smoothly. However, it also lacks long-term catalytic stability caused by continuous SO<sub>2</sub> action. The supported CeO<sub>2</sub>-based catalysts (VO<sub>x</sub>, WO<sub>3</sub>, and NiO) have also been developed to meet low-temperature catalytic requirements and continue the sulfur resistance [35,36]. The doping of heteroatom such as Zr into ceria has been proved as an efficient strategy for strengthening the interaction between active components and support and then improving the thermal stability [37]. Meanwhile Ti has gained widespread attention and application due to its excellent sulfur resistance and easy practicality, and Ce-Ti oxides are considered as promising materials for NH<sub>3</sub>-SCR reactions in the presence of water and sulfur [38,39].

Herein, CoMn<sub>2</sub>O<sub>4</sub> spinel stabilized on Ti-doped CeO<sub>2</sub> (denoted as CMCT) was synthesized through a two-step method with solvothermal and thermal evaporation process, resulting in a mixed oxide with typical carrier phase and even dispersion of the active phase. The catalyst exhibited superior catalytic activity, and outstanding stability under water and sulfur activation for LT-SCR. To verify the formation of the supported mixed oxide, the multi-technique approach combining HRTEM (high-resolution transmission electron microscopy), SEM (scanning electron microscope), XAFS (synchrotron radiation photo-electron spectroscopy), XRD (X-ray diffraction), ICP-OES (Inductively Coupled Plasma Optical Emission), FTIR (Fourier Transform infrared spectroscopy) and Raman spectrometer were chosen to display the microstructure and surface topography. The X-ray photoelectron spectroscopy (XPS), in situ infrared Fourier transform spectroscopy (DRIFTS), H<sub>2</sub>-TPR, NH<sub>3</sub>-TPD were applied to explore the adsorption capacity and reactivity of the surface of catalyst. The low-temperature NH<sub>3</sub>-SCR performance of all the catalysts was investigated under relevant conditions encountered in the industrial flue gas.

## 2. Experimental section

### 2.1. Chemicals and materials

Cerium (III) nitrate hexahydrate (Ce(NO<sub>3</sub>)<sub>3</sub>·6H<sub>2</sub>O, 99.99%), cobalt (II) nitrate (Co(NO<sub>3</sub>)<sub>2</sub>·6H<sub>2</sub>O, 99.99%), glycerol (C<sub>3</sub>H<sub>8</sub>O<sub>3</sub>, 99%), isopropanol (C<sub>3</sub>H<sub>8</sub>O, 99%) and glucose (C<sub>6</sub>H<sub>12</sub>O<sub>6</sub>, 99%) were purchased from Aladdin Shanghai Co., Ltd. Manganese (II) acetate ((CH<sub>3</sub>COO)<sub>2</sub>Mn·4H<sub>2</sub>O, 99.99%), tetra butyl titanate (C<sub>16</sub>H<sub>36</sub>O<sub>4</sub>Ti, 98%) were purchased from Shanghai Macklin Biochemical Co., Ltd. Ethanol (C<sub>2</sub>H<sub>5</sub>OH, 99.9%) were purchased from Sinopharm Chemical Reagent Shanghai Co., Ltd. All the reagents are of analytical grade and used without further purification.

### 2.2. Catalyst preparation

#### 2.2.1. Synthesis of Ce<sub>1-x</sub>Ti<sub>x</sub>O<sub>x</sub> support

Ceria-titanium oxide support (Ce/Ti molar ratio from 1 to 0) was prepared via solvothermal method. In a typical synthesis procedure, 7 mL glycerol (co-solvent) was dissolved in 50 mL isopropanol with vigorous stirring for 30 min. Then the cerium nitrate and tetra butyl titanate with a certain proportion was added to the solution, stirring continuously until the solid substance dissolved completely. After that, the two solutions were transferred into a 100 mL stainless steel autoclave and raised the temperature of the oven to 120 °C and maintained for 48 h. Finally, the resultant was filtered and washed with ethanol until the supernatant was neutral, then dried at 110 °C overnight and calcined at 500 °C for 4 h in a muffle furnace to obtain Ce<sub>1-x</sub>Ti<sub>x</sub>O<sub>x</sub> support.

#### 2.2.2. Synthesis of CoMn<sub>2</sub>O<sub>4</sub> spinel-containing catalysts

Ce<sub>1-x</sub>Ti<sub>x</sub>O<sub>x</sub> supported CoMn<sub>2</sub>O<sub>4</sub> spinel catalyst (Ce+Ti/Mn+Co molar ratio for 5:2) was prepared via thermal evaporation method. The as-prepared Ce<sub>1-x</sub>Ti<sub>x</sub>O<sub>x</sub> and a certain amount of glucose (complexing agent) was dispersed in deionized water with vigorous stirring. (denoted

as solution A) The manganese acetate and cobalt nitrate were weighed in a molar ratio of Mn/Co= 2:1 and dissolved in deionized water through ultrasound. (denoted as solution B) Then solution B was added dropwise into solution A, and the solvent was slowly evaporated and dried under the water bath at 80 °C. The resulting solid was dried at 110 °C overnight and calcined in air at 450 °C for 6 h to obtain  $\text{CoMn}_2\text{O}_4/\text{Ce}_{1-x}\text{Ti}_x\text{O}_x$ . The actual contents of Ti in catalysts were determined by inductively coupled plasma optical emission spectroscopy (ICP-OES) as shown in Table 1.

Notice: The dosage of glucose and glycerol was based on theoretical values and related literature [40–43].

The experimental process is shown in Scheme 1.

### 2.3. Catalyst characterization

Fourier transform infrared spectrometer (FTIR) was carried out on the iS10 FT-IR spectrometer of Negoli, with a wave number range of 400–4000  $\text{cm}^{-1}$ , a resolution of 4  $\text{cm}^{-1}$ , and 32 scans.

X-ray diffraction (XRD) was carried out on a Panalytical Empyrean, Cu K $\alpha$  radiation (40 kV and 40 mA) was used to determine the X-ray diffraction of the catalyst in the range of 5–90° at a rate of 2°/min.

The Visible Raman spectra were acquired using a DXR2 (Thermo Fisher Scientific) instrument equipped with a 532 nm semiconductor laser.

The morphology and structure were performed using scanning electron microscopy (SEM, Zeiss Gemini 500) and high-resolution transmission electron microscope TEM (HRTEM, JEM1200EX).

X-ray photoelectron spectroscopy (XPS) was performed on a Thermo Scientific spectrometer (USA) equipped with Al K $\alpha$  radiation (1486.6 eV), with the carbon 1 s peak (BE = 284.6 eV) used as the standard to calibrate all binding energies. Raman was carried out on the Renishaw model Invia Reflex Raman system, the laser wavelength was 532 nm, and the wave number range was 400–3200  $\text{cm}^{-1}$ .

Mn, Co (K-edge) and Ce (L<sub>3</sub>-edge) X-ray absorption fine structure (XAFS) spectra were measured at the XRD station of beamline 4B9A of Beijing Synchrotron Radiation Facility (BSRF) in transmission mode or fluorescence mode.

Temperature-programmed desorption (TPD) measurements, the NH<sub>3</sub>-TPD were performed on a BUILDER PCA-1200 instrument with a similar procedure. 150 mg catalyst was pretreated under N<sub>2</sub> (50 mL/min) at 200 °C for 1 h, subsequently cooled down to 50 °C in N<sub>2</sub> flow. Then, the catalyst was exposed to 1% NH<sub>3</sub>/N<sub>2</sub> (50 mL/min) for 1 h and flushed with pure N<sub>2</sub> for 30 min to remove physically adsorbed NH<sub>3</sub>. Finally, the NH<sub>3</sub>-TPD curve was recorded as the temperature increases from 50° to 800°C with a heating rate of 10 °C/min. Temperature-programmed reduction (TPR) measurements, the H<sub>2</sub>-TPR were performed on a Microtrac BELCAT II instrument with a similar procedure. 150 mg catalyst was pretreated under N<sub>2</sub> (50 mL/min) at 200 °C for 1 h, subsequently cooled down to 50 °C in N<sub>2</sub> flow. Then, the NH<sub>3</sub>-TPD curve

was recorded as the temperature increases from 50° to 800°C with a heating rate of 10 °C/min.

Inductively coupled plasma (ICP) was carried out on Agilent ICP-OES 730 in the United States, with an emission power of 1.0 KW and carrier gas of argon.

### 2.4. Catalytic test

The catalyst performance testing was carried out in a fixed-bed reactor. 0.1 g of catalyst was weighed and placed in the reaction tube, and the reaction gas was fed into the denitrification reactor through the mass flow meter and gas mixer in turn. The simulated flue gas components were NO<sub>x</sub> concentration of 500 ppm, NH<sub>3</sub> concentration of 500 ppm, O<sub>2</sub> volume fraction of 8%, SO<sub>2</sub> concentration of 100 ppm (when used), H<sub>2</sub>O volume fraction of 10% (when used), N<sub>2</sub> as the balance gas. The gas concentration of each temperature point was analyzed in a stable state using a Thermo Fisher Scientific Nicolet iS50 FT-IR spectrometer. As shown in Scheme S1.

NO<sub>x</sub> conversion, N<sub>2</sub> selectivity and changes of NO<sub>x</sub> conversion were calculated by the following equations: The inlet and outlet concentrations of the components were analyzed by an online Fourier transform infrared (FTIR) spectrometer (iS50). The NO<sub>x</sub> conversion and N<sub>2</sub> selectivity of the catalysts were calculated using the following equations.

$$\text{NO}_x \text{ conversion}(\%) = \frac{[\text{NO}_x]_{\text{in}} - [\text{NO}_x]_{\text{out}}}{[\text{NO}_x]_{\text{in}}} \times 100 \quad (1)$$

$$\text{N}_2 \text{ selectivity}(\%) = \left( 1 - \frac{2 \times [\text{N}_2\text{O}]_{\text{out}}}{[\text{NO}_x]_{\text{in}} + [\text{NH}_3]_{\text{in}} - [\text{NO}_x]_{\text{out}} - [\text{NH}_3]_{\text{out}}} \right) \times 100 \quad (2)$$

$$\text{Changes of NO}_x \text{ conversion}(\%) = \left( \frac{\text{NO}_x \text{ conversion}_{\text{with}}}{\text{NO}_x \text{ conversion}_{\text{without}}} - 1 \right) \times 100 \quad (3)$$

Where  $[\text{NO}_x] = [\text{NO}] + [\text{NO}_2]$ , where the subscripts of (in) and (out) refer to the concentration of the corresponding gases before and after the catalytic reactor, respectively. And the subscripts (with) and (without) refer to the NO<sub>x</sub> conversion of the reaction system with and without H<sub>2</sub>O or SO<sub>2</sub>, respectively. in and out represent the inlet and outlet of the reactor, respectively.

## 3. Results and discussion

### 3.1. Performance of NH<sub>3</sub>-SCR

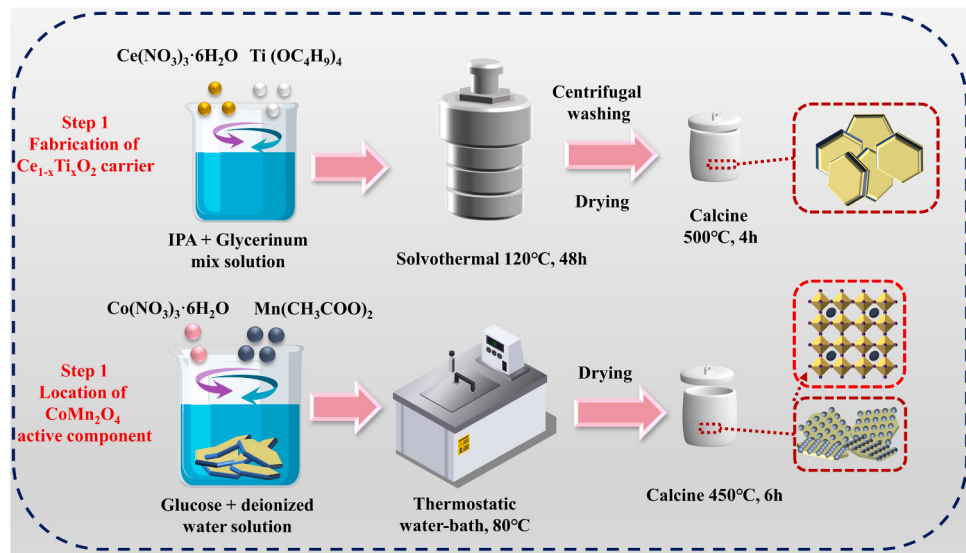
NH<sub>3</sub>-SCR performance under low-temperature (typical at 100 °C and 150 °C) over catalysts with various Ti doping ratios was carried out in the reaction system, and the results are displayed in Fig. S1, three stages including activation zone (the molar ratio of Ti/Ce+Ti=0–0.1), response

**Table 1**  
Different crystallite parameters of catalysts by XRD results.

Sample	Crystal plane	2 theta (deg.)	FWHM (°)	d-Space (nm)	D (nm) <sup>a</sup>	D (nm) <sup>b</sup>	A/A <sub>(111)</sub>
CoMn <sub>2</sub> O <sub>4</sub>	(311)	36.340	0.618	2.470	13.90	13.39	100%
	(113)	32.860	0.583	2.723		14.06	62.4%
	(202)	29.260	0.518	3.050		15.68	28.5%
	(404)	60.720	0.595	1.524		15.31	30.0%
CoMn <sub>2</sub> O <sub>4</sub> /CeO <sub>2</sub>	(111)	28.460	0.842	3.134	6.60	9.63	100%
	(220)	47.480	0.888	1.913		9.67	37.6%
	(200)	33.000	0.807	2.712		10.16	26.4%
	(311)	56.360	0.924	1.631		9.65	25.0%
	(111)	28.554	0.992	3.123		8.66	100.0%
CoMn <sub>2</sub> O <sub>4</sub> /CeTiO <sub>x</sub>	(200)	33.081	0.975	2.706	4.80	8.91	25.9%
	(220)	47.478	1.032	1.913		8.82	35.7%
	(311)	56.334	0.998	1.632		9.47	22.1%

<sup>a</sup> Calculated by Jade 6.5.

<sup>b</sup> Calculated by Scherrer Formula.



Scheme 1. Schematic diagram of catalyst synthesis.

zone ( $Ti/Ce+Ti=0.1-0.5$ ) and stability zone ( $Ti/Ce+Ti=0.5-1$ ) are distinguished clearly. Here the molar ratio of Ti with 0, 0.3, 0.5, and 0.7 is selected as a comparison for further analysis.

Among all the  $CoMn_2O_4/Ce_{1-x}Ti_xO_x$  catalysts,  $CoMn_2O_4/Ce_{0.5}Ti_{0.5}O_x$  exhibits remarkably higher activity than that for  $CeO_2$ ,  $CoMn_2O_4$  and other Ti-doped  $Ce_{1-x}Ti_xO_x$  catalysts at 100 and 150 °C (Fig. 1a), where more than 90% NO<sub>x</sub> conversion in the range of 100–225 °C, and nearly 100% NO<sub>x</sub> conversion in 150–200 °C are displayed. It is discovered that  $CoMn_2O_4/TiO_x$  have substantially greater activity than  $CoMn_2O_4/CeO_x$ , especially at 100 °C, where the  $CoMn_2O_4/TiO_x$  performed well, suggesting that the Ti-doped  $CeO_2$  support could play a role in enhancing the low-temperature activity. The NO<sub>x</sub> conversion rate increases as Ti content increased (< 0.5), but decreases with

the further increase of Ti content (> 0.5), indicating that the reaction behavior of the active site depends on the carrier type to a certain extent. Fig. 1b depicts the N<sub>2</sub> selectivity of catalysts. The N<sub>2</sub> selectivity steadily declines with temperature, which originates from the pre-oxidation of reactant NH<sub>3</sub> to N<sub>2</sub>O at high temperatures. Among which  $CeO_2$  has the best selectivity due to its low catalytic activity. Additionally,  $CoMn_2O_4/Ce_{0.5}Ti_{0.5}O_x$  exhibits splendid N<sub>2</sub> selectivity, which is always > 80% below 150 °C. In contrast to  $CoMn_2O_4$  pure metal oxide, the supported one may contain fewer  $CoMn_2O_4$  active components but still with higher performance owing to good dispersion of active species and strong interaction between metal and support. To further check the catalytic behavior for Ti doping carrier, supported and pure  $CoMn_2O_4$  catalysts, reaction rates under 50–120 °C were conducted (Fig. 1c). The

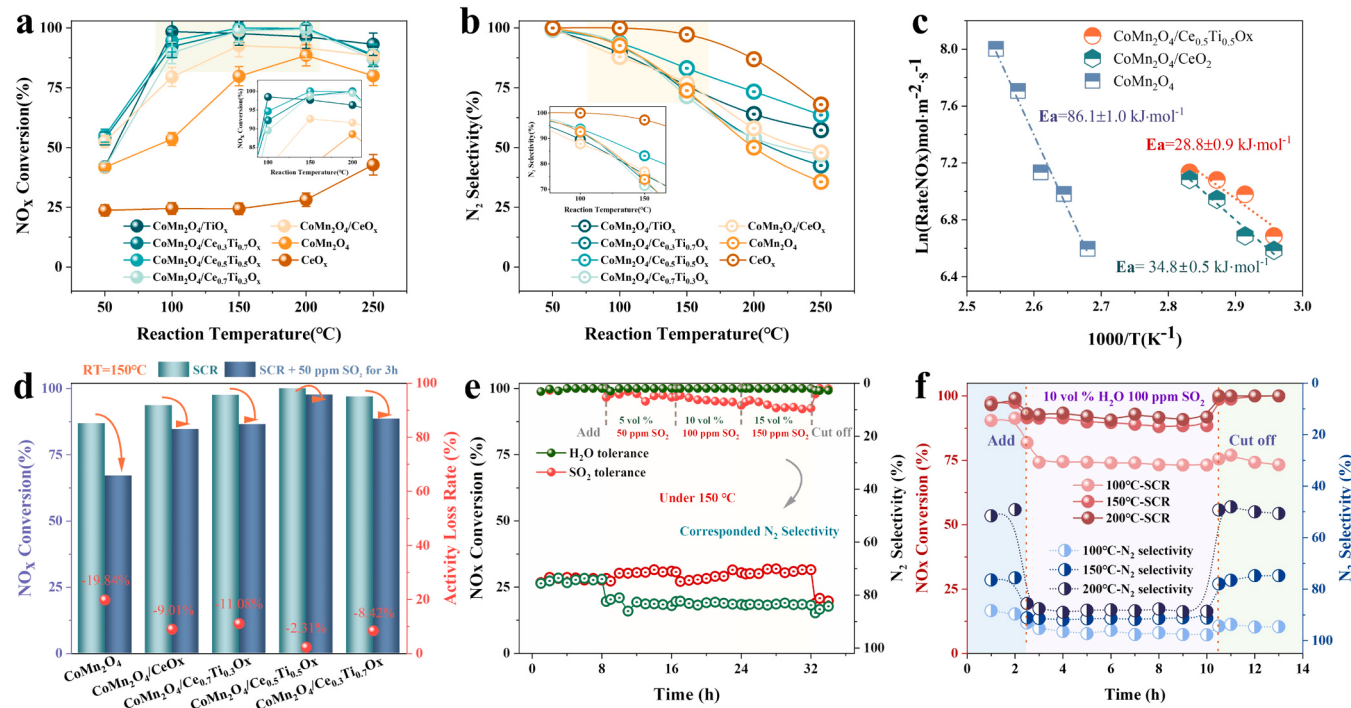


Fig. 1. (a) Comparison of NH<sub>3</sub>-SCR activity (b) N<sub>2</sub> selectivity on the various catalysts. (c) Reaction rates of various catalysts (50–120 °C). (d) Comparison of sulfur resistance over various catalysts at 150 °C. (e) Effect of water and sulfur fluctuation and temperature fluctuation (f) on NH<sub>3</sub>-SCR activity of  $CoMn_2O_4/Ce_{0.5}Ti_{0.5}O_x$  catalyst. Reaction conditions:  $[NO_x] = [NH_3] = 500 \text{ ppm}$ ,  $[O_2] = 8 \text{ vol\%}$ , balance gas N<sub>2</sub>, GHSV = 32,000 h<sup>-1</sup>.

apparent activation energy ( $E_a$ ) of NH<sub>3</sub>-SCR is determined by the slope of the fitted curve, and the results also indicate that CoMn<sub>2</sub>O<sub>4</sub> supported by Ti-doped CeO<sub>2</sub> has better catalytic activity with a lower reaction activation energy of  $28.8 \pm 0.9 \text{ kJ mol}^{-1}$ , while CoMn<sub>2</sub>O<sub>4</sub> and CoMn<sub>2</sub>O<sub>4</sub>/CeO<sub>2</sub> present  $86.1 \pm 1.0 \text{ kJ mol}^{-1}$  and  $34.8 \pm 0.5 \text{ kJ mol}^{-1}$  respectively, which also exhibits outstanding strength than other catalysts reported in recent years (Table S1).

Since pure CeO<sub>x</sub> support produces lower catalytic activity (Fig. 1a), the excellent catalytic performance of CoMn<sub>2</sub>O<sub>4</sub>/Ce<sub>1-x</sub>Ti<sub>x</sub>O<sub>x</sub> is reasonably attributed to the synergistic effects between CoMn<sub>2</sub>O<sub>4</sub> and CeTiO<sub>x</sub> support. The catalytic stability for CoMn<sub>2</sub>O<sub>4</sub> has been challenging owing to the facile poisoning caused by the continuous action of SO<sub>2</sub> and H<sub>2</sub>O [27]. Surprisingly, CoMn<sub>2</sub>O<sub>4</sub>/Ce<sub>0.5</sub>Ti<sub>0.5</sub>O<sub>x</sub> exhibits excellent catalytic stability over 3 h of action of 50 ppm SO<sub>2</sub> with a 2.31% activity loss ( $\Phi$ ), compared to that for CoMn<sub>2</sub>O<sub>4</sub> ( $\Phi = 19.84\%$ ) and CoMn<sub>2</sub>O<sub>4</sub>/Ce<sub>1-x</sub>Ti<sub>x</sub>O<sub>x</sub> ( $\Phi = 8\text{--}11\%$ ) with different Ti proportions. The doping of smaller-sized Ti atoms into CeO<sub>2</sub> will lead to the structural reconstruction of CeO<sub>2</sub> with a shorter Ti-O bond but a longer Ce-O bond [44]. The structural

deformation lowers the energy barrier for the aggregation of the CoMn<sub>2</sub>O<sub>4</sub> active phase and encourages the embedding of CoMn<sub>2</sub>O<sub>4</sub>. Therefore, it can be concluded that CoMn<sub>2</sub>O<sub>4</sub>/Ce<sub>0.5</sub>Ti<sub>0.5</sub>O<sub>x</sub> exhibits high structural stability owing to the stronger metal-support interaction between CoMn<sub>2</sub>O<sub>4</sub> and Ti-doped CeO<sub>2</sub>, which contributes to the excellent catalytic performance for NH<sub>3</sub>-SCR and outstanding stability under H<sub>2</sub>O and SO<sub>2</sub> containing conditions (Fig. 1d-e). The dual SO<sub>2</sub> trapping functions of the Ce and Ti sites result in a change in the SO<sub>2</sub> adsorption sites on metal oxides, effectively shielding the low-temperature active center CoMn<sub>2</sub>O<sub>4</sub> from delayed sulfur poisoning (Fig. 2c-d). Meanwhile, the catalyst is still able to maintain the adsorption of NH<sub>3</sub>, which lessens the inhibitory effect on the SCR process thanks to the enlarged Ti acid sites and the sulfate acid sites Ce<sub>2</sub>(SO<sub>4</sub>)<sub>3</sub> generated by CeO<sub>2</sub> carrier pre-sulfurization (Fig. 7) [34,39]. But when the quantity of Ti is raised, the anti-sulfur action of the catalyst initially rises and then falls, which could be connected to the dynamic equilibrium between encouraging NH<sub>3</sub> adsorption and discouraging SO<sub>2</sub> adsorption. Additionally, the effects of the reaction condition on the catalyst are explored, including

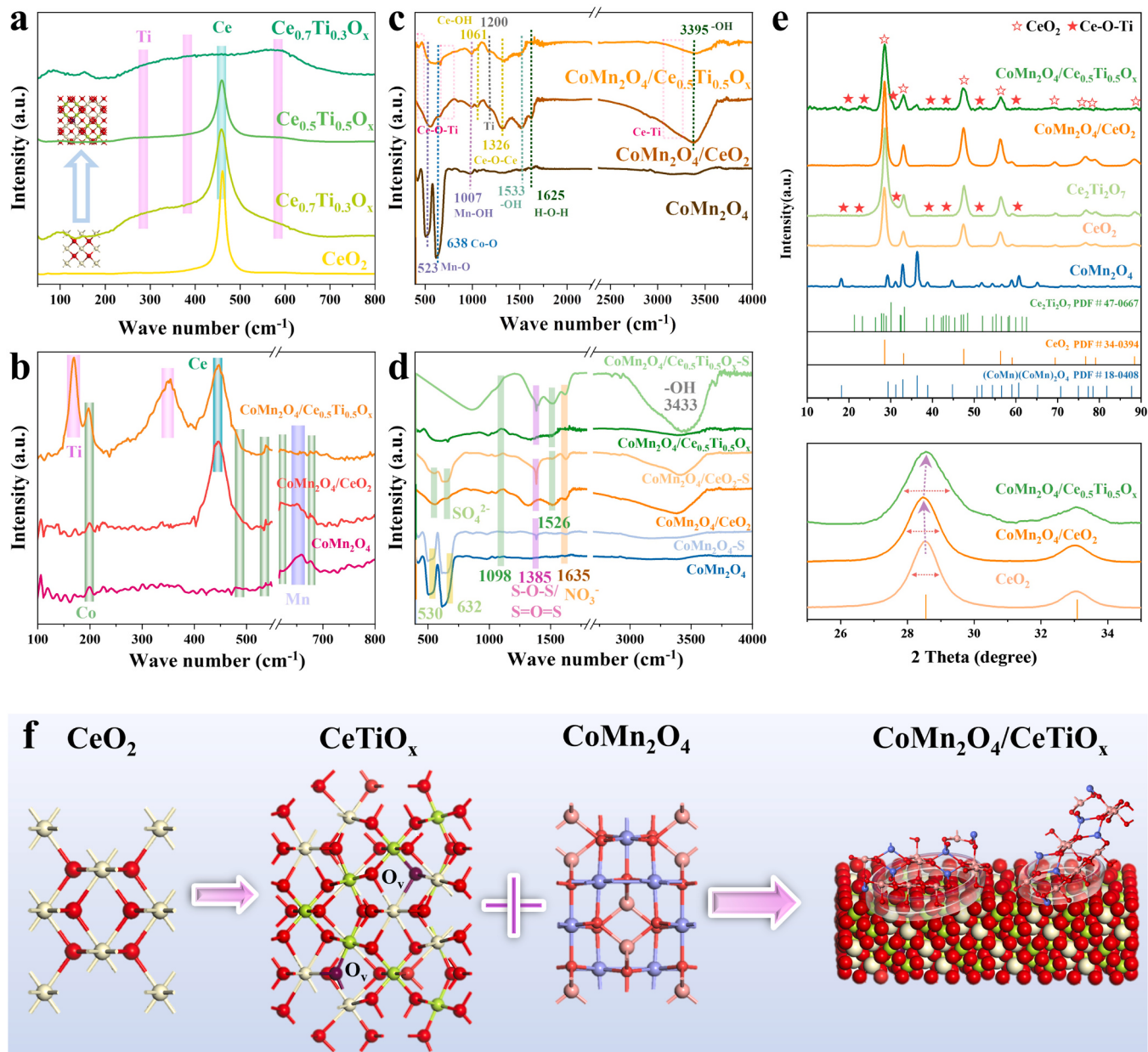


Fig. 2. (a)-(b) Raman spectroscopy, (c)-(d) FTIR curves, (e) XRD patterns, (f) Structure diagram of catalysts.

how changes in the  $\text{SO}_2$ ,  $\text{H}_2\text{O}$ , and reaction temperature (Fig. 1d-e). Among all results,  $\text{CoMn}_2\text{O}_4/\text{Ce}_{0.5}\text{Ti}_{0.5}\text{O}_x$  maintains a stable NOx conversion with almost uniformity during water effect (5, 10, 15 vol%) and a slight decrease (still above 90%) under  $\text{SO}_2$  action (50, 100, 150 ppm). Three reaction intervals of 100 °C, 150 °C, and 200 °C are chosen to evaluate the simultaneous water resistance and sulfur resistance at various reaction temperatures. As shown in Fig. 1f, the NOx removal rate decreases to about 75% within 2 h at 100 °C, while the reduction of catalytic activity decreases to about 90% within 8 h at 150 and 200 °C, indicating that the catalyst can maintain good water and sulfur resistance at 150 °C. When the catalyst is injected with water alone, there is essentially little change in the catalytic activity, and the activity is lower when water and sulfur added together, as can be observed by comparing Fig. 1e-f. Therefore, it is implied that rather than competing adsorption, the poisonous impact of  $\text{H}_2\text{O}$  is mostly caused by the blocking of the active site by sulfated ammonium salt created by the interaction with  $\text{SO}_2$  and  $\text{NH}_3$ . At the same time, Fig. 1f shows that when the water and sulfur are removed at 150 and 200 °C, the catalytic activity returns to its initial level, showing that competitive adsorption and sulfated ammonium salt production coexist and are dominated by competitive adsorption, while the active site is almost unaffected by sulfated ammonium salt. When the water and sulfur are removed from the reaction at 100 °C, the catalytic activity do not revert to its initial level, demonstrating that sulfated ammonium salt generation predominates the reaction, which has a negative effect on the active sites. It is undeniable that in the presence of water and sulfur,  $\text{CoMn}_2\text{O}_4/\text{Ce}_{0.5}\text{Ti}_{0.5}\text{O}_x$  catalyst has better low-temperature activity and longer high-activity plateau than some LT catalysts have been reported, as shown in Table S2.

Fig. 1e-f also demonstrates that  $\text{N}_2$  selectivity rises dramatically in the presence of water, particularly when water and sulfur are present at the same time, which is advantageous for the use of the catalyst at low temperatures. The main cause of this phenomenon is attributed to the presence of  $\text{H}_2\text{O}$ , and a reasonable hypothesis is that  $\text{H}_2\text{O}$  can dissociate and adsorb at sites related to hydrated species like  $\text{Ti-O-Ti}$  and  $\text{Ce-O-Ce}$ . This would lead to the formation of more surface  $\text{Ti-OH}$  and  $\text{Ce-OH}$  species, which would act as Brønsted acid sites and increase  $\text{NH}_3$  adsorption [45,46]. From the perspective of the reaction path,  $\text{H}_2\text{O}$  could improve selectivity by encouraging  $\text{NH}_3$  to shift toward the path of coordinated  $\text{NH}_3^{+4}$  and  $\text{-NH}_2$  species, inhibiting excessive oxidative of  $\text{NH}_3$  dehydrogenation, reducing the formation of  $\text{-NH}$ , and then inhibiting the reaction rate of the  $\text{N}_2\text{O}$  formation [47]. In general, the inhibitory effect is more significant in the coexistence of  $\text{SO}_2$  and  $\text{H}_2\text{O}$  than that of them alone, which may originate from the active sites covered by the formation of sulfate. The activity can be restored when  $\text{H}_2\text{O}$  and  $\text{SO}_2$  are cut off, which indicates that the activity was mainly affected by competitive adsorption, in other words, the main LT active sites were almost unaffected by the deposition of ammonium sulfate.

### 3.2. Surface structure evolution and characterization

#### 3.2.1. Bulk structure properties

To confirm the chemical compositions of as-prepared samples, the Raman measurements were conducted with the results shown in Fig. 2a. For the sample without an active component, pure  $\text{CeO}_2$  exhibits a prominent peak at 461  $\text{cm}^{-1}$  corresponding to the  $\text{F}_{2g}$  Raman active mode of symmetric stretching vibration of  $\text{Ce-O-Ce}$  in metal oxides with a fluorite-like structure [48]. The addition of Ti leads to a gradual attenuation of the  $\text{F}_{2g}$  band intensity, and this is likely caused by the decrease of Ce amount and different crystallite sizes of  $\text{CeO}_2$ . The Raman scattering profiles provide further evidence that the anatase phase is the major crystalline structure and showed a slight Raman peak in three positions (297, 391, and 585  $\text{cm}^{-1}$ ) in all targets. Among which a wide peak at 297 and a strong peak at 391  $\text{cm}^{-1}$  represent the anatase  $\text{B}_{1g}$  phases, respectively [49,50]. However, this former peak value deviates from the theoretical value of 244  $\text{cm}^{-1}$  and this blue shift may be caused

by non-stoichiometry or the small size effect [51]. Also, the related peak observed at around 585  $\text{cm}^{-1}$  is attributed to the production of oxygen vacancies, indicating that the bulk oxygen vacancies form on these catalysts [52]. This conclusion is consistent with XRD that Ti has caused the structural change of the  $\text{CeO}_2$  catalysts (Fig. 2e). A small amount of Ti doping does not change the structure of  $\text{CeO}_2$  and forms a solid solution with a fluorite structure. However, a large amount of  $\text{TiO}_2$  will lead to structural distortion and accumulate on the surface of the catalyst. Since only the O atoms move, the vibrational mode is almost independent of the ionic mass of cerium. The broad peak in the Raman spectrum is mainly from stretching vibrations of  $\text{CeO}_2$  nanoparticles, which are the building blocks of nanocrystals.

Due to the loading of  $\text{CoMn}_2\text{O}_4$  spinel, it can be observed from the more sensitive Raman analysis that the main characteristic peaks of  $\text{Mn}_2\text{O}_3$  exist in the range of 623–652  $\text{cm}^{-1}$ , but the characteristic peaks of Ce-Ti carriers gradually disappear [53]. The Raman bands at  $\approx 194$ , 482, 524, 616, and 688  $\text{cm}^{-1}$  are corresponded to the  $\text{F}_{2g}$ ,  $\text{E}_{2g}$ ,  $\text{F}_{2g}$ ,  $\text{F}_{2g}$ , and  $\text{A}_{1g}$  phonon modes, thus confirming the existence of  $\text{Co}_3\text{O}_4$  [54,55], as shown in Fig. 2b. The Raman spectra of the catalysts with the two support forms are different. Compared with  $\text{CoMn}_2\text{O}_4$ ,  $\text{CeO}_2$  and Ce-Ti supported catalysts show characteristic peaks moving to low-frequency Raman bands. This phenomenon may indicate that part of  $\text{CoMn}_2\text{O}_4$  is bound to the  $\text{CeO}_2$  lattice. In contrast, the Ce-Ti supported catalyst shows two bands at 150 and 194  $\text{cm}^{-1}$  with higher intensity and wider characteristics compared to Mn-Co particles, corresponding to the rutile  $\text{B}_{1g}$  phase of  $\text{TiO}_2$  and Co(IV) oxide respectively [54,56]. In addition, the lower and wider Raman spectra indicates that the crystallite reduction of the catalyst is due to the lattice distortion caused by the introduction of active components into the  $\text{CeO}_2$  lattice, which facilitates the formation of lattice defects and inhibits the crystal growth rate [52,57]. This finding is consistent with the XRD results.

FTIR spectra were collected for further elucidation of the structural phases of the as-prepared composite samples (Fig. 2c). The wide absorption band at 3395  $\text{cm}^{-1}$  is attributed to the stretching vibration of hydrogen-bonded -OH groups from the adsorbed water, while those peaks around 1625  $\text{cm}^{-1}$  correspond to the bending vibrations in plane H-O-H of  $\text{H}_2\text{O}$ . Due to the higher concentration of hydroxyl groups on the surface of  $\text{CeO}_2$  carrier, the variation in the strength of the hydroxyl group exhibits a positive correlation pattern with the acidity of the catalyst surface (Fig. 6b-c). This is because when the hydroxyl group binds strongly to the surface metal ions, the hetero-cleavage of the O-H bond leaves a negative charge on the oxygen side, which is prone to release the  $\text{H}^+$  ions and cause acidity [58]. It is observed that the strong transmittance bands at 638 and 523  $\text{cm}^{-1}$  are attributed to the stretching vibrational modes of the spinel  $\text{CoMn}_2\text{O}_4$  compounds [59]. These two bands are due to the interaction of tetrahedrally coordinated  $\text{Mn}^{2+3+}$ ,  $\text{Co}^{3+}$  and octahedrally coordinated  $\text{Mn}^{3+4+}$ ,  $\text{Co}^{2+}$  ions with the oxygen in the spinel structure. The absorption bands around 1007  $\text{cm}^{-1}$  are assigned to bending vibrations of O-H combined with the Mn atoms, and the intensity of this group gradually increases, indicating that the higher the valence state of the Mn ion is, the simpler it is for it to bind OH and release  $\text{H}^+$  [60]. The signal peak of the  $\text{CoMn}_2\text{O}_4$  decreased gradually after loading on supports, suggesting that some Mn, Co elements might be highly dispersed on the surface of the catalysts in the  $\text{CeO}_2$  bulk, which is consistent with the XRD results. The peak at 1533  $\text{cm}^{-1}$  is due to physically adsorbed water molecules, and the pure  $\text{CeO}_2$  carriers have a certain amount of surface -OH, whereas Ti doping causes a drop in surface -OH, which may result in a decrease in sulfated ammonium salt species [61,50]. Peaks below 883  $\text{cm}^{-1}$  are ascribed to the n(Ce-O) or n(Ti-O) vibrational mode and the formation of Ce-O-Ti linkage bonds is most likely the reason why  $\text{CeTiO}_x$  tends to have a strong wavenumber shift in the bands at 400 and 744  $\text{cm}^{-1}$ . Because  $\text{Ce}^{4+}$  has a greater electronegativity than  $\text{Ti}^{4+}$ , the creation of Ce-O-Ti linkage bonds alters the polarity of Ce-O and Ti-O. In addition, The bands refer to 1061, 1200 and 1326  $\text{cm}^{-1}$  are assigned to the bending vibrations of the hydroxyl group of metal oxides (Ce-OH), Ti-O-Ti, and

Ce-O-Ce vibrations [62–64]. In summary, since the carrier is a variable valence carrier, combined with TEM and XRD data, indicating that a very significant charge transfer occurs between the metal and the carrier, resulting in reversible nanoscale structural changes [65,66]. And the structure is shown in Fig. 2g, the carrier mainly presents the  $\text{CeO}_2$  doped by Ti, while the active component  $\text{CoMn}_2\text{O}_4$  is embedded by the carrier.

When the catalyst spent 3 h in a 50 ppm  $\text{SO}_2$  environment, obvious S species appear on the surface. A characteristic band at  $1385\text{ cm}^{-1}$  observed in the FT-IR spectrum of sulfated oxide (Fig. 2d) is due to the surface bonded sulfate groups having  $\text{S}=\text{O}$  covalent bonds, whereas the enhanced and weakened bands at  $660$ ,  $1098$  and  $1526\text{ cm}^{-1}$  are assigned to the metal sulfate ( $\text{M}-\text{SO}_{2-x}$   $x = 3$  or  $4$ ) and the  $1635\text{ cm}^{-1}$  wavelength corresponded to the vibration of the monodentate nitrate peak [67,68]. Among them, the peak of metal oxide in the  $\text{CoMn}_2\text{O}_4$  catalyst gradually widens ( $530$ ,  $660\text{ cm}^{-1}$ ), which may be attributed to the formation of metal sulfate that influences the vibration of the metal-oxygen bond [69,70]. By passing the catalyst through flue gases containing  $\text{H}_2\text{O}$  or  $\text{SO}_2$ , it has been shown that metal sulfates or ammonium sulfate salts are produced. These salts either prevent the reactive gases from adhering to the catalyst or cover its active sites, limiting the catalytic activity. The peaks of metal sulfates are attenuated (below  $1000\text{ cm}^{-1}$ ) when Ce-Ti was utilized as a carrier. The hydroxyl-related peaks increased ( $3433$  and  $1526\text{ cm}^{-1}$ ), whereas the surface sulfur-oxygen bonding shrunk and widened ( $1385\text{ cm}^{-1}$ ), indicating that part of the sulfate species have changed and may be connected to the synthesis of hydrogen-sulfate.

The crystallographic structure of the prepared catalysts was measured by the wide-angle XRD, as shown in Fig. 2e. It can be inferred that Mn-Co (2:1) particles exhibit a  $(\text{Co}, \text{Mn})(\text{Co}, \text{Mn})_2\text{O}_4$  crystal phase, and the diffraction peaks are ascribed to the  $\text{CoMn}_2\text{O}_4$  spinel-type structure (JCPDF#18-0408) [71,72].  $\text{CoMn}_2\text{O}_4/\text{CeO}_2$  shows intense and sharp diffraction peaks of cubic fluorite structure (JCPDF#34-0394), accompanied by weakness and disappearance of spinel phase, indicating that Mn, Co elements are highly dispersed in the  $\text{CeO}_2$  bulk. In the  $\text{CeTiO}_x$  vector, the  $\text{CeO}_2$  crystal form is still dominant, but it is noted that the doping of Ti into  $\text{CeO}_2$  leads to an additional phase of  $\text{Ce}_2\text{Ti}_2\text{O}_7$  (JCPDF#47-0667), which suggests that crystallites with the Ce-O-Ti structure might be formed. There may exist reversible crystal phase transformation between the  $\text{Ce}_2\text{Ti}_2\text{O}_7$  pyrochlore and Ce-Ti mixed oxides during the REDOX, thus enhancing the mobility of lattice oxygen [73]. Meanwhile, compared with the  $\text{CoMn}_2\text{O}_4/\text{CeO}_2$  catalyst, the peak of  $\text{CoMn}_2\text{O}_4/\text{CeTiO}_x$  series catalysts at  $2\theta = 28.6^\circ$  is shifted slightly to a higher theta value, suggesting that Ti was successfully doped into ceria lattice structure due to that the ionic radius of  $\text{Ti}^{4+}$  is smaller than that of  $\text{Ce}^{3+}$ , resulting in the formation of a solid solution accompanied by the shrunked interplanar spacing of  $\text{CeO}_2$ . The average thickness ( $D$ ) of the grain perpendicular to the crystal plane is significantly reduced (calculated by Scherrer's formula), which also proves that Ti ions successfully enter the  $\text{CeO}_2$  structure (Table 1). These results further confirm that the exposure ratio of metal atoms gradually increases with the decrease of metal particle size, which significantly changes the structure and proportion of active centers of catalytic materials, thus enhancing the catalytic activity [74]. Furthermore, no  $\text{CoMn}_2\text{O}_4$ -related XRD patterns are observed, owing to the high dispersion of the spinel species.

Table S3 shows the textural parameters of these catalysts, the Brunauer-Emmett-Teller (BET) specific surface area of  $\text{CoMn}_2\text{O}_4/\text{CeTiO}_x$  ( $38.64\text{ m}^2\text{ g}^{-1}$ ) and  $\text{CoMn}_2\text{O}_4/\text{CeO}_2$  ( $41.54\text{ m}^2\text{ g}^{-1}$ ) catalysts are much higher than  $\text{CoMn}_2\text{O}_4$  ( $22.99\text{ m}^2\text{ g}^{-1}$ ). The isotherms of all catalysts are type IV, correspond to H3 ( $P/P_0 = 0.4$ – $1.0$ ) hysteresis loop, and the pore width of  $\text{CoMn}_2\text{O}_4/\text{CeO}_2$  and  $\text{CoMn}_2\text{O}_4/\text{CeTiO}_x$  are  $3.82$  and  $3.71\text{ nm}$  while  $\text{CoMn}_2\text{O}_4$  exhibits almost no micro-pores (Fig. S2), indicating that the formed seam-shaped pore formed on the surface of the material is accumulated by loose sheet particles. To further quantitative analysis of the chemical contents of the samples, ICP-OES is also

applied. It shows that the  $\text{CoMn}_2\text{O}_4$  sample displays an Mn: Co ratio of  $1.7:1$ , while  $\text{CoMn}_2\text{O}_4/\text{CeTiO}_x$  exhibits an Mn:Co:Ce: Ti ratio of  $1.7:1:2.3:1.8$ , which is similar but exists errors to the expected stoichiometric ratios, where the proportion of Ce is greater than that of Ti, which is mainly attributed to the existence of separated  $\text{CeO}_2$  phase in the system in addition to the Ce-Ti carrier phase, corresponds to the results in Fig. 2e. Similarly, the ratio of Mn:Co:Ce is  $1.8:1:1$  in  $\text{CoMn}_2\text{O}_4/\text{CeO}_2$ , showing less carrier amount, which might be attributed to the better dispersion and lower agglomeration of active components on the surface of the Ce-Ti carrier. In addition, incomplete dissolution of a very small number of samples and instrument errors may also be the reason for the difference in theoretical values.

### 3.2.2. Microstructure and composition

The morphologies of three catalysts were investigated by SEM, as depicted in Fig. 3a-c,  $\text{CoMn}_2\text{O}_4$  exhibits an aggregated granular structure, while  $\text{CoMn}_2\text{O}_4/\text{CeO}_2$  appears as a hierarchical structure with many nanoparticles loaded on the lamellar support. As a comparison, the  $\text{CoMn}_2\text{O}_4$  nanoparticles that exists on the surface of  $\text{CeTiO}_x$  are more dispersed and uniform, accompanied by a trapped state in the carrier. The above observations confirm that the carrier is beneficial to the dispersion of the active component of the metal, and the Ti-doped  $\text{CeO}_2$  carrier further promotes closer binding with the active component. The microstructure of the  $\text{CoMn}_2\text{O}_4/\text{CeTiO}_x$  catalyst is recorded by transmission electron microscopy. It can be observed that the catalyst of  $\text{CeTiO}_x$  is a dispersed lamellar structure, with a length and width of about  $500$ – $900\text{ nm}$ , and the supported active components of Mn-Co are spherical or massive dispersed on the surface of the support. Since there are several diffraction peaks in the SEAD diagram, only a few obvious diffraction peaks are analyzed in relation to the active components and carriers. Crystal lattices of manganese cobalt oxide, cerium oxide and Ce-Ti oxide can be observed from lattice analysis and SEAD diffraction pattern (Fig. 3d-g). In addition to the  $\text{CeO}_2$  (111) and (331) diffraction rings, d-spacings of  $0.312$ ,  $0.270\text{ nm}$  belong to  $\text{CeO}_2$  (111) and  $\text{CeO}_2$  (200), while  $0.327\text{ nm}$  belongs to  $\text{TiO}_2$ (110). Clear lattice spacings of  $0.320$  and  $0.337\text{ nm}$  are observed in the Ce-Ti oxide carrier, correspond to  $\text{Ce}_2\text{Ti}_2\text{O}_7$  (400) and (310) respectively, indicating the formation of Ce-Ti solid solution, which exhibits an obvious unsaturated coordination structure. Relevant studies have shown that anion-deficient  $\text{Ce}_2\text{Ti}_2\text{O}_7$  will be re-oxidized back to  $\text{CeO}_2$  and  $\text{TiO}_2$  after adding O anion, so the phase transition between  $\text{CeO}_2$ - $\text{TiO}_2$  and  $\text{Ce}_2\text{Ti}_2\text{O}_7$  is reversible [73]. This is consistent with the enhancement of lattice oxygen transport by Mn, Co and other active species and the increase of the REDOX cycle of Ce ( $\text{Ce}^{4+} \leftrightarrow \text{Ce}^{3+}$ ) in the XPS data. In addition, interfacial lattice interlacing between MnCo oxide and Ce-Ti carrier appears, among which the interlacing between  $\text{CeO}_x$  and Ce-Ti oxide and  $0.265\text{ nm}$  lattice spacing corresponding to  $\text{CoMn}_2\text{O}_4$  (103) interface is more obvious. The distribution of elements in the sample was studied by the element mapping method (Figs. 3h and S3). Each element is evenly distributed in the catalyst, and the MnCo component is highly dispersed in  $\text{CeTiO}_x$ , indicating that  $\text{CoMn}_2\text{O}_4$  and  $\text{CeTiO}_x$  nanosheets are well mixed. Therefore, it can be concluded that  $\text{CoMn}_2\text{O}_4$  shows a high degree of chimerism in  $\text{CeTiO}_x$  nanosheets, and an obvious interface is achieved between appearances.

### 3.3. Effect of Ti-doping on reaction activity and redox properties

#### 3.3.1. Surface electron transfer

As demonstrated above,  $\text{CoMn}_2\text{O}_4/\text{CeTiO}_x$  has shown excellent performance for  $\text{NH}_3$  selective reduction of  $\text{NO}_x$  and  $\text{H}_2\text{O}$  and  $\text{SO}_2$  tolerance, which is attributed to the synergistic effects between  $\text{CoMn}_2\text{O}_4$  and  $\text{CeTiO}_x$  support. To obtain a deeper understanding of this synergistic effect, a series of characteristics were performed.

The surface chemical composition and elemental oxidation states of the catalysts were investigated by X-ray photoelectron spectroscopy (XPS). The XPS spectra of Mn, Co, O, Ce, and Ti are shown in Fig. 3, and

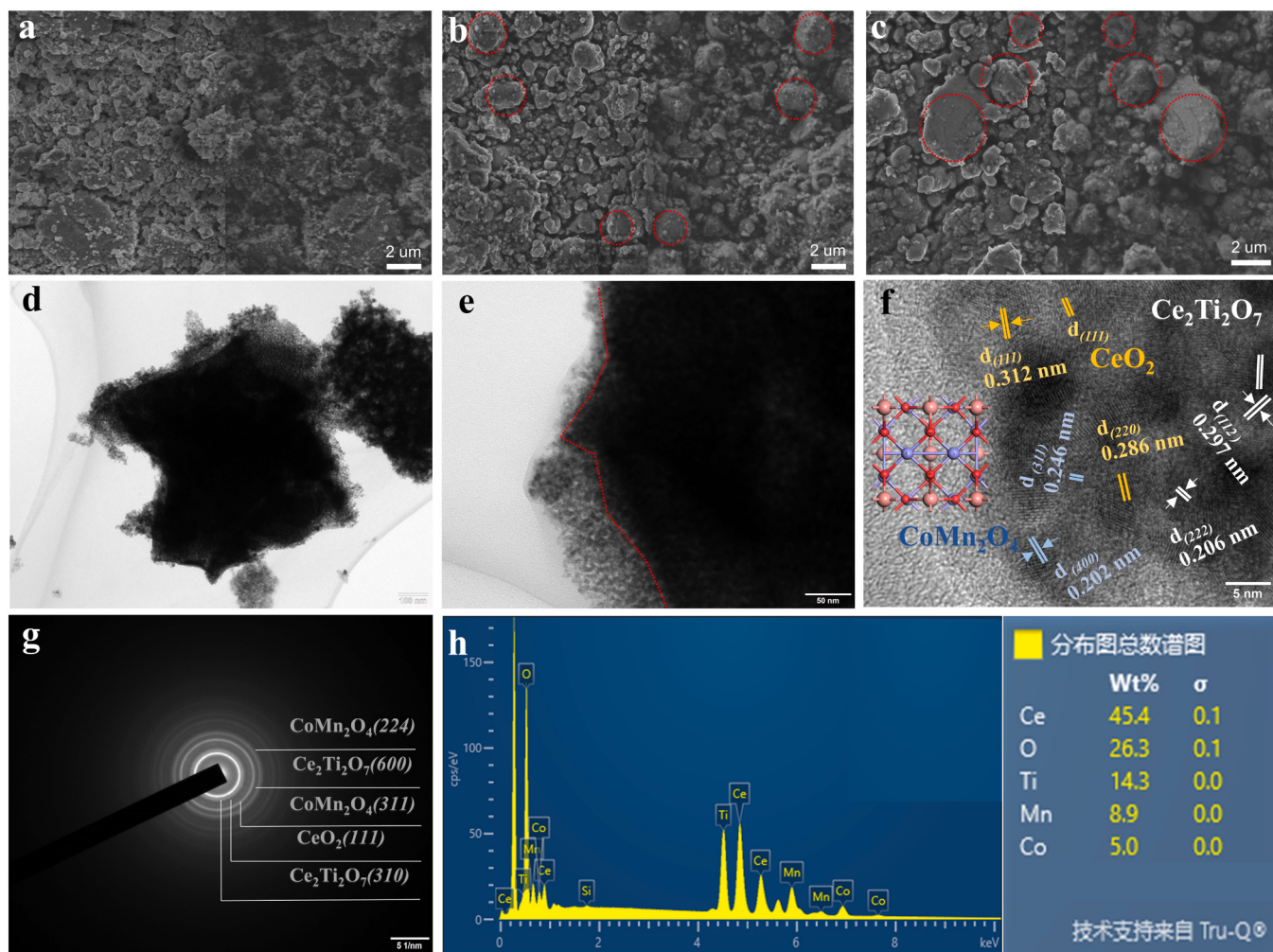


**Fig. 3.** (a-c) and SEM (InLens and SE2 model in 5 kV, 6.2 mm working distance) of various catalysts, (d-f) HRTEM, (g) SEAD and (h) EDX images of CoMn<sub>2</sub>O<sub>4</sub>/CeTiO<sub>x</sub> collected by SEM.

the surface element proportion atom ratios of the catalysts are summarized in Tables 2 and 3. Fig. 3a, b, and f illustrate Mn 3 s, Mn 2p XPS spectra and the average oxidation state of Mn respectively. By linear comparison of  $\Delta E$  of Mn 3 s spectral peaks, it can be seen that the average valence state of Mn in the catalyst increases from + 2.85 to + 3.35 and + 3.33 after loading CeO<sub>2</sub> and doping Ti in the CeO<sub>2</sub> carrier, which indicates that the catalyst with improved performance has a changed behavior of Mn element from low-value state to high-value state with continuous and enhanced cyclic transmission of electrons ( $Mn^{2+}/3+ + Ce^{4+} \leftrightarrow Mn^{3+}/4+ + Ce^{3+}$ ,  $Ti^{4+} + Ce^{3+} \leftrightarrow Ce^{4+} + Ti^{3+}$ ). On the other hand, hypervalent Mn species (including Mn<sup>3+</sup> and Mn<sup>4+</sup>) can also serve as Lewis acid sites to promote the adsorption and activation of gaseous molecules [75]. Mn 2p displays two main spectral peaks, Mn 2p<sub>1/2</sub> and Mn 2p<sub>3/2</sub> with binding energies of 653.2 and 641.6 eV, respectively. The peak of Mn 2p<sub>3/2</sub> can be divided into three peaks at 640.5, 644.1 and 643.1 eV by peak fitting, which is corresponded to the species Mn<sup>2+</sup>, Mn<sup>3+</sup>, Mn<sup>4+</sup>, respectively [22,76]. The ratio of Mn<sup>4+</sup> and

**Table 3**  
The relative percent of the surface element of the samples (%).

Catalyst	Mn	Co	Ce	Ti	O	Mn:Co:Ce:Ti
CoMn <sub>2</sub> O <sub>4</sub>	24.60	10.85	-	-	64.55	2.27:1
CoMn <sub>2</sub> O <sub>4</sub> /CeO <sub>2</sub>	13.81	6.40	10.19	-	69.59	2.16:1:1.59
CoMn <sub>2</sub> O <sub>4</sub> /CeTiO <sub>x</sub>	16.70	6.68	5.93	3.96	66.73	2.5:1:0.89:0.60

Mn<sup>3+</sup> in supported catalyst CoMn<sub>2</sub>O<sub>4</sub>/CeTiO<sub>x</sub> (45.2% and 31.8%) is much higher than that of unsupported CoMn<sub>2</sub>O<sub>4</sub> (34.0% and 32.8%), which is consistent with the changing trend of the valence of Mn 3 s. It is generally believed that the abundance of Mn<sup>4+</sup> and Mn<sup>3+</sup> species is beneficial to improve the redox ability along with the redox couples of Mn<sup>3+</sup>↔Mn<sup>4+</sup>, thus promoting the activity through the “fast-SCR” pathway.<sup>65</sup>

Further, the XPS spectra for Co 2p over catalysts are presented in Fig. 3c, which are fitted into Co<sup>3+</sup> at 779.6 eV and Co<sup>2+</sup> at 780.9 eV of

**Table 2**

The percent of valence state on the surface of the samples was calculated from XPS results. (%)

Catalyst	Ce <sup>3+</sup> /Ce <sup>4+</sup>	Mn <sup>2+</sup> /Mn	Mn <sup>3+</sup> /Mn	Mn <sup>4+</sup> /Mn	Co <sup>2+</sup> /Co	Co <sup>3+</sup> /Co	O <sub>1</sub> /O	O <sub>2</sub> /O	O <sub>3</sub> /O
CoMn <sub>2</sub> O <sub>4</sub>	/	33.2	34.0	32.8	50.9	49.1	64.8	26.8	8.4
CoMn <sub>2</sub> O <sub>4</sub> /CeO <sub>2</sub>	20.6	28.1	41.9	30.0	46.4	53.6	62.7	31.5	5.7
CoMn <sub>2</sub> O <sub>4</sub> /CeTiO <sub>x</sub>	26.2	23.0	45.2	31.8	40.6	59.4	56.5	34.1	9.4

Co 2p<sub>3/2</sub>. The other spin-orbit component (Co 2p<sub>1/2</sub>) is found at 795.4 eV and 797.3 eV, corresponding to Co<sup>3+</sup> and Co<sup>2+</sup> configuration, respectively [25,47]. Besides, the peaks center at 785.4 eV and 802.2 eV could be assigned to the satellite peak of Co 2p [24]. As can be seen from Table 2, the Co<sup>3+</sup> contents of CoMn<sub>2</sub>O<sub>4</sub>/CeTiO<sub>x</sub> (59.4%) are higher compared with CoMn<sub>2</sub>O<sub>4</sub> (49.1%), indicating a higher average valence state of Co ions on catalysts. As a result, having more Co<sup>3+</sup> species is advantageous for the redox characteristics and critical to the increase in catalytic activity (Fig. 4c). The Ce 3d spectra can be deconvoluted into 8 peaks, as shown in Fig. 4d, the bands label u<sub>2</sub> and v<sub>2</sub> represent 3d<sup>10</sup>4 f<sup>1</sup> corresponding to the initial electronic state of Ce<sup>3+</sup>, of which the peaks at 883.9 eV and 902.4 eV, while the peaks u<sub>1</sub>, u<sub>3</sub>, u<sub>4</sub>, v<sub>1</sub>, v<sub>3</sub>, v<sub>4</sub> represent the state of 3d<sup>10</sup>4 f<sup>0</sup> Ce<sup>4+</sup> ion, of which the peaks at 882.0, 888.5, 897.9, 900.6, 907.1 eV and 916.3 eV. The atomic ratio of Ce<sup>3+</sup> is determined by the peak area in Table 2, which shows that the relative concentration of Ce<sup>3+</sup> of CoMn<sub>2</sub>O<sub>4</sub>/CeTiO<sub>x</sub> (26.2%) is remarkably higher than CoMn<sub>2</sub>O<sub>4</sub>/CeO<sub>2</sub> (20.6%). This also indicates that Ti doping increases the oxygen defect of CeO<sub>2</sub> and promotes electron transport as the introduction of oxygen vacancy defect structure will break the dynamic balance of electrons and holes, so that a large number of electrons gather around oxygen vacancy, which is conducive to promoting the formation of active components [77]. In the process of REDOX reaction, gaseous oxygen molecules enter oxygen vacancy defects to capture electrons and form active oxygen components, while Ce<sup>3+</sup> loses electrons to form

Ce<sup>4+</sup>, forming a new dynamic equilibrium (Ce<sup>3+</sup> + O<sub>2</sub> → Ce<sup>4+</sup> + 2O<sup>•</sup>). Therefore, it can be said that the abundance of Ce<sup>3+</sup> will lead to the formation of unsaturated bonds and surface charge imbalance in the catalyst, increasing the number of oxygen vacancies, resulting in surface oxygen defects or the increase of hydroxyl groups. The XPS spectrum of the studied sample Ti 2p is also shown in Fig. 4e. The peak values are about 457.8 eV and 463.3 eV for Ti 2p<sub>3/2</sub> and Ti 2p<sub>1/2</sub>, respectively.

In multilayer structures, the conduction band is an important factor in determining the excitation potential of the guest layer and the ability to inject electrons into the main layer [78]. The valence band diagram is shown in Fig. 4g with the valence band maximum (VBM) values of CoMn<sub>2</sub>O<sub>4</sub>, CoMn<sub>2</sub>O<sub>4</sub>/CeO<sub>2</sub> and CoMn<sub>2</sub>O<sub>4</sub>/CeTiO<sub>x</sub> catalysts obtained by linear extrapolation were 0.58, 0.29 and 0.20 eV, respectively. The movements of VBM may be due to the change of the catalyst phase with the addition of Ce and Ti elements, thus generating additional molecular orbitals.

As an important species to evaluate the REDOX capacity of catalysts, O plays a crucial role in the adsorption and activation of subsequent reaction species. As shown in Fig. 4h, the XPS spectra of O 1s can be fitted into three sub-bands of O<sub>1</sub> (O<sub>lat</sub>), O<sub>2</sub> (O<sub>v</sub>) and O<sub>3</sub> (O<sub>ads</sub>), corresponding to binding energies of 529.2, 531.0 and 533.1 eV, belonging to lattice oxygen, oxygen vacancy and surface adsorbed oxygen respectively [79,80]. Compared with the original CoMn<sub>2</sub>O<sub>4</sub>, the content of oxygen defect (O<sub>2</sub>) in the catalyst supported by CeO<sub>2</sub> is significantly

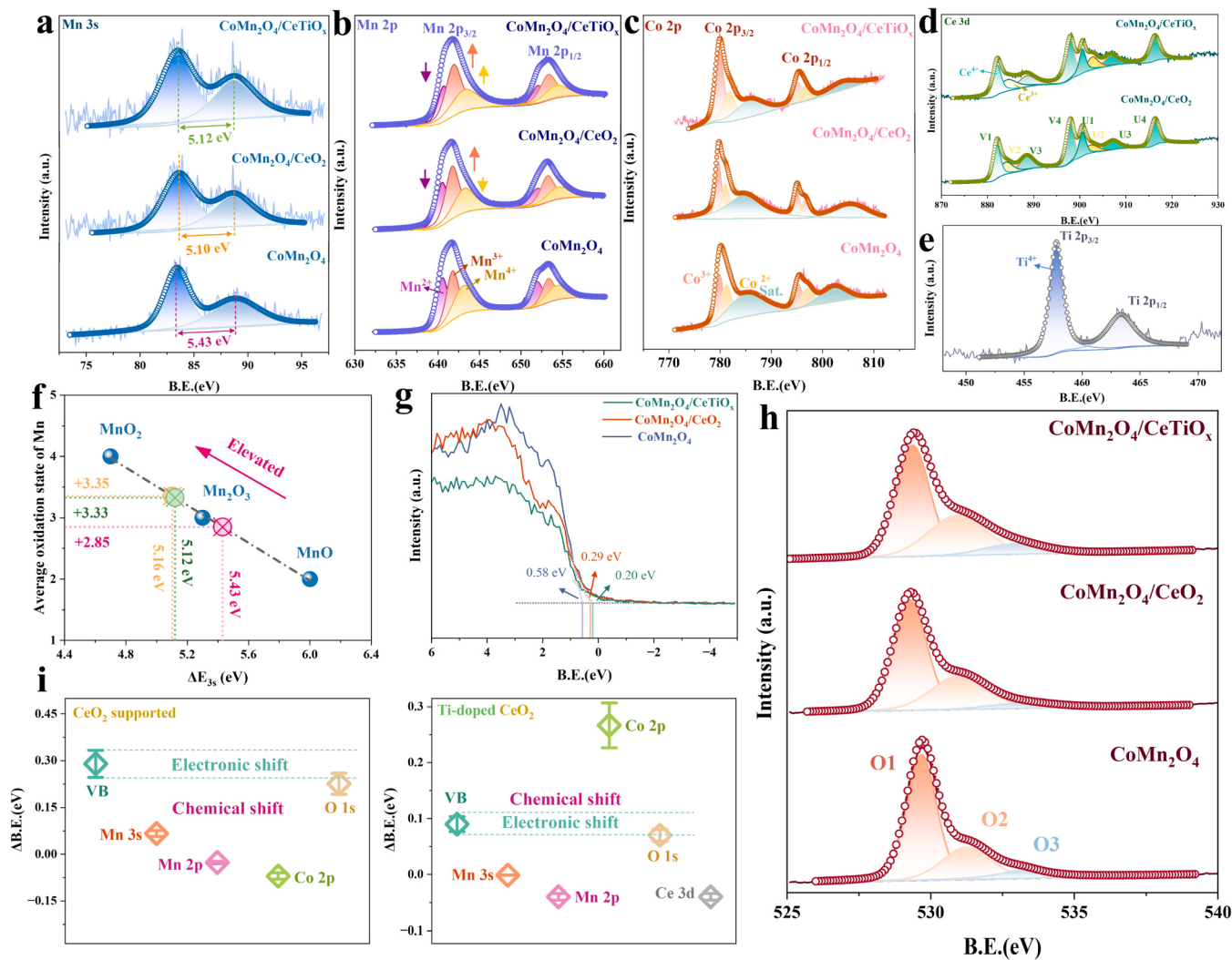


Fig. 4. XPS spectra of (a) Mn 3s, (b) Mn 2p, (c) Co 2p, (d) Ce 3d, (e) Ti 2p, (f) Average oxidation state of Mn, (g) Valence band (h) O 1s and (i) Shifting of binding energy in CoMn<sub>2</sub>O<sub>4</sub>, CoMn<sub>2</sub>O<sub>4</sub>/CeO<sub>2</sub> and CoMn<sub>2</sub>O<sub>4</sub>/CeTiO<sub>x</sub>.

increased, indicating that the introduction of  $\text{CeO}_2$  support produces more oxygen vacancies on the catalyst surface. In addition, with the doping of Ti, the oxygen defect content of the  $\text{CoMn}_2\text{O}_4/\text{CeTiO}_x$  catalyst increases obviously, which indicates that Ti can be used to adjust the defect content of catalyst. In addition, the percentage of  $\text{Ce}^{3+}$  can also characterize the oxygen vacancy (Fig. 4d, Table 3), and the results are consistent with O 1 s.

The displacement of binding energy in XPS can be divided into electronic shift and chemical shift, the former refers to the movement of Fermi energy level (work function) caused by some physical effects such as element doping, field effect and interface effect, while the latter refers to the movement caused by the change of elemental oxidation state, namely, valence. It has been found that the displacement of binding energy caused by Fermi level on the surface of transition metal shows the same trend in all bands of elements (including elemental orbital, oxide, valence band, etc) [81,82]. The change in valence is independent of the change in the element. The displacement of binding energy during catalysts was compared in Fig. 4i. It is found that the valence band spectrum and O 1 s show the same trend of changes, which may be attributed to the decrease of the Fermi level caused by the generation of a new interface [83]. In addition, the binding energy of other elements varies greatly and irregularly, which may be due to the displacement caused by the change in the oxidation state of elements. Therefore, it can be preliminarily speculated that there are both electronic and chemical shifts on the catalytic surface.

The charge transfer between the metal oxide and the carrier can regulate the chemical properties of the metal oxide (such as REDOX capacity) and thus its reactivity [84]. The XPS peak of O 1 s was further

analyzed (Fig. 4a) to determine the state of oxygen. The peak of 531–533 eV is attributed to oxygen vacancy and reactive oxygen species produced by adsorption and dissociation of nearby  $\text{O}_2$  molecules, and the peak of 529–531 eV is attributed to lattice oxygen [85]. Among them, the former can be regarded as the reactive oxygen species (ROS), which are considered to be highly active in SCR response [86]. It is worth noting that the order of ROS content is  $\text{CoMn}_2\text{O}_4/\text{CeTiO}_x$  (43.5%) >  $\text{CoMn}_2\text{O}_4/\text{CeO}_2$  (37.2%) >  $\text{CoMn}_2\text{O}_4$  (35.2%), which is consistent with the results of the SCR test. In addition, an oxygen vacancy is related to the chemical state and mobility of lattice oxygen [85]. Differences in reactive oxygen species between catalysts can be attributed to differences in the chemical state of lattice oxygen, which can be seen from the position of O1. The binding energy of O1 on  $\text{CoMn}_2\text{O}_4/\text{CeTiO}_x$  decreases after Ti doping, indicating that Ti doping could regulate the interfacial charge transfer between  $\text{CoMn}_2\text{O}_4$  and  $\text{CeO}_2$ , and improve the surface lattice oxygen reactivity of the  $\text{CoMn}_2\text{O}_4$  phase.

### 3.3.2. Electronic structure and oxidation state

The electronic structure and coordination states of Mn, Co and Ce were studied by X-ray absorption near edge structure (XANES) and extended X-ray adsorption fine structure (EXAFS) characterization (Fig. 5). The effects of loaded  $\text{CeO}_2$  and Ti doping on the oxidation state and local structure of Mn, Co and Ce were studied. The recorded Mn K-edge XANES spectra are shown in Fig. 5a, with weak peaks in the front edge region due to the 1 s→3d quadrupole transition (inlet), and the white lines characterized by the oxidation state of manganese are mainly in the octahedral environment [87,88]. According to the change of catalyst structure, the positions of 1 s→3d transition are at different

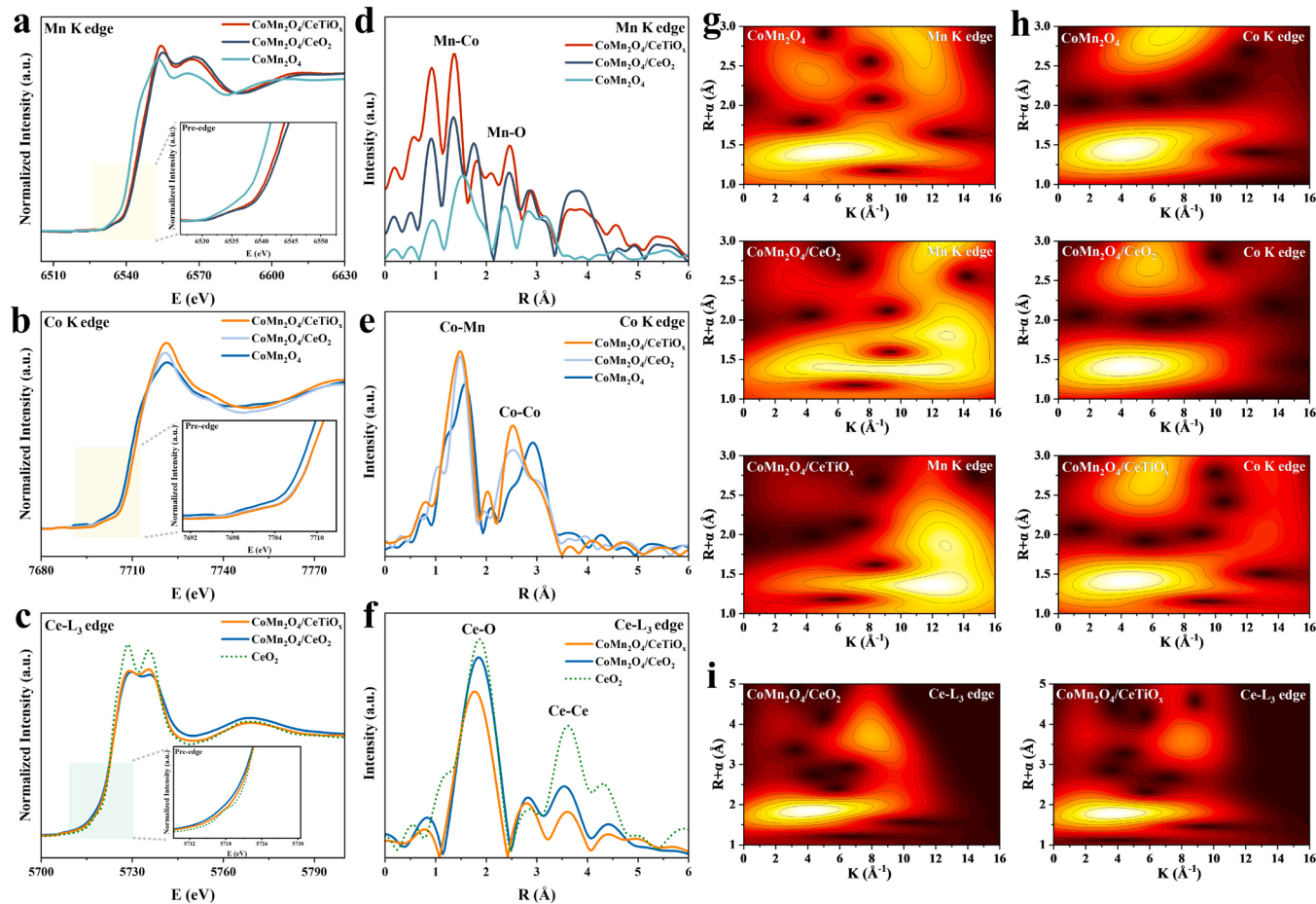


Fig. 5. EXAFS and XANES of Mn K-edge (a, d), Co K-edge (b, e), and Ce L<sub>3</sub>-edge (c, f); WT contour plots of Mn K-edge (g), Co K-edge (h) and Ce L<sub>3</sub>-edge (i) of three catalysts.

energies, so they represent different manganese oxidation states [89]. The addition of  $\text{CeO}_2$  support increases the average oxidation state of Mn, while the average oxidation state of Mn decreases when Ti is doped. In order to estimate the average oxidation state of manganese, the standard of Mn spectra ( $\text{Mn}$ ,  $\text{MnO}$ ,  $\text{Mn}_3\text{O}_4$ ,  $\text{Mn}_2\text{O}_3$ ,  $\text{MnO}_2$ ) was distributed with the Hephaestus software [B. Ravel and M. Newville, ATHENA, ARTEMIS, HEPAESTUS: data analysis for X-ray absorption spectroscopy using IFEFFIT, *Journal of Synchrotron Radiation* 12, 537–541 (2005)], and the results are shown in Fig. S4 [88]. The edge energy position and absorption threshold energy indicate that Mn is mainly  $\text{CoMn}_2\text{O}_4$  component close to  $\text{Mn}_3\text{O}_4$ . According to the chemometrics of  $\text{Mn}_3\text{O}_4$  phase, the average oxidation state of Mn is defined as 2.66. Therefore, the average oxidation state of  $\text{CoMn}_2\text{O}_4$  should be close to 2.66 (XPS:2.85). When  $\text{CeO}_2$  support is introduced, the average oxidation state of Mn increases between +3 and +4 (XPS:3.35), while when Ti is introduced, the average oxidation state of Mn decreases slightly, but was still higher than +3 (XPS:3.33). This result is consistent with the trend of XPS and H<sub>2</sub>-TPR, which further strengthens the explanation of Mn oxidation state.

Subsequently, the EXAFS spectrum was qualitatively evaluated. As shown in Fig. 5d, a main peak at 1.53 Å belongs to the Mn-Co scattering path, and several peaks between 2.0 and 3.0 Å mainly belongs to the Mn-O path, with some multiple scattering processes also contributing a small amount. R-space fitting determined that the coordination number (CNs) of Mn to O and Mn to Co are both 2, respectively (Fig. S5 and Table S4). The peaks of the catalyst shift after  $\text{CeO}_2$  introduced, and it can be seen from the wavelet transform diagram in Fig. 5g. The peak change more obviously after Ti doping, which may be related to the formation of metal-support surface between the carrier and the active component.

The Co-K-Edge X-ray absorption near-side structure (XANES) spectra of the three catalysts show very similar spectral patterns. After adding support, the absorbed energy of the catalyst moves slightly toward high energy, and the white line intensity (WL) increases (Fig. 5b), indicating that the average oxidation state of the supported catalyst  $\text{CeTiO}_x$  is higher than  $\text{CeO}_2$ . The EXAFS results (Fig. 5d) exhibit a main peak at 1.59 Å belongs to the Co-Mn scattering path, and peaks between 2.0 and 3.0 Å mainly belong to the Co-Co path, and the peaks higher than 3.0 Å belong to Co-O path. R-space fitting determines that the coordination number (CNs) of Co to Mn and Co to Co are both 2 and 4. The maximum intensity of the wavelet transform (WT) near 4 Å<sup>-1</sup> further demonstrates the Co-Mn coordination structure in the three samples.

To further investigate the effect of Ti doping on the carrier, the oxidation state of cerium was detected. Fig. 5c shows the XANES spectrum on the Ce L<sub>3</sub> side. For comparison, the standard reference spectrum of  $\text{Ce}^{4+}$  ( $\text{CeO}_2$ ) is also included (data source). The spectrum of  $\text{Ce}^{4+}$  has two absorption peaks near 5732.2 eV and 5739.0 eV, and the Ce L<sub>3</sub>-edge XANES spectrum of the catalyst is similar to that of  $\text{Ce}^{4+}$  in  $\text{CeO}_2$ . After Ti doping, the spectrum of  $\text{CeTiO}_x$  is only slightly shifted to low energy, which indicates that the average oxidation state is reduced, but it is still much higher than  $\text{Ce}^{3+}$ , because the spectrum of  $\text{Ce}^{3+}$  only exists a strong absorption peak near 5727.9 eV [73].  $\text{CeO}_2$  has a significant peak at 1.85 Å and a weak peak at 3.55 Å, which are attributed to Ce-O and Ce-Ce scattering paths, respectively. Considering that the WL intensity of oxides is usually proportional to the amount of coordination oxygen, compared with  $\text{CeO}_2$  support, Ce WL intensity of  $\text{CeTiO}_x$ -supported catalysts decreased, while Mn and Co gradually increased, indicating that oxygen species migrated significantly, which was consistent with the XPS results.

Overall, the shorter bond length of the Mn-Co/Co-Mn is primarily attributable to the influence of carrier. The interaction between the metal-support interfaces changes the structure of the active components, which improves their ability to interact with one another, shortens the electron transfer path, and accelerates the redox cycle. Additionally, Ti doping has mostly changed the Ce-O bond, indicating that Ti has successfully entered the  $\text{CeO}_2$  lattice. The carrier is made more stable by the

shorter metal-oxygen connection.

### 3.3.3. REDOX and acidic

To disclose the correlation between SCR performances and redox properties of the catalysts, the results of H<sub>2</sub>-TPR are presented in Fig. 6a. In the H<sub>2</sub>-TPR spectrum, the first peak at 220–240 °C is attributed to the reduction of oxygen adsorbed on the lattice defects. For the  $\text{CoMn}_2\text{O}_4$  catalyst, the second peak at 437 °C belongs to the co-existence of reduction of  $\text{MnO}_2$  to  $\text{Mn}_2\text{O}_3$  and  $\text{Mn}_3\text{O}_4$  and reduction of  $\text{Co}^{3+}$  to  $\text{Co}^{2+}$  [47,53]. The third peak at 624 °C belongs to the co-existence of reduction of  $\text{Mn}_3\text{O}_4$  to  $\text{MnO}$  and reduction of  $\text{Co}^{2+}$  to  $\text{Co}^0$  [47]. As for  $\text{CoMn}_2\text{O}_4/\text{CeO}_2$  catalyst, the reduction peaks blue shift from 281 °C to 574 °C, which is ascribed to the enhanced REDOX capacity of  $\text{CoMn}_2\text{O}_4$  phase and reduction of surface capping oxygen of  $\text{CeO}_2$  [73,90]. The new peak that appeared at 836 °C corresponded to the reduction of  $\text{Ce}^{4+}$  to  $\text{Ce}^{3+}$  and removal of bulk lattice oxygen of  $\text{CeO}_2$  which was extremely stable [76,90]. Notably, when Ti was doped into  $\text{CeO}_2$ , the spectra show a single peak width in the range of 645 °C, and the intensity is much higher than that of pure  $\text{CeO}_2$ , indicating a relatively high lattice oxygen mobility [73]. The enhancement of reducibility may be due to the interaction between  $\text{CeO}_2$  and  $\text{TiO}_2$  during the reduction process, which reduces the energy potential of oxygen anion migration, thus forming  $\text{Ce}_2\text{Ti}_2\text{O}_7$  pyrochlorite, which can achieve efficient oxygen anion transfer and promote the availability of bulk lattice oxygen. These results are consistent with earlier work by Luo et al. who showed that the reduction of  $\text{CeO}_2\text{-TiO}_2$  mixed oxides is greatly improved due to  $\text{TiO}_2$  incorporation into the  $\text{CeO}_2$  lattice [91]. Meanwhile, the reduction temperature of Ce decreases from 836 °C to 794 °C, while the temperature of 281 °C and 574 °C increases to 326 °C and 645 °C, indicating that the REDOX capacity of the  $\text{CoMn}_2\text{O}_4$  phase is inhibited, which also shows from another aspect that Ti doping regulation of REDOX properties can reduce the generation of by-products caused by excessive oxidation.

NH<sub>3</sub>-TPD is usually used to evaluate catalyst performance. Fig. 6b shows the profile and the relationship between the number of different acid sites on the catalyst and  $\text{NO}_x$  conversion, and three desorption peaks were observed in the range of 50–600 °C. The peaks belong to NH<sub>3</sub> adsorbed on weak (< 200 °C), medium-strong (200–350 °C), and strong (350–500 °C) acid sites respectively [76]. The adsorption amounts of NH<sub>3</sub> at the acid sites derived from the respective peak areas are presented in Fig. 6b.  $\text{CoMn}_2\text{O}_4$  catalysts are mainly weak (106 °C) and strong acid sites (372 and 454 °C), with a few medium strong acid sites (298 °C). After  $\text{CeO}_2$  is introduced, the weak acid sites increases straightly and the temperature shiftes to right (134 °C), strong acid sites decreases and shiftes to right (480 °C), and medium strong acid sites shiftes to the left (272 °C). It indicates that more weak acids adsorbed on the surface of the  $\text{CoMn}_2\text{O}_4/\text{CeO}_2$  catalyst. After Ti is added to the support, the weak acid sites decreases (121 °C) while the medium strong acid sites (304 °C) increases remarkably, indicating that strong interaction between Ti and Ce, resulting in big changes in acid sites distribution. Notably, the variation tendency of weak acid sites is in accordance with that of NH<sub>3</sub> adsorption on catalyst surface (Figs. 6b and 7a-c). Moreover, the number of strongly acidic sites for  $\text{CoMn}_2\text{O}_4/\text{CeTiO}_x$  catalysts also increased at relatively high temperatures (403 and 452 °C), which may be due to the exposure of appeared crystal faces of the catalyst leading to the desorption of NH<sub>3</sub> at new strong acid sites. In summary, medium-strong acid center had the most significant influence on the catalytic reaction.

Adsorption of NH<sub>3</sub> on the catalyst surface plays a key role in SCR reaction. NH<sub>3</sub>-adsorbed substances on the catalyst surface are obtained by in-situ diffuse infrared Fourier transform spectroscopy (DRIFTS) (Fig. 6c). The adsorption strength of NH<sub>3</sub> on the  $\text{CoMn}_2\text{O}_4/\text{CeO}_2$  catalyst is one order of magnitude higher than that of the other two catalysts, while  $\text{CoMn}_2\text{O}_4/\text{CeTiO}_x$  catalyst exhibits a decreased strength, the intensity and number of acid species are still higher than the that of the unsupported catalyst, indicating that Ti could have a good acid

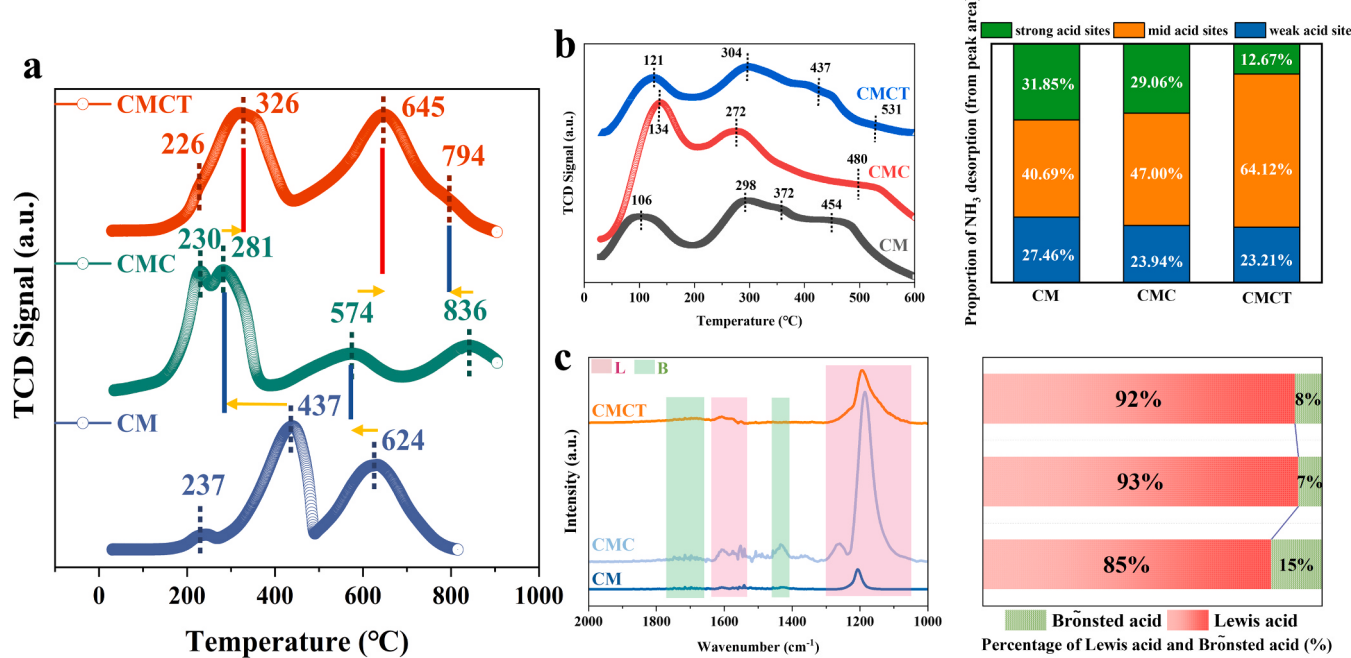


Fig. 6. (a) H<sub>2</sub>-TPR, (b) NH<sub>3</sub>-TPD and (c) DRIFT spectra of NH<sub>3</sub> adsorbed of CoMn<sub>2</sub>O<sub>4</sub>, CoMn<sub>2</sub>O<sub>4</sub>/CeO<sub>2</sub> and CoMn<sub>2</sub>O<sub>4</sub>/CeTiO<sub>x</sub>.

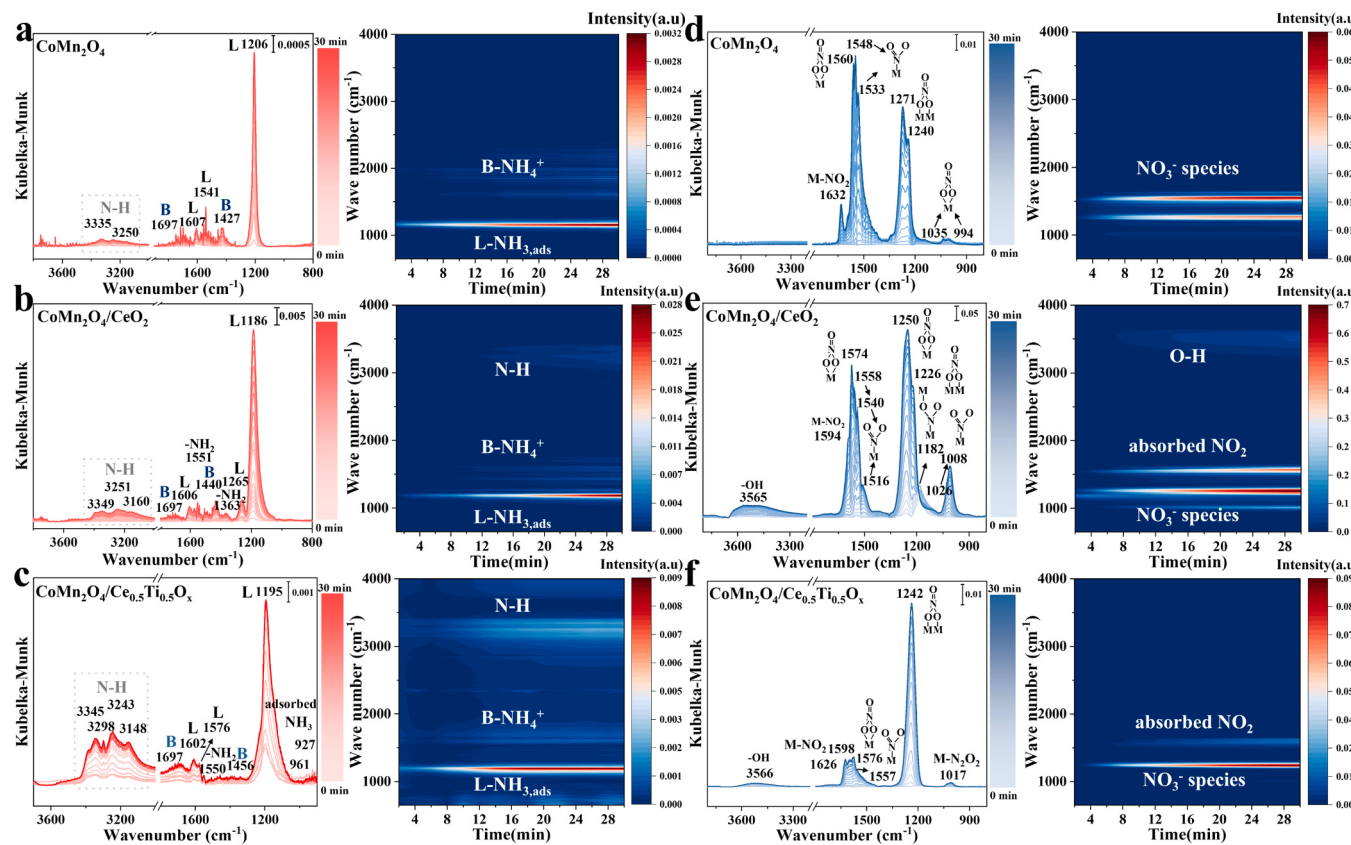


Fig. 7. In situ DRIFTS spectra of NH<sub>3</sub> adsorption (a)-(c), NO+O<sub>2</sub> co-adsorption (e)-(f) in different time at 150 °C over CoMn<sub>2</sub>O<sub>4</sub>, CoMn<sub>2</sub>O<sub>4</sub>/CeO<sub>2</sub> and CoMn<sub>2</sub>O<sub>4</sub>/CeTiO<sub>x</sub> catalysts.

regulation effect. The peaks near 1180–1250, 1607 cm<sup>-1</sup> belong to NH<sub>3</sub> species bound to Lewis acid sites, while peaks around 1456, 1680–1700 cm<sup>-1</sup> are attributed to NH<sub>4</sub><sup>+</sup> bound to Brønsted acid sites, and peaks near 1355 cm<sup>-1</sup> are attributed to -NH<sub>2</sub> species. Combined

with the results of NH<sub>3</sub> adsorption and desorption spectra of the above catalyst, it can be determined that the addition of CeO<sub>2</sub> support can improve the acidity of the catalyst to a large extent, when Ti doping CeO<sub>2</sub> support, the weak acidity of the catalyst can be adjusted, but more

stable medium-strong acid sites can be generated. This may be attributed to the fact that the doping of Ti causes or enhances the interfacial interaction between the carrier and the active component, exposing new active crystal planes, thus improving the catalytic activity.

### 3.4. Reaction mechanisms of $\text{NH}_3$ -SCR

#### 3.4.1. DRIFTS study $\text{NH}_3$ or $\text{NO} + \text{O}_2$ adsorption

The adsorption of  $\text{NH}_3$  and  $\text{NO}_x$  is a critical step involved in the reduction of  $\text{NO}_x$ , and the in situ DRIFTS of  $\text{NH}_3/\text{NO}_x$  adsorption by catalysts at 150 °C are recorded in Fig. 7. With increasing  $\text{NH}_3$  adsorption time, several vibrational bands appear for  $\text{CoMn}_2\text{O}_4$  catalysts at 3335, 3250, 1697, 1607, 1541, 1427 and 1206  $\text{cm}^{-1}$  (Fig. 7a). The negative bands between 3000 and 3400  $\text{cm}^{-1}$  (3313 and 3149  $\text{cm}^{-1}$ ) are related to the N-H stretching vibration region of the coordinated  $\text{NH}_3$  [34]. Meanwhile, the catalyst surface is covered by the adsorbed  $\text{NH}_3$  species including  $\text{NH}_3$  linked to Lewis acid (1206, 1541 and 1607  $\text{cm}^{-1}$ ) [92,93] and  $\text{NH}_4^+$  on Brønsted acid sites (1427 and 1697  $\text{cm}^{-1}$ ) [39]. As for  $\text{CeO}_2$  supported catalyst (Fig. 7b), the number of adsorbed  $\text{NH}_3$  species on the Lewis and Brønsted acid sites are significantly increased with increasing adsorption time. Two new spectral bands appeared at 3160, 1265, 1551 and 1363  $\text{cm}^{-1}$  assign to N-H stretching band, coordinated  $\text{NH}_3$  adsorbed at the Lewis acid sites and  $-\text{NH}_2$  belonged to the oxidation of adsorbed ammonia, respectively [12,22,94,95]. Also, the intensity of all  $\text{NH}_3$  absorption peaks increase by tens of times. When Ti-doped with  $\text{CeO}_2$  carriers (Fig. 7c), new kinds of acidic sites appear, which is consistent with the description of  $\text{NH}_3$ -TPD. Among them, the Lewis peak from 1576  $\text{cm}^{-1}$ , N-H-related band in 3298  $\text{cm}^{-1}$  and weakly adsorbed  $\text{NH}_3$  correspond to 927 and 961  $\text{cm}^{-1}$  are displayed [21,34]. These results indicate that the introduction of the  $\text{CeTiO}_x$  carrier can enhance the number of Lewis and Brønsted acid sites and promote the activation of  $\text{NH}_3$  adsorption, thus improving  $\text{NH}_3$ -SCR activity.

Fig. 7d-f show the results of in situ DRIFTS to study the adsorption of  $\text{NO} + \text{O}_2$  on catalysts. On the  $\text{CoMn}_2\text{O}_4$  catalyst (Fig. 7d), several distinct bands located at 994, 1035, 1240, 1271, 1533, 1548, 1564, 1632  $\text{cm}^{-1}$  are observed when the  $\text{NO} + \text{O}_2$  is introduced at 150 °C, which are assigned to bridged nitrate (1240, 1271 and 1632  $\text{cm}^{-1}$ ) [96–98], bidentate nitrate (994, 1035 and 1560  $\text{cm}^{-1}$ ) [22,25] monodentate nitrite (1533 and 1548  $\text{cm}^{-1}$ ) [22,47,99] and  $\text{M-NO}_2$  nitro compounds (1632  $\text{cm}^{-1}$ ) [98], respectively. And the band at 3700–3600  $\text{cm}^{-1}$  is assigned to the surface -OH species that appeared [34]. According to the peak intensity and peak area, the order of nitrate species content could be estimated as single monodentate nitrate > bidentate nitrate > bridging nitrate [100]. It is noteworthy that the intensities of the adsorbed  $\text{NO}_x$  species are much stronger than those of the adsorbed  $\text{NH}_3$  species. On the  $\text{CoMn}_2\text{O}_4/\text{CeO}_2$  catalyst (Fig. 7d), the variation of the spectral bands is more different from that of the  $\text{CoMn}_2\text{O}_4$  catalyst, with the bands of bridged nitrate (1226  $\text{cm}^{-1}$ ), bidentate nitrate (1574 and 1250  $\text{cm}^{-1}$ ) [17], monodentate nitrite (1008, 1026, 1516, 1540, 1558  $\text{cm}^{-1}$ ) [17,99,101],  $\text{M-NO}_2$  nitro compounds (1594  $\text{cm}^{-1}$ ), and hydroxyl group (3565  $\text{cm}^{-1}$ ), respectively. The chelating nitrite species (1182  $\text{cm}^{-1}$ ) that appear at the beginning of the adsorption reaction and then disappear with the extension of the reaction time, indicating that these nitrate species initially presented in an unstable state but eventually oxidized to a stable state [102]. By contrast, fewer species but stronger intensities of  $\text{NO}_x$  related species adsorb on  $\text{CoMn}_2\text{O}_4/\text{CeTiO}_x$  catalysts compared to the above two kinds of catalysts. In other words,  $\text{NO}_x$  is adsorbed on the catalyst surface to form bidentate nitrate (1576  $\text{cm}^{-1}$ ), bridge nitrate species (1242  $\text{cm}^{-1}$ ) and monodentate nitrite (1557  $\text{cm}^{-1}$ ) [22,17,103]. Besides,  $\text{M-NO}_2$  nitro compounds (1598 and 1626  $\text{cm}^{-1}$ ) and  $\text{cis-N}_2\text{O}_2^2$  (1017  $\text{cm}^{-1}$ ) are detected. Overall, these adsorbed  $\text{NO}_x$  species gradually strengthened in intensity with the prolonged exposure time for all three catalysts, suggesting that abundant nitrate species are formed and accumulated. The thermal stability of these materials is in order of linear monodentate nitrate < bridged

nitrite < monodentate complex nitrite < monodentate nitrate < bridged bidentate nitrate < chelated bridged nitrate [101]. These adsorbed nitrites and nitrates have high activity on the surface of the catalyst, react with  $\text{NH}_3$  to form  $\text{NH}_4\text{NO}_3$ , and finally decompose into  $\text{N}_2\text{O}$  and  $\text{N}_2$ , making important contributions to the activity of the catalyst. Among which  $\text{CoMn}_2\text{O}_4/\text{CeO}_2$  possessed substantially more adsorbed  $\text{NO}_x$  species, but a catalyst supported by  $\text{CeTiO}_x$  has strong adsorption performance for nitrate and migrates to more stable species, which weakens the adsorption of other kinds of nitrate and provide more active sites for  $\text{NH}_3$  adsorption. This may be the main reason for the improvement of catalyst performance.

#### 3.4.2. Reaction between $\text{NO} + \text{O}_2$ and $\text{NH}_3$

To understand the reaction mechanism contributing to the different catalytic activity of catalysts, in situ DRIFTS analysis of  $\text{NH}_3$  followed by  $\text{NO} + \text{O}_2$  co-adsorption and co-adsorption  $\text{NO} + \text{O}_2$  followed by  $\text{NH}_3$  were applied to test the transient behaviors of  $\text{NH}_3$  and  $\text{NO} + \text{O}_2$ . And the reactivity of the catalysts at different times at 150 °C is presented in Fig. 8, and Table S5.

**3.4.2.1.  $\text{CoMn}_2\text{O}_4$  catalysts.** Over the surface of the  $\text{CoMn}_2\text{O}_4$  sample, as shown in Fig. 8a, after 500 ppm  $\text{NH}_3$  balanced by  $\text{N}_2$  is introduced for 30 min, several peaks attributed to the adsorbed  $\text{NH}_3$  species appear. When switching to 500 ppm  $\text{NO} + 8 \text{ vol\% O}_2$ , it is observed that the intensities of the adsorbed  $\text{NH}_3$  species (except Brønsted acid sites in 1432 and 1697  $\text{cm}^{-1}$ ) weaken with increasing time and gradually vanish in 10 min, indicating that these adsorbed  $\text{NH}_3$  species in Lewis acid sites are reactive and can participate in the  $\text{NH}_3$ -SCR reaction. Meanwhile, the bands of surface nitrate species gradually appear and accumulate, with bidentate nitrate (1556  $\text{cm}^{-1}$ ) and monodentate nitrates (1533 and 1540  $\text{cm}^{-1}$ ) corresponding to the peaks that exist in co-adsorption of 500 ppm  $\text{NO} + 8 \text{ vol\% O}_2$  but with a slight shift. Notably, the adsorption signal peaks of  $\text{M-NO}_2$  nitro compounds (1632  $\text{cm}^{-1}$ ), bridge nitrate species (1240 and 1271  $\text{cm}^{-1}$ ) and bidentate nitrate (994, 1035  $\text{cm}^{-1}$ ) are not detected, but new peaks of monodentate nitrates (1457  $\text{cm}^{-1}$ ) and  $\text{cis-N}_2\text{O}_2^2$  (1015  $\text{cm}^{-1}$ ) emerge [22,47,99,104]. This may be associated with  $\text{NO}$  adsorption sites that are occupied by ammonia [105]. The additional bands ascribe to nitrate intermediates  $\text{NH}_4\text{NO}_3$  located at 1524  $\text{cm}^{-1}$  (overlaps with 1531  $\text{cm}^{-1}$  monodentate nitrates) and 1245  $\text{cm}^{-1}$  showed up, indicating that there exists a pathway for the formation of intermediate active species [99].

Similar bands assigned to  $\text{NH}_4\text{NO}_3$  also showed up after the introduction of 500 ppm  $\text{NH}_3$  when 500 ppm  $\text{NO} + 8 \text{ vol\% O}_2$  is supplied successively for 30 min in the simulating gas in Fig. 8b. When reversing the sequence of gas to  $\text{NH}_3$ , the absorption bands intensities of nitrate species weaken or vanish significantly until stable with increasing time. In which, the  $\text{M-NO}_2$  nitro compounds (1632  $\text{cm}^{-1}$ ) and bidentate nitrate (994, 1035 and 1560  $\text{cm}^{-1}$ ) almost completely disappeared, the bridge nitrate species (1240 and 1271  $\text{cm}^{-1}$ ) are consumed gradually and may overlap with a growing band of 1245  $\text{cm}^{-1}$  linked to  $\text{NH}_4\text{NO}_3$ , the monodentate nitrates (1533 and 1540  $\text{cm}^{-1}$ ) reacted slowly and showed a blue shift towards 1518 and 1537  $\text{cm}^{-1}$ , Otherwise, after enlarging from Fig. 8b, and the new peaks attributing to coordinated  $\text{NH}_3$  on the Lewis acid sites (1427  $\text{cm}^{-1}$ ),  $\text{NH}_4^+$  species on the Brønsted acid sites (1697  $\text{cm}^{-1}$ ), and N-H stretching vibration modes of  $\text{NH}_3$  (3335, 3257  $\text{cm}^{-1}$ ) are observed. These results demonstrate that part of nitrate species eventually formed the dominant unstable nitrate/  $\text{NH}_4\text{NO}_3$  species to participate in the  $\text{NH}_3$ -SCR reaction. This intermediate is fairly stable at low temperatures, which could block the effective active sites, thus reducing the activity of the catalyst in the  $\text{NH}_3$ -SCR reaction at low temperatures [106]. Overall, the adsorption strength of  $\text{NO}_x$  on the catalyst surface is higher than that of  $\text{NH}_3$ . During the reaction, it was observed that adsorbed species at the Lewis acid sites participated in the SCR reaction more quickly than those at the Brønsted acid site, which may also relate to the higher proportion of L acid on the

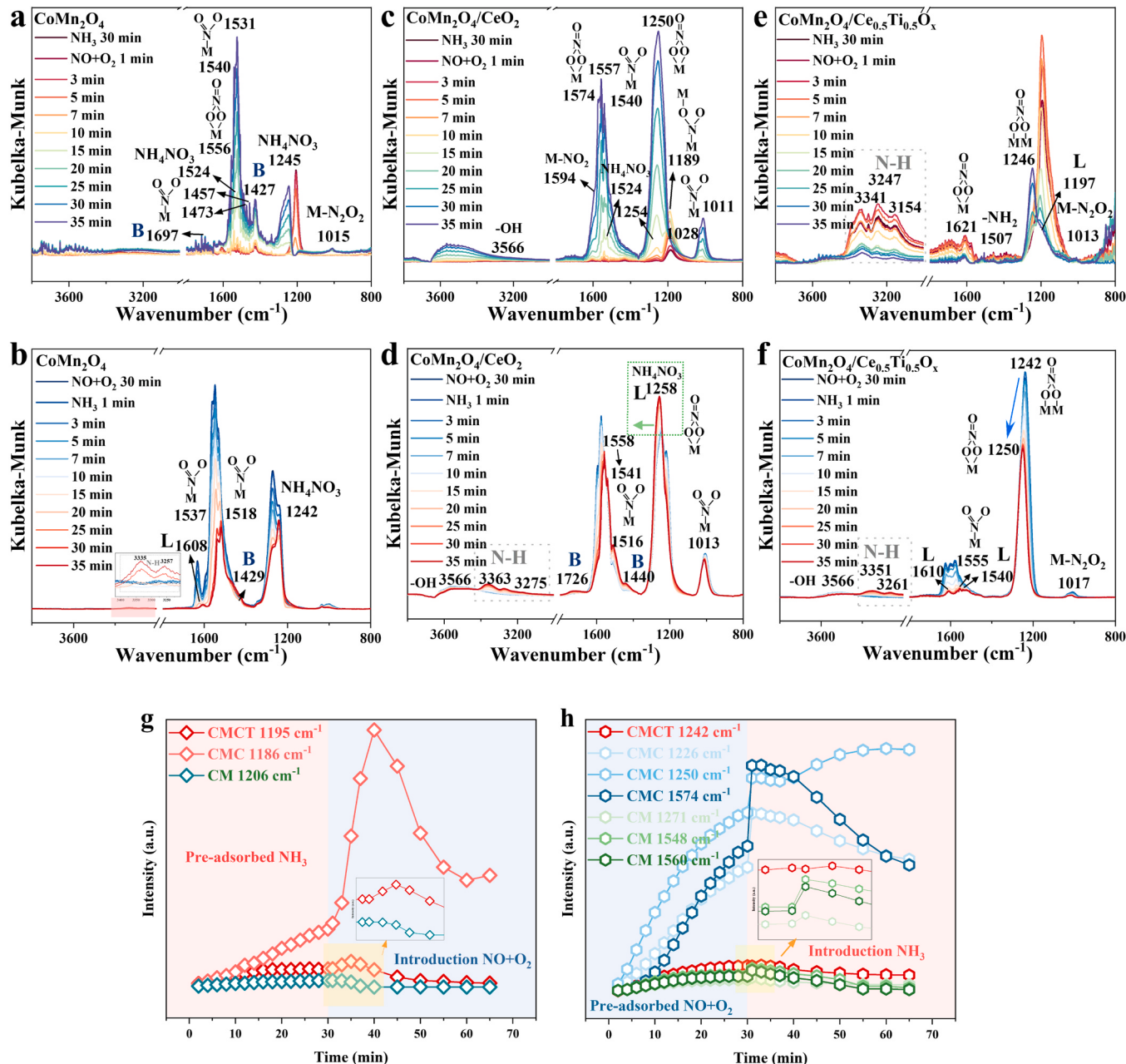


Fig. 8. In situ DRIFTS spectra of  $\text{NH}_3$  reacted with pre-adsorbed  $\text{NO} + \text{O}_2$  species and  $\text{NO} + \text{O}_2$  reacted with pre-adsorbed  $\text{NH}_3$  species at a different time at  $150^\circ\text{C}$  over  $\text{CoMn}_2\text{O}_4$  (a)-(b),  $\text{CoMn}_2\text{O}_4/\text{CeO}_2$  (c)-(d) and  $\text{CoMn}_2\text{O}_4/\text{CeTiO}_x$  (e)-(f) catalysts, and changes of main peak intensity on the catalyst surface (g)-(h).

catalyst surface (Fig. 7d). This indicates that  $\text{NH}_3$  exists in the form of  $-\text{NH}_2$  and  $\text{H}^+$ , and the adsorbed ammonia reacts quickly with gaseous  $\text{NO}/\text{NO}_2$ . After adsorption and saturation of  $\text{NH}_3$ , it further reacts with  $\text{NO}$  to form  $\text{N}_2$  and  $\text{H}_2\text{O}$ , indicating that adsorbed  $\text{NO}_x$  reacts with gaseous  $\text{NH}_3$ , which proves the existence of Langmuir-Hinshelwood (L-H) reaction mechanism. The order of peak intensity of nitrate was as follows: bidentate nitrate > bridge nitrate > monodentate nitrate.

**3.4.2.2.  $\text{CoMn}_2\text{O}_4/\text{CeO}_2$  catalysts.** Obvious differences in the reaction process were manifested on  $\text{CeO}_2$  supported  $\text{CoMn}_2\text{O}_4$  catalyst. Fig. 8c illustrates the in-situ DRIFTS of  $\text{NO} + \text{O}_2$  after pre-exposure of the catalyst to  $\text{NH}_3$  at  $150^\circ\text{C}$ . When  $\text{NO}$  and  $\text{O}_2$  are introduced, the prominent peaks ascribed to  $\text{NH}_3$  species decrease significantly and generate nitrate species in 1 min, and the reaction rate of the adsorbed  $\text{NH}_3$  species with  $\text{NO}$  over the supported  $\text{CoMn}_2\text{O}_4/\text{CeO}_2$  sample is more quickly than those on the  $\text{CoMn}_2\text{O}_4$  sample. The following species

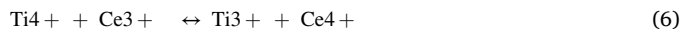
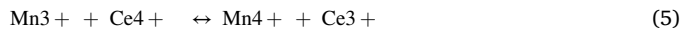
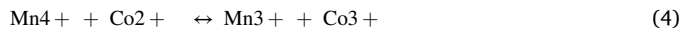
mainly including strengthening of bidentate nitrate ( $1574$  and  $1250 \text{ cm}^{-1}$ ), monodentate nitrate ( $1011$ ,  $1028$ ,  $1540$ ,  $1557 \text{ cm}^{-1}$ ) and chelating nitrite ( $1189 \text{ cm}^{-1}$ ) gradually transferred to stable nitrate species on the catalyst surface, which is consistent with the adsorption species of  $\text{NO} + \text{O}_2$  despite the slight displacement. The occurrence of displacement may be related to the emergence of nitrate intermediates such as  $\text{NH}_4\text{NO}_3$  ( $1574$  and  $1250 \text{ cm}^{-1}$ ) in the initial stage and the peaks gradually merged in the bands of nitrate species. This indicates nitrogen oxides can react with adsorbed ammonia in the  $\text{NH}_3$ -SCR reaction and present an obvious E-R mechanism. However, gaseous  $\text{NO}_2$  molecules ( $1594 \text{ cm}^{-1}$ ) part of monodentate nitrate ( $1516 \text{ cm}^{-1}$ ) did not appear, which might be associated with the good reactivity of weakly adsorbed nitrate or competitive adsorption between  $\text{NO}_x$  and  $\text{NH}_3$ .

Switch the gas intake sequence,  $\text{NO} + \text{O}_2$  were pre-adsorbed on the sample at  $150^\circ\text{C}$  for 30 min, then  $\text{NH}_3$  was introduced, and the results are shown in Fig. 8d. After being exposed to  $\text{NO} + \text{O}_2$ , the surface of the

sample is covered by several  $\text{NO}_x$  species, when switching to  $\text{NH}_3$ , the bands intensities of nitrate species are almost unchanged, yet accompanied by the complete disappearance of  $\text{M-NO}_2$  nitro compounds ( $1594 \text{ cm}^{-1}$ ), a small decrease of bidentate nitrate ( $1574$  and  $1250 \text{ cm}^{-1}$ ), bridge nitrate ( $1226 \text{ cm}^{-1}$ ) and monodentate nitrate ( $1013$  and  $1558 \text{ cm}^{-1}$ ) and slight migration of bidentate nitrate ( $1258 \text{ cm}^{-1}$ ) with increasing time. Then several new peaks ascribed to the adsorbed  $\text{NH}_3$  species are observed after 7 min. Meanwhile, the overlapping peaks of bidentate nitrate ( $1250 \text{ cm}^{-1}$ ),  $\text{NH}_4\text{NO}_3$  ( $1254 \text{ cm}^{-1}$ ), and Lewis acid sites ( $1265 \text{ cm}^{-1}$ ) kept increasing in  $1258 \text{ cm}^{-1}$  as the reaction goes on, which is related to the reaction of adsorbed bidentate nitrate with adsorbed  $\text{NH}_3$  substance to form  $\text{NH}_4\text{NO}_3$ . Therefore, gaseous  $\text{NO}_2$  and bridging nitrates are considered as the main active substances, and they are easy to react with adsorbed  $\text{NH}_3$  to generate  $\text{N}_2$  and  $\text{H}_2\text{O}$ , while monodentate nitrates are less reactive. This further supports the dominance of E-R mechanisms, while L-H mechanisms account for a small proportion. In addition, the carrier  $\text{CeO}_2$  not only promotes the dispersion of active species but also exists the electronic interaction behaviors over the metal-support interface.

**3.4.2.3.  $\text{CoMn}_2\text{O}_4/\text{CeTiO}_x$  catalysts.** Different from the above two catalysts, the adsorption and activation conversion capacity of  $\text{NH}_3$  on the surface of the  $\text{CoMn}_2\text{O}_4/\text{CeTiO}_x$  catalyst is much higher than that of  $\text{NO}_x$  species (Fig. 8e). Specifically, when  $\text{NO}+\text{O}_2$  are introduced after the pre-adsorption of for 30 min on the catalyst, the intensities of adsorbed  $\text{NH}_3$  species decreases rapidly, nevertheless, some characteristic bands of adsorbed  $\text{NH}_3$  species still exist, indicating that the  $\text{NH}_3$  species on the catalyst surface are not completely consumed after 30 min  $\text{NO}+\text{O}_2$  treatment. Meanwhile, the nitrate species of bidentate nitrate ( $1621 \text{ cm}^{-1}$ ), bridged nitrate ( $1246 \text{ cm}^{-1}$ ) and *cis*- $\text{N}_2\text{O}_2$  ( $1013 \text{ cm}^{-1}$ ) are observed and stabilized gradually. Moreover, the new peak at  $1507 \text{ cm}^{-1}$  ascribed to the  $\text{NH}_2$  species is also detected, which may be related to the oxidation of  $\text{NH}_3$  adsorption [107].

Reverse the order of simulating gas, the adsorbed nitrate species at  $150^\circ\text{C}$  and corresponding results are shown in Fig. 8f. After the introduction of  $\text{NH}_3$ , the band intensity of the corresponding  $\text{M-NO}_2$  adsorption species ( $1598$ ,  $1626 \text{ cm}^{-1}$ ), bidentate nitrate ( $1576 \text{ cm}^{-1}$ ), and -OH hydroxyl band ( $3566 \text{ cm}^{-1}$ ) decline and diminish rapidly. The monodentate nitrate ( $1555 \text{ cm}^{-1}$ ) and *cis*- $\text{N}_2\text{O}_2^{\cdot-}$  ( $1017 \text{ cm}^{-1}$ ) react quickly but not completely, and the bridged nitrate ( $1242 \text{ cm}^{-1}$ ) transfers to stable bidentate nitrate ( $1250 \text{ cm}^{-1}$ ) with increasing time. With the consumption of the nitrate species, the peaks of the coordinated  $\text{NH}_3$  on Lewis acid sites ( $1540$  and  $1610 \text{ cm}^{-1}$ ) and N-H stretching vibration ( $3351$  and  $3261 \text{ cm}^{-1}$ ) appear. It is noteworthy that no nitrate intermediates were detected during the transient reaction, which may be related to the path of rapid reaction. These results showed that the adsorbed  $\text{M-NO}_2$  species and bidentate nitrate had higher activity. Besides, the coexistence of  $\text{NH}_3$  and  $\text{NO}$  indicated that they adsorbed at different sites of the  $\text{CoMn}_2\text{O}_4/\text{CeTiO}_x$  catalyst. Moreover, there are more cyclic interactions of electron pairs on the catalyst surface.



In addition, it is suggested that bidentate nitrate is the main reactive species, while  $\text{SO}_2$  had little effect on the formation of bidentate nitrate, but would completely inhibit the production of monodentate nitrite. This may be the reason why the catalyst has excellent resistance to  $\text{SO}_2$  [108].

It can be seen from the changes of major peaks on the catalyst surface that  $\text{NH}_3$  adsorption is strongest in the reaction of  $\text{NO}+\text{O}_2$  after  $\text{NH}_3$  pre-adsorption, but the  $\text{NH}_3$  adsorption peak at  $\text{CoMn}_2\text{O}_4/\text{CeO}_2$  at  $1186 \text{ cm}^{-1}$  after the introduction of  $\text{NO}$  does not rapidly disappear, but rapidly increases and then weakens, which may be due to the generation

of unstable nitrate species and the process of gradually transforming into stable nitrate. Compared with  $\text{CoMn}_2\text{O}_4$ , the  $\text{NH}_3$  adsorption peak of  $\text{CoMn}_2\text{O}_4/\text{CeTiO}_x$  weakens and disappears faster. And in the reaction of  $\text{NH}_3$  after  $\text{NO}+\text{O}_2$  pre-adsorption, the intensities of most main peaks of nitrate species in  $\text{CoMn}_2\text{O}_4$  and  $\text{CoMn}_2\text{O}_4/\text{CeO}_2$  catalysts raise briefly and then decrease gradually, indicating that the adsorbed nitrate species react and were consumed with  $\text{NH}_3$ . And an increased peak at  $1250 \text{ cm}^{-1}$  of  $\text{CoMn}_2\text{O}_4/\text{CeO}_2$  rose slowly, contributing to the formation of new ammonium nitrate species. Compared with the above two catalysts,  $\text{CoMn}_2\text{O}_4/\text{CeTiO}_x$  adsorbed fewer types of nitrates and exhibited lower adsorption strength. Moreover, when  $\text{NH}_3$  is introduced, the main peak site decreased less, indicating that the reaction between nitrate species and ammonia is weak.

### 3.4.3. $\text{SO}_2$ -tolerant mechanisms

In situ DRIFTS were used to compare the adsorption properties of  $\text{SO}_2$  on the catalysts, as shown in Figs. 9–10 and Table S6. The results of  $\text{SO}_2 + \text{O}_2$  adsorption at  $150^\circ\text{C}$  are shown in Fig. 9a–c. After exposure to  $\text{SO}_2 + \text{O}_2$ , the peaks of different  $\text{SO}_2$  adsorption species appear on the three catalysts. On the  $\text{CoMn}_2\text{O}_4$ , the peaks attributed to the  $\text{HSO}_4^-$  ( $1619 \text{ cm}^{-1}$ ) from the reaction between  $\text{SO}_2$  and surface hydroxyl groups,  $\text{S=O=S}$  ( $1166$ ,  $1235$  and  $1339 \text{ cm}^{-1}$ ) and O-S-O species ( $1047 \text{ cm}^{-1}$ ) located in  $1000$ – $1400 \text{ cm}^{-1}$  of the bidentate sulfate-metal surface complex formed by adsorbed  $\text{SO}_2$  and metal oxides are detected [76,109,110]. In contrast, it can be concluded that the adsorption capacity of  $\text{SO}_2$  on the surface of the  $\text{CoMn}_2\text{O}_4/\text{CeO}_2$  catalyst is stronger than that of  $\text{CoMn}_2\text{O}_4$ , except for minority peaks ( $1225$  and  $1339 \text{ cm}^{-1}$ ), other sulfate peaks associated to  $\text{CoMn}_2\text{O}_4$  catalyst are diminished. Meanwhile,  $\text{SO}_{2-4}$  and  $\text{SO}_3$  linked to Ce atom species ( $1004$ ,  $1115$  and  $1539 \text{ cm}^{-1}$ ) appear and accumulate, indicating that  $\text{SO}_2$  more easily adsorbed on the Ce atoms, so it is considered as a good candidate for the sacrifice sites for active components [109]. It should be noted that the band ascribed to weakly adsorbed  $\text{SO}_3$  has shifted to the highest frequency band  $1545 \text{ cm}^{-1}$  from  $1400 \text{ cm}^{-1}$  may be due to the physical adsorption having changed under different situations [111]. In addition, the gradual increase of -OH species indicates that the appearance of cerium sulfate increases the Brønsted acid site. These results indicate that the addition of ceria might lead to more bulk-like sulfates. Furthermore, the types and amounts of sulfate form less after Ti-doped in  $\text{CeO}_2$ , indicating that  $\text{CoMn}_2\text{O}_4/\text{CeTiO}_x$  has a lower degree of sulfation as the decrease of sulfates and  $\text{SO}_x$ . Unlike before, the characteristic sulfate peaks associated with  $\text{CoMn}_2\text{O}_4$  and Ce were not present, instead is  $\text{SO}_2$  and sulfate species associated with Ti were investigated ( $1040$ ,  $1135$  and  $1252 \text{ cm}^{-1}$ ), implying that Ti also has a good absorption affinity for  $\text{SO}_2$  [112,113]. According to the above results, it can be inferred that  $\text{SO}_2$  preferentially adsorbed on the carrier rather than the active component, and preferentially adsorbed on the Ti site in the dual-component carrier, that is, the attraction of  $\text{CeTiO}_x$  phase to  $\text{SO}_2$  is higher than that of  $\text{CeO}_2$  phase. The excellent sulfate resistance may be attributed to the presence of  $\text{SO}_2$  double adsorption sites, which is more conducive to delaying the binding of  $\text{SO}_2$  to the active sites, and the layered structure of supports can effectively increase the contact area with the gas flow and trap the  $\text{SO}_2$ , thus weaken the formation and accumulation of sulfate on the active sites of catalysts.

To investigate the interaction between gas components, the effect of  $\text{SO}_2 + \text{O}_2$  adsorption on the adsorption capacity of  $\text{NH}_3$  on the catalyst surface was investigated by in-situ drift. As can be seen from Fig. 9d–f, when  $\text{NH}_3$  is introduced, the sulfate species on the surface of the three catalysts do not disappear, and some peaks are strengthened or migrated. It shows that  $\text{NH}_3$  gas reacts with adsorbed  $\text{SO}_2$  to form ammonium sulfide species, which is deposited on the catalyst surface. The difference is that a small amount of Lewis acid species adsorbed by  $\text{NH}_3$  ( $1195 \text{ cm}^{-1}$ ) and more N-H bond peaks ( $3100$ – $3400 \text{ cm}^{-1}$ ) appear on the surface of the  $\text{CoMn}_2\text{O}_4/\text{CeTiO}_x$  catalyst.

To clearly illustrate the mechanism of  $\text{SO}_2$  resistance and compare the effect of  $\text{SO}_2$  on the  $\text{NH}_3/\text{NO} + \text{O}_2$  adsorption performance of the

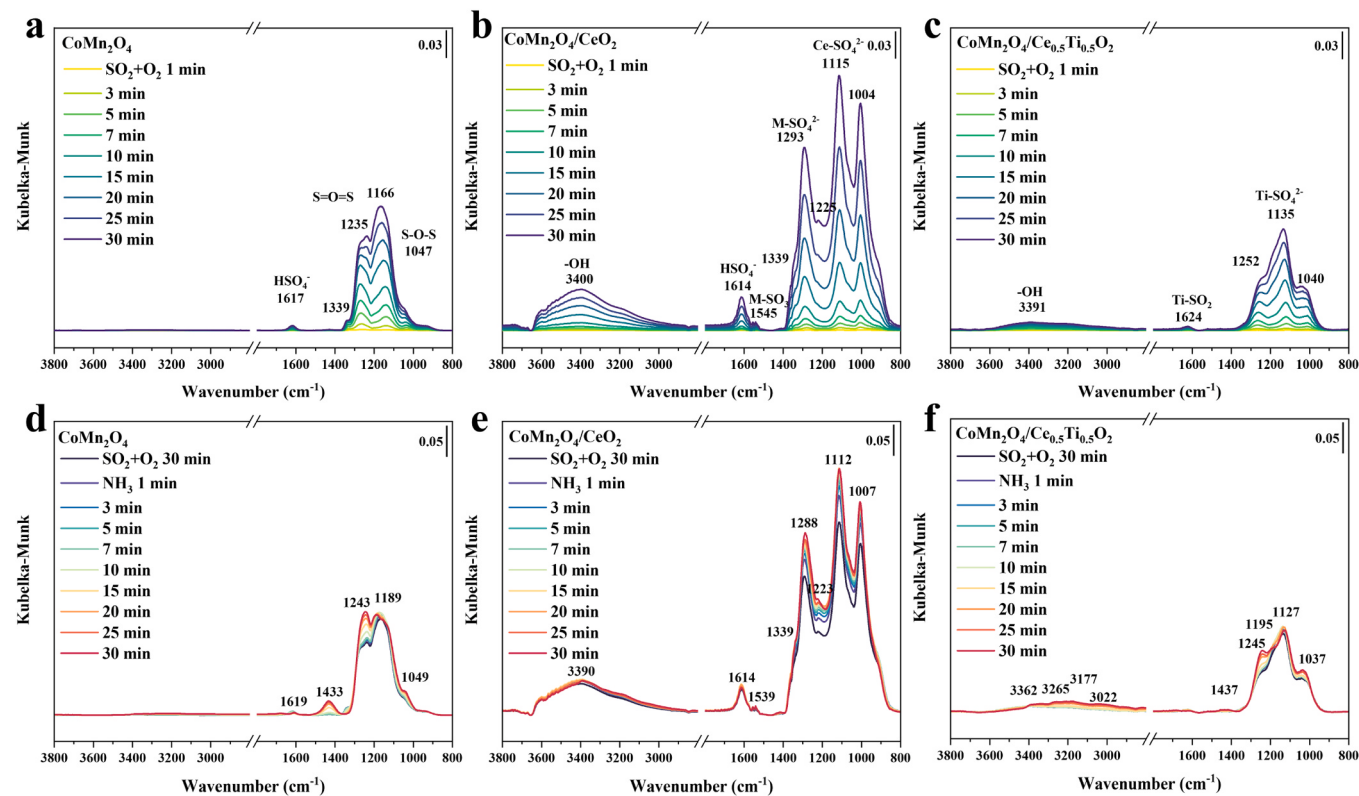


**Fig. 9.** In situ DRIFTS spectra co-adsorption of  $\text{SO}_2+\text{O}_2$  (a)-(c),  $\text{NH}_3$  adsorption after 30 min treatment of  $\text{SO}_2$  (d)-(f) in different time at 150 °C over  $\text{CoMn}_2\text{O}_4$ ,  $\text{CoMn}_2\text{O}_4/\text{CeO}_2$  and  $\text{CoMn}_2\text{O}_4/\text{CeTiO}_x$  catalysts.

two catalysts, in situ DRIFTS were conducted at 150 °C for  $\text{NH}_3$  and then  $\text{SO}_2 + \text{O}_2$  adsorption. As shown in Fig. 10a-c, the bands resulting from part of Lewis  $\text{NH}_3$  adsorption site ( $1541 \text{ cm}^{-1}$ ) and Brønsted acidic sites  $\text{NH}_4^+$  ( $1697 \text{ cm}^{-1}$ ) for species on the  $\text{CoMn}_2\text{O}_4$  catalyst gradually disappeared, and other  $\text{NH}_3$  adsorption peak at  $1206$  and  $1607 \text{ cm}^{-1}$ . And  $\text{NH}_4^+$  species at  $1427 \text{ cm}^{-1}$  does not disappear but gradually intensifies and moves to  $1193$ ,  $1610$  and  $1432 \text{ cm}^{-1}$  respectively with the increasing  $\text{SO}_2$  exposure time, which originates to the accumulation of ammonium sulfate species. As the peaks located at  $1432 \text{ cm}^{-1}$  for  $\text{NH}_4^+$  species may correspond to the newly formed  $\text{NH}_4\text{HSO}_4$  [114]. At the same time, the peaks belonging to the bulk sulfate species ( $1031$ ,  $1153$ , and  $1254 \text{ cm}^{-1}$ ) gradually appear and increase in intensity with prolonged  $\text{SO}_2$  exposure, which is similar to the sulfate species in Fig. 9a [115]. However, the band at  $1257 \text{ cm}^{-1}$  increases greatly at the peak of  $1235 \text{ cm}^{-1}$ , which may associate with the overlaps of different  $\text{SO}_2$  species. The above results suggest that large amounts of surface sulfate species and bulk-like sulfate species form on the surface of the  $\text{CoMn}_2\text{O}_4$  catalyst, which cover the active sites and deactivate the catalyst. The phenomenon that occurs on the surface of  $\text{CoMn}_2\text{O}_4/\text{CeO}_2$  catalyst is quite different (Fig. 10b). With the introduction of  $\text{SO}_2 + \text{O}_2$ , the N-H characteristic peak ( $3057$ ,  $3176$  and  $3335 \text{ cm}^{-1}$ ) related to  $\text{NH}_3$  adsorption do not disappear but gradually increase and  $\text{NH}_4^+$  species belonging to  $\text{NH}_4\text{HSO}_4$  ( $1419 \text{ cm}^{-1}$ ) are also detected, indicating that ammonium sulfate species are accumulating on the catalyst surface. The surface sulfate ( $1607$  and  $1539 \text{ cm}^{-1}$ ) and bulk sulfate species links to Ce ( $1104$ ,  $1012$  and  $1270 \text{ cm}^{-1}$ ) can be observed. It is different from the adsorption of  $\text{SO}_2$  alone in that the bulk sulfate species links to  $\text{CoMn}_2\text{O}_4$  ( $1225$  and  $1339 \text{ cm}^{-1}$ ) do not appear, which indicates that sulfates may preferentially form on Ce sites, and less sulfation of  $\text{CoMn}_2\text{O}_4$  species occurs. It can be deduced that the introduced  $\text{SO}_2$  preferentially binds to  $\text{NH}_3$  and competes for adsorption sites rather than directly adsorbs on the catalyst surface. Compared with the active component  $\text{CoMn}_2\text{O}_4$ ,  $\text{NH}_3$  is preferentially adsorbed on the surface of  $\text{CeO}_2$ , which

corresponds to the results that the introduction of  $\text{CeO}_2$  greatly improves the adsorption capacity of  $\text{NH}_3$ . Similar changes can be observed on the  $\text{CoMn}_2\text{O}_4/\text{CeTiO}_x$  catalysts (Fig. 10c), the proportion of bulk phase sulfate ( $1023$ ,  $1120$ ,  $1247 \text{ cm}^{-1}$ ) is much less than that of the first two types of catalysts, which changes a lot that adsorption peak in Fig. 9c, with the Ce linked sulfate species occupied all, and Ti corresponded species overlapped with Ce ( $1247 \text{ cm}^{-1}$ ), which also indicates that  $\text{NH}_3$  is tend to adsorbed on the Ce. At the same time, the N-H related bands ( $3037$ ,  $3174$ ,  $3256$ , and  $3342 \text{ cm}^{-1}$ ) and  $\text{NH}_4^+$  ( $1428 \text{ cm}^{-1}$ ) increase, which may be attributed to the deposition of ammonium sulfate on surfaces. These results reveal that the deposition rates of sulfate species on the  $\text{CoMn}_2\text{O}_4/\text{CeTiO}_x$  catalysts are much lower than others, which may be attributed to the existence of the  $\text{CeO}_2$  and Ce-Ti parent sulfur affinity sites. It also needs to be illustrated that there is an electron cycle between the multi-metals, that is electrons can transfer from adsorbed  $\text{SO}_2$  to  $\text{Mn}^{4+}$  on the surface of the  $\text{CoMn}_2\text{O}_4$  catalyst, and then  $\text{SO}_2$  is oxidized to  $\text{SO}_3$  and further produces sulfate species. However, electron transfer from  $\text{SO}_2$  to  $\text{Mn}^{4+}$  may be suppressed by electron transfer from  $\text{Ce}^{3+}/\text{Ti}^{3+}$  to  $\text{Mn}^{4+}$ , and consequently, the production of sulfate species is limited on the  $\text{CoMn}_2\text{O}_4/\text{CeTiO}_x$  catalysts.

NO can be adsorbed in a molecular form and oxidized on oxide surfaces, giving rise to surface species such as  $\text{NO}^+$ ,  $\text{NO}_2^-$ ,  $\text{NO}_2$ , and  $\text{NO}_3^-$ , which are identified as key intermediates involved in SCR reactions [116]. Nitrite (HONO), as the most important intermediate species in SCR reaction, is converted by hydrolysis or REDOX reaction of  $\text{NO}_2$  dimer [117,118]. Many studies have found that when  $\text{NO}_2$  and  $\text{SO}_2$  coexist on the surface of metal oxides, the sulfite content is significantly reduced and the sulfate content is significantly increased, which is because the intermediate HONO(or  $\text{N}_2\text{O}_4$ ) oxidizes the sulfite on the surface of the oxide to form sulfate [119,120]. Therefore, the effect of  $\text{SO}_2$  on the oxidation of NO on the catalyst was investigated, and the results are shown in Fig. 10d-f. After exposing  $\text{CoMn}_2\text{O}_4$  to  $\text{NO} + \text{O}_2$  for 30 min at 150 °C, the bands of adsorbed nitrate species appear. After the

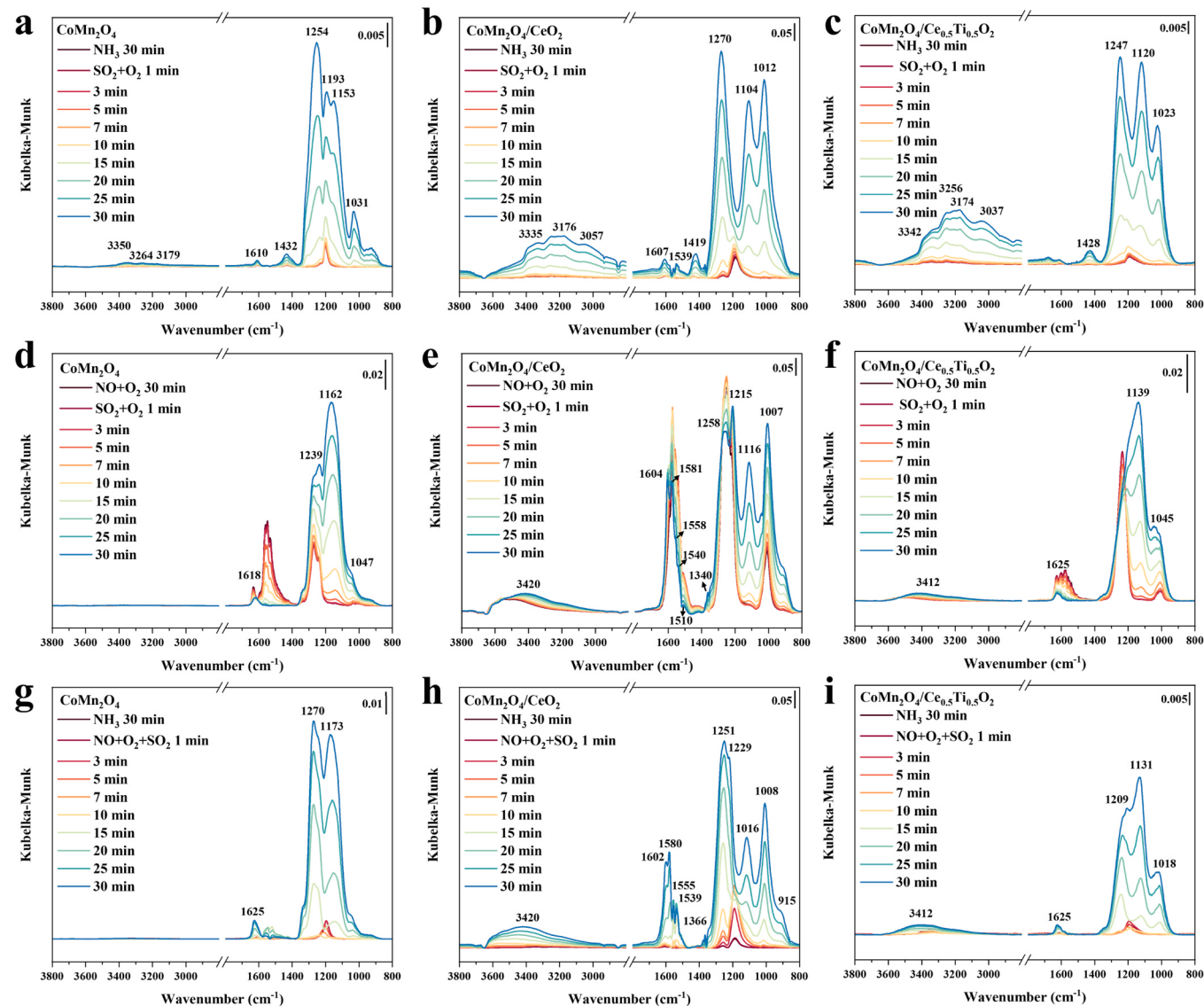


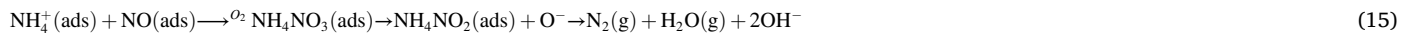
**Fig. 10.** In situ DRIFTS spectra co-adsorption of  $\text{SO}_2+\text{O}_2$  (a)-(c),  $\text{NH}_3$  adsorption after 30 min treatment of  $\text{SO}_2$  (d)-(f) in different time at 150 °C over  $\text{CoMn}_2\text{O}_4$ ,  $\text{CoMn}_2\text{O}_4/\text{CeO}_2$  and  $\text{CoMn}_2\text{O}_4/\text{CeTiO}_x$  catalysts.

introduction of  $\text{SO}_2$ , gaseous  $\text{M-NO}_2$  species ( $1632 \text{ cm}^{-1}$ ), bidentate nitrate ( $1560 \text{ cm}^{-1}$ ), bridging nitrates ( $1240$  and  $1271 \text{ cm}^{-1}$ ) and monodentate nitrate ( $1533$  and  $1548 \text{ cm}^{-1}$ ) rapidly disappear, together with the sulfate species identical to that with the  $\text{SO}_2+\text{O}_2$  adsorption alone appear upon the introduction of  $\text{SO}_2$  and increase with time. It is indicated that there is strong competitive adsorption between  $\text{SO}_2$  and  $\text{NO}$  and have a significant inhibitory effect on the formation of nitrate. For  $\text{CoMn}_2\text{O}_4/\text{CeO}_2$  catalysts, most nitrates are less affected, among which monodentate nitrate ( $1008$ ,  $1510$ ,  $1540$  and  $1558 \text{ cm}^{-1}$ ) decrease gradually but still in the position, the gaseous  $\text{M-NO}_2$  species ( $1604 \text{ cm}^{-1}$ ) and bidentate nitrate ( $1258$  and  $1581 \text{ cm}^{-1}$ ) decrease and move to high wavenumber segment, bridging nitrates ( $1215 \text{ cm}^{-1}$ ) move to low wavenumber segment and increase due to the coincide with the generated sulfate species linked to  $\text{CoMn}_2\text{O}_4$ . Meanwhile, the sulfate species linked to  $\text{Ce}$  ( $1007$  and  $1116 \text{ cm}^{-1}$ ) and  $\text{CoMn}_2\text{O}_4$  ( $1340 \text{ cm}^{-1}$ ) are also detected with increasing time. These results indicate a weak effect of the competitive adsorption of  $\text{NO}$  by  $\text{SO}_2$ , which may originate from the good and stable adsorption performance of the catalyst for  $\text{NO}_x$ , thus the catalyst still retains sufficient adsorbed nitrate species for SCR process despite the reaction with  $\text{SO}_2$ . In contrast, the variation tendency is different on the  $\text{CoMn}_2\text{O}_4/\text{CeTiO}_x$ . After the introduction of

$\text{SO}_2$ , almost all the nitrates are diminished except for gaseous  $\text{M-NO}_2$  species ( $1625 \text{ cm}^{-1}$ ), which is increased combined with the generated  $\text{Ti-SO}_2$ , together with the sulfate species linked to  $\text{Ti}$  ( $1139$  and  $1045 \text{ cm}^{-1}$ ) identical to that with the  $\text{SO}_2+\text{O}_2$  adsorption alone. These results indicate that  $\text{SO}_2$  has a significant inhibiting effect on the formation of nitrate but not including the  $\text{NO}_2$ , thus reducing the effect on “fast-SCR”.

The competitive adsorption of  $\text{SO}_2$  and  $\text{NO}$  on catalysts after the pre-adsorption of  $\text{NH}_3$  was obtained by in situ DRIFTS (Fig. 10g-i). In Fig. 10g, the bands of bridged nitrate ( $1270 \text{ cm}^{-1}$ ), gaseous  $\text{NO}_2$  ( $1625 \text{ cm}^{-1}$ ) and surface sulfate species ( $1173 \text{ cm}^{-1}$ ) were observed for the passage of  $\text{NO} + \text{O}_2 + \text{SO}_2$  after pre-adsorption of  $\text{NH}_3$  by the  $\text{CoMn}_2\text{O}_4$  catalyst. At the same time, the bands of  $\text{NH}_3$  adsorbed species disappeared or decreased, which implies that the reaction path on the  $\text{CoMn}_2\text{O}_4$  catalyst does not change when  $\text{SO}_2$  is present and still follows the L-H mechanism. In contrast, a comparison of the bands of  $\text{NO}_x$  adsorbed species in Fig. 10d reveals that both  $\text{NO}_x$  species and sulfate species can be adsorbed on the surface of the catalyst, but the species and number of adsorbed  $\text{NO}_x$  species are much less. This further confirms that strong competitive adsorption between  $\text{NO}$  and  $\text{SO}_2$  exists, and  $\text{CoMn}_2\text{O}_4$  mainly adsorbs  $\text{SO}_2$  rather than  $\text{NO}$ . Similarly, the

changing trend of CMC is basically the same as that of  $\text{CoMn}_2\text{O}_4$ , with bridged nitrate ( $1229\text{ cm}^{-1}$ ), bidentate nitrate ( $1602$ ,  $1580$ , and  $1251\text{ cm}^{-1}$ ), and monodentate nitrate ( $1555\text{ cm}^{-1}$ ), and surface sulfate species ( $915$ ,  $1008$ ,  $1016$ ,  $1366$ ,  $1539\text{ cm}^{-1}$ ) are also observed (Fig. 10h), which implies that the reaction path on the  $\text{CoMn}_2\text{O}_4/\text{CeO}_2$  catalyst does not change when  $\text{SO}_2$  is present and still follows the L-H mechanism. It can be concluded from Fig. 10e that the competitive adsorption between NO and  $\text{SO}_2$  exists, and the capacity of the two are comparable. Different from the above two catalysts, after introducing  $\text{NO} + \text{O}_2 + \text{SO}_2$ , none of the absorption peaks of nitrate-absorbing species were present over  $\text{CoMn}_2\text{O}_4/\text{CeTiO}_x$  (Fig. 10i). Instead, the bands of Ti-related surface sulfate species ( $1018$ ,  $1131$  and  $1626\text{ cm}^{-1}$ ) and Ce-related surface sulfate species ( $1209\text{ cm}^{-1}$ ) enhanced gradually.

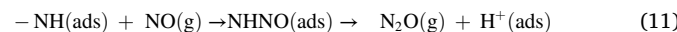
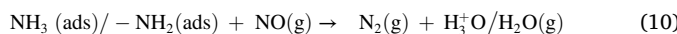
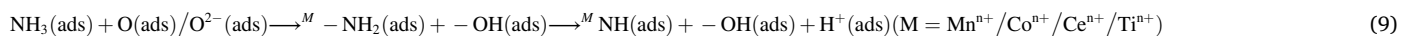


It is worth mentioning that the absorption peak is 80% similarly to the absorption peak of  $\text{SO}_2 + \text{O}_2$  (Fig. 10c), suggesting that NO is almost not adsorbed, and  $\text{SO}_2$  occupies most sites, which has a great impact on the adsorption of  $\text{NO}_x$ .

#### 3.4.4. $\text{NH}_3$ -SCR reaction mechanism and $\text{SO}_2$ effect mechanism

**3.4.4.1. SCR mechanism.** Studies on  $\text{NH}_3$  adsorption on catalysts by in situ DRIFTS show that the strength of the Lewis acid site is higher than the Brønsted acid site. In addition, supported catalysts have stronger acidity in  $\text{NH}_3$ -TPD results, and the metal-carrier co-existence effect provides more acid sites for  $\text{NH}_3$  adsorption, thus producing more  $-\text{NH}_2$  substances. In addition, the structure of  $\text{CeO}_2$  can provide more hydroxyl groups, which can be consumed as Brønsted acid sites by providing hydrogen ( $\text{H}^+$ ) to  $\text{NH}_3$ . It is worth mentioning that amide- $\text{NH}_2$  is an important catalyst intermediate in the low-temperature  $\text{NH}_3$ -SCR process. However, excessive adsorption and oxidation of  $\text{NH}_3$  will lead to the formation of by-product  $\text{N}_2\text{O}$ . The presence of Ti can regulate the adsorption site without loss of catalytic activity, contributing to the formation of metal-support surfaces, thus exposing more active site and accelerating the reaction. The equation of  $\text{NH}_3$  adsorption and activation on the catalyst can be summarized as follows:

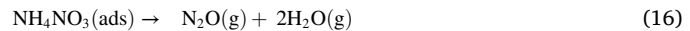
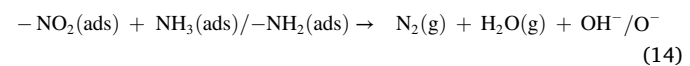
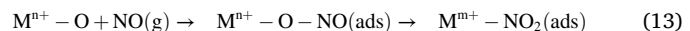
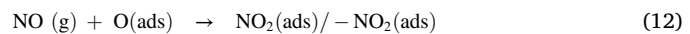
#### 3.4.4.2. Eley-Rideal mechanism



It is worth mentioning that from the adsorption analysis of  $\text{NO} + \text{O}_2$ , in the  $\text{O}_2$  atmosphere, gaseous NO can be adsorbed on the surface of the catalyst to form some nitro and/or nitrate. More  $\text{NO}_2$  species are also generated on the surface of the supported catalyst, which accelerates the "fast SCR" reaction, as shown in Fig. S6. At the active site of the catalyst,

some nitrates may react with gaseous NO to form nitrite. The formation of nitric acid species (bridging nitrate species, monodentate nitrate species and bidentate nitrite species) on the catalyst surface can be described by the following equation.

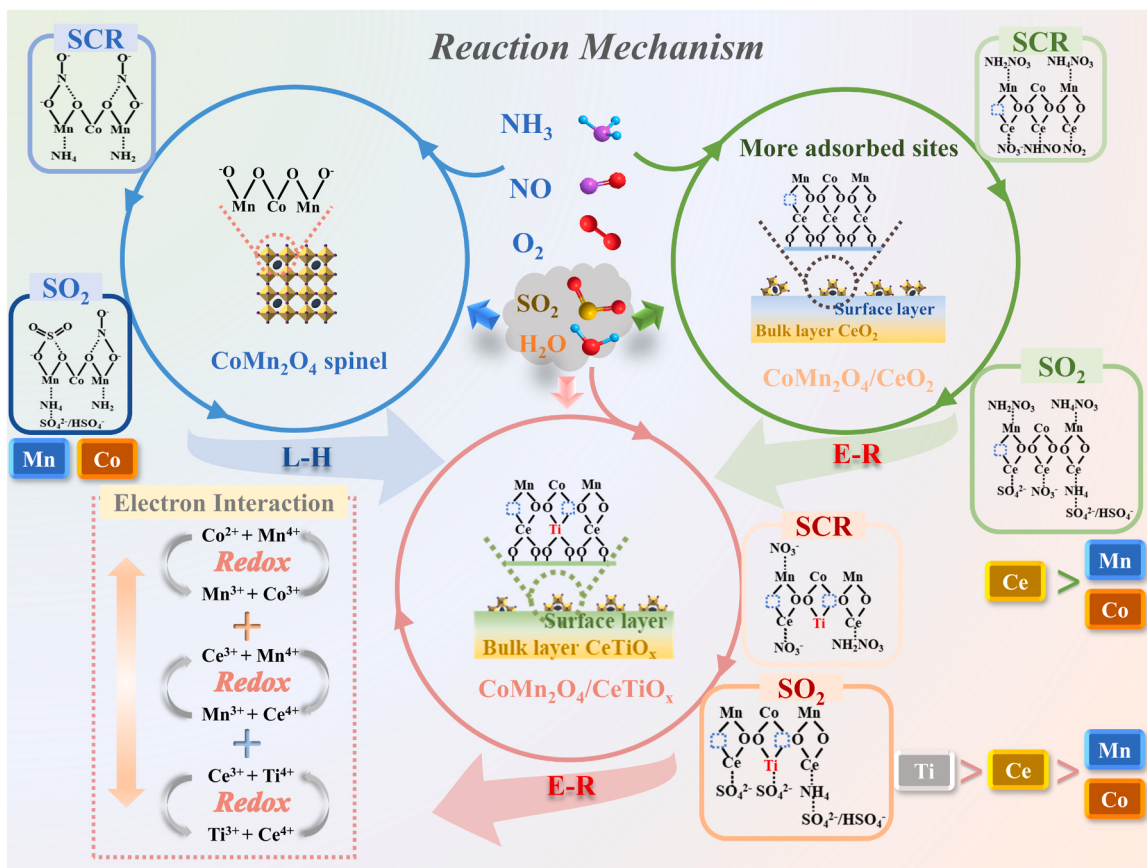
#### 3.4.4.3. Langmuir-Hinshelwood mechanism



Different intermediates and surface adsorption types were detected by in situ DRIFTS experiments and the reaction pathways and mechanisms of catalysts are proposed. For all the catalysts, when  $\text{NO} + \text{O}_2$  are introduced in pre-adsorbed  $\text{NH}_3$ , acid sites such as ad- $\text{NH}_3$ ,  $\text{NH}_4^+$ , and  $-\text{NH}_2$  are gradually consumed, while nitro, monodentate nitrate, bridging nitrate even accompanied with some  $\text{NH}_4\text{NO}_3$  intermediate are formed within few minutes. The Lewis acid site is consumed faster, indicating that plays an important role in low temperatures  $\text{NH}_3$ -SCR reaction. It can be concluded that E-R mechanism exists in all of them. When the gas sequence is changed, the opposite pattern can be found on the  $\text{CoMn}_2\text{O}_4$  catalyst. At the same time, it can be observed that more  $\text{NO}_x$  species are generated when adsorbed  $\text{NH}_3$  is consumed, while not many  $\text{NH}_3$  species are generated when adsorbed  $\text{NO}_x$  is consumed, indicating that the adsorption of  $\text{NO}_x$  is significantly stronger than  $\text{NH}_3$ . Therefore, it can be said that the L-H mechanism is mainly followed on the surface of  $\text{CoMn}_2\text{O}_4$  catalyst. For  $\text{CoMn}_2\text{O}_4/\text{CeO}_2$  catalyst, although the adsorption capacity of  $\text{NO}_x$  is strong, the reaction between adsorbed  $\text{NO}_x$  and  $\text{NH}_3$  does not change significantly after switching the gas entry sequence, indicating that the catalyst mainly follows the E-R mechanism. What needs illustration is that intermediate species associated with the L-H mechanism are observed in both catalysts, that is,  $\text{NO}_2$  and  $\text{NO}_3^-$  react with  $\text{NH}_4^+$  to form intermediates of  $\text{NH}_4\text{NO}_2$  and  $\text{NH}_4\text{NO}_3$ , respectively.  $\text{NH}_4\text{NO}_3$  reacts with adsorbed NO to form  $\text{NO}_2$ ,  $\text{N}_2$  and  $\text{H}_2\text{O}$  at low temperatures or directly decomposes to form  $\text{N}_2\text{O}$  and  $\text{H}_2\text{O}$  at high temperatures, where the formation of  $\text{N}_2\text{O}$  reduces the  $\text{N}_2$  selec-

tivity of the catalyst.

Unlike the previous two catalysts,  $\text{CoMn}_2\text{O}_4/\text{CeTiO}_x$  catalyst do not show a stronger  $\text{NO}_x$  adsorption capacity than  $\text{NH}_3$ , and scarcely intermediate species such as ammonium nitrate appeared in the reaction process, indicating that gaseous NO can react quickly with adsorbed ammonia to produce  $\text{N}_2$  and  $\text{H}_2\text{O}$ , mainly following the E-R mechanism, reducing the path of decomposition to produce  $\text{N}_2\text{O}$ , thus improving the  $\text{N}_2$  selectivity of  $\text{CoMn}_2\text{O}_4/\text{CeTiO}_x$  catalyst. In addition, the multiple active sites of the catalyst can form more  $-\text{NH}_2$  substances, thus accelerating the SCR reaction. This may be due to the weak ability of



**Scheme 2.** Possible SCR pathway and  $\text{SO}_2$  resistance mechanisms of  $\text{CoMn}_2\text{O}_4$ ,  $\text{CoMn}_2\text{O}_4/\text{CeO}_2$  and  $\text{CoMn}_2\text{O}_4/\text{CeTiO}_x$  catalysts.

$\text{CoMn}_2\text{O}_4/\text{CeTiO}_x$  to adsorb  $\text{NO}_x$ , which reduces the reaction path of L-H mechanism.

In summary, both E-R reactions and L-H reactions occur on all catalysts. The first one is dominated by L-H mechanism, while supported two are mainly E-R mechanism with  $\text{CoMn}_2\text{O}_4/\text{CeTiO}_x$  showing a faster reaction rate. In addition, due to the formation of weakly adsorbed  $\text{NO}_2$  on the surface of the supported catalyst, it can be inferred that the “fast SCR” reaction promotes the high catalytic activity of the catalyst.

**3.4.4.4.  $\text{SO}_2$  influence mechanism.** Combining the above characterization and analysis results, the reaction path and anti- $\text{SO}_2$  mechanism of catalysts were compared and explored (Scheme 2). For the  $\text{CoMn}_2\text{O}_4$  catalyst, bidentate nitrate and bridged nitrate react with the  $\text{NH}_3$  adsorbed on Lewis acid sites to produce  $\text{N}_2/\text{N}_2\text{O}$  and  $\text{H}_2\text{O}$ , mainly obeying the L-H mechanism. When  $\text{SO}_2$  is present, strong competition adsorption between  $\text{SO}_2 \rightarrow \text{NH}_3$  and  $\text{SO}_2 \rightarrow \text{NO}$  is shown, which inhibits the adsorption activation of the reaction gas. At the same time, bulk and surface sulfates are formed on the Mn active sites, which hinder the participation of the active center in the redox reaction, leading to a significant decrease in the catalyst activity. The number of acidic sites on the  $\text{CoMn}_2\text{O}_4/\text{CeO}_2$  catalyst are significantly increased, which promote the adsorption of reaction gas  $\text{NO}_x$  and  $\text{NH}_3$ , and enhanced the reaction, which may originate from the abundant adsorption sites that benefited from the good dispersion of active components after the introduction of an acidic  $\text{CeO}_2$  carrier. However, the catalyst also exhibits a stronger adsorption capacity of  $\text{SO}_2$ , thus having a large impact on  $\text{NH}_3$  adsorption and little influence on  $\text{NO}$  adsorption, and weaken the effect on L-H mechanism. Fortunately, the dominated E-R mechanism is less affected by  $\text{SO}_2$ , and the  $\text{CeO}_2$  is inferred as the precedence adsorption sites of  $\text{SO}_2$  according to the bulk and surface sulfate generated in the Ce atoms, which significantly weaken and delay the S intoxication effect of Mn

active components at low temperatures. When the Ti element is doped in the  $\text{CeO}_2$  carrier, the strong REDOX capacity and acidity of the catalyst are regulated, the adsorption capacity of  $\text{NO}$  and  $\text{NH}_3$  is balanced, and the adsorption of  $\text{SO}_2$  is weakened, thus facilitating the  $\text{NH}_3$ -SCR reaction. The above results indicate that the  $\text{CoMn}_2\text{O}_4/\text{CeTiO}_x$  follows the E-R mechanism, the superior anti- $\text{SO}_2$  performance can be attributed to the fact that the  $\text{SO}_2$  can preferentially be adsorbed at the Ti site, followed by the Ce site, and finally the metal Mn or Co site. In other words, the presence of double sacrificial sites can retard active site poisoning to a great extent. Furthermore,  $\text{SO}_2$  has a relatively weak competitive adsorption ability on the  $\text{CoMn}_2\text{O}_4/\text{CeTiO}_x$  catalyst with fewer surface sulfate species generated, meanwhile, the SCR reaction surface follows the E-R mechanism which is less influenced by  $\text{SO}_2$ , the active center is less affected by the sulfate species. Therefore, high catalytic activity can still be maintained in the presence of  $\text{SO}_2$ .

In general, the LT activity and poison resistance of the supported catalyst is better, mainly due to its hierarchical structure, which optimizes the function of each element or component. It works well at the three levels listed below. One is the supporter layer, which serves as the carrier of active components and helps to disperse them maximum. Meanwhile, the Ce-Ti component functions as a double-effect anti-toxic site to absorb  $\text{H}_2\text{O}$  and  $\text{SO}_2$ , which delays the poisoning effect of active site. The second is the active layer, where Co, Mn, and oxygen species acted as adsorbed sites to react with the target gas, which has been continuous at catalytic reaction. The third layer is the cooperative reaction layer, which is created by the contact surface between the support and the active component. In this layer, strong electron interaction and oxygen species migration are produced, which is primarily reflected in the electron transfer between Ce, Ti and Mn, Co ions, which is strongly supportive of the REDOX process.

#### 4. Conclusion

In conclusion, the hierarchically structured Ti-doped  $\text{CeO}_2$  support uniformly dispersed the  $\text{CoMn}_2\text{O}_4$  was synthesized through the combination of hydrothermal and thermal evaporation methods and applied for  $\text{NH}_3\text{-SCR}$  reaction. The as-prepared  $\text{CoMn}_2\text{O}_4/\text{CeTiO}_x$  has shown superior catalytic performance, including excellent L-T activity ( $>95\%$  at  $100\text{--}225^\circ\text{C}$ ), remarkable reaction activation energy ( $28.8 \pm 0.9 \text{ kJ}\cdot\text{mol}^{-1}$ ) and outstanding catalytic stability even in a tough condition (high concentration of  $\text{H}_2\text{O}$  and  $\text{SO}_2$ ). Given the microstructure evolution, the superior performance of  $\text{CoMn}_2\text{O}_4/\text{CeTiO}_x$  is driven by the synergy interface between metal ( $\text{CoMn}_2\text{O}_4$ ) and support ( $\text{CeTiO}_x$ ). On the one hand, Mn-Co oxides coexist on the catalyst, resulting in a high concentration of  $\text{Mn}^{4+}$  and  $\text{Mn}^{3+}$ , at the same time, the high concentration of  $\text{Ce}^{4+}$  in the carrier formed more oxygen vacancies, which enhanced the oxygen migration ability. More effective electronic transfer occurs after the addition of other metal elements (Ti), which is conducive to improving the ability of oxidation and reducing and generating a more efficient activity center. On the other hand, the increase in surface acidity sites leads to an enhancement of  $\text{NH}_3/\text{NO}$  adsorption ability, and the Ti doping adjusted the surface acidity, by weakening the per-oxidation of  $\text{NH}_3$  and  $\text{NO}$  adsorption species, thus inhibiting the generation of  $\text{N}_2\text{O}$  and improving the selectivity of  $\text{N}_2$ . One of the most important points related to stability is the existence of dual anti-poison sites (Ce, Ti), that the  $\text{CeTiO}_x$  carrier accelerated the transfer of toxic sites and delayed the poisoning on active components (Mn, Co).

Taking account of the reaction process, the  $\text{CoMn}_2\text{O}_4$  catalyst mainly obeys the L-H mechanism by bidentate nitrate and bridged nitrate reacts with the  $\text{NH}_3$  adsorbed on Lewis acid sites to produce  $\text{N}_2/\text{N}_2\text{O}$  and  $\text{H}_2\text{O}$ , the  $\text{SO}_2$  inhibits the reaction by strong competition adsorption with  $\text{NO}$  and  $\text{NH}_3$ , and accumulates of bulk and surface sulfate. Discriminatively, the two supported catalysts are dominated by E-R mechanism. The  $\text{CoMn}_2\text{O}_4/\text{CeO}_2$  performed outstanding adsorption ability to all of gas composition (including  $\text{SO}_2$ ), and  $\text{SO}_2$  exhibits a large impact on  $\text{NH}_3$  adsorption but little influence on  $\text{NO}$ , which weakens the effect on L-H mechanism. Fortunately, the dominated E-R mechanism is less affected by  $\text{SO}_2$ , and the poisoned sites are migrated to Ce from Mn, Co. When the Ti element is doped in the  $\text{CeO}_2$  carrier, the strong REDOX capacity, acidity, and adsorption capacity to gas composition are balanced. The superior anti- $\text{SO}_2$  performance can be attributed to the  $\text{SO}_2$  adsorption order of the sites ( $\text{Ti} > \text{Ce} > \text{Co} > \text{Mn}$ ), which retards the active center affected by the sulfate species. In general, studies regarding low-temperature denitrification catalysts can be conducted in accordance with the novel concept of double cycle + coupling, which is based on the powerful synergistic consequence of metal active components and holders. Granting full access to the redox cycle of the active sites and modifying the adsorption equilibrium cycle of sulfur-resistant sites on the reactive components through the modulation of the microstructure or the exterior acidity, etc., aiming to boost efficiency of low-temperature catalytic activity and stability. The results obtained add to our understanding of how  $\text{SO}_2$  and  $\text{H}_2\text{O}$  react with various metal elements during the  $\text{NH}_3\text{-SCR}$  catalysis and offer theoretical direction for creating stable low-temperature de $\text{NO}_x$  catalysts.

#### CRediT authorship contribution statement

**Ning Luo:** Conceptualization, Methodology, Validation, Formal analysis, Writing – original draft, Visualization, Writing – review & editing. **Fengyu Gao:** Conceptualization, Formal analysis, Writing – review & editing, Project administration, Funding acquisition. **Hengheng Liu:** Investigation, Formal analysis. **Tingkai Xiong:** Data curation, Formal analysis. **Jiajun Wen:** Investigation, Data curation. **Erhong Duan:** Resources, Funding acquisition. **Chengzhi Wang:** Writing – review & editing, Providing language help. **Shunzheng Zhao:** Formal analysis. **Honghong Yi:** Resources, Supervision. **Xiaolong Tang:** Resources, Project administration, Funding acquisition.

#### Declaration of Competing Interest

The authors declare that they have no known competing financial interests or personal relationships that could have appeared to influence the work reported in this paper.

#### Data availability

The authors do not have permission to share data.

#### Acknowledgments

This research was supported by the National Natural Science Foundation of China (U20A20130), and Fundamental Research Funds for the Central Universities (FRF-EY17-23-07). The authors wish to thank the facility's support of the 4B9A beamline of the Beijing Synchrotron Radiation Facility (BSRF).

#### Appendix A. Supporting information

Supplementary data associated with this article can be found in the online version at [doi:10.1016/j.apcatb.2023.123442](https://doi.org/10.1016/j.apcatb.2023.123442).

#### References

- [1] R. Bai, J.C.K. Lam, V.O.K. Li, A review on health cost accounting of air pollution in China, *Environ. Int.* 120 (2018) 279–294.
- [2] J. Huang, X. Pan, X. Guo, G. Li, Impacts of air pollution wave on years of life lost: a crucial way to communicate the health risks of air pollution to the public, *Environ. Int.* 113 (2018) 42–49.
- [3] F. Chen, Z. Chen, Cost of economic growth: air pollution and health expenditure, *Sci. Total Environ.* 755 (2021), 142543.
- [4] G. Shaddick, M.L. Thomas, P. Mudu, G. Ruggeri, S. Gumy, Half the world's population are exposed to increasing air pollution, *npj Climate and Atmospheric Science* 3 (2020) 23.
- [5] S. Fu, Z. Ma, B.J. Ni, J. Peng, L. Zhang, Q. Fu, Research on the spatial differences of pollution-intensive industry transfer under the environmental regulation in China, *Ecol. Indic.* 129 (2021), 107921.
- [6] G. Zhang, W. Liu, H. Duan, Environmental regulation policies, local government enforcement and pollution-intensive industry transfer in China, *Comput. Ind. Eng.* 148 (2020), 106748.
- [7] C. Paolucci, I. Khurana, A.A. Parekh, S. Li, A.J. Shih, H. Li, J.R. Di Iorio, J. D. Albarracín-Caballero, A. Yezerski, J.T. Miller, W.N. Delgass, F.H. Ribeiro, W. F. Schneider, R. Gounder, Dynamic multinuclear sites formed by mobilized copper ions in  $\text{NO}_x$  selective catalytic reduction, *Science* 357 (2017) 898–903.
- [8] J.L. Laughner, R.C. Cohen, Direct observation of changing  $\text{NO}_x$  lifetime in North American cities, *Science* 366 (2019) 723–727.
- [9] L. Han, S. Cai, M. Gao, Jy Hasegawa, P. Wang, J. Zhang, L. Shi, D. Zhang, Selective catalytic reduction of  $\text{NO}_x$  with  $\text{NH}_3$  by using novel catalysts: state of the art and future prospects, *Chem. Rev.* 119 (2019) 10916–10976.
- [10] K. Guo, J. Ji, W. Song, J. Sun, C. Tang, L. Dong, Conquering ammonium bisulfate poison over low-temperature  $\text{NH}_3\text{-SCR}$  catalysts: a critical review, *Appl. Catal. B Environ.* 297 (2021), 120388.
- [11] X. Zhou, P. Wang, Z. Shen, S. Chen, Q. Wang, D. Cheng, D. Zhang, Low-temperature  $\text{NO}_x$  reduction over hydrothermally stable SCR catalysts by engineering low-coordinated Mn active sites, *Chem. Eng. J.* 442 (2022), 136182.
- [12] F. Gao, X. Tang, H. Yi, J. Li, S. Zhao, J. Wang, C. Chu, C. Li, Promotional mechanisms of activity and  $\text{SO}_2$  tolerance of Co- or Ni-doped  $\text{MnO}_x\text{-CeO}_2$  catalysts for SCR of  $\text{NO}_x$  with  $\text{NH}_3$  at low temperature, *Chem. Eng. J.* 317 (2017) 20–31.
- [13] L. Zhang, L. Li, Y. Cao, X. Yao, C. Ge, F. Gao, Y. Deng, C. Tang, L. Dong, Getting insight into the influence of  $\text{SO}_2$  on  $\text{TiO}_2/\text{CeO}_2$  for the selective catalytic reduction of NO by  $\text{NH}_3$ , *Appl. Catal. B Environ.* 165 (2015) 589–598.
- [14] S. Ali, L. Chen, Z. Li, T. Zhang, R. Li, Su.H. Bakhtiar, X. Leng, F. Yuan, X. Niu, Y. Zhu,  $\text{Cu}_x\text{-Nb}_{1.1-x}$  ( $x = 0.45, 0.35, 0.25, 0.15$ ) bimetal oxides catalysts for the low temperature selective catalytic reduction of NO with  $\text{NH}_3$ , *Appl. Catal. B Environ.* 236 (2018) 25–35.
- [15] Y. Li, Y. Wan, Y. Li, S. Zhan, Q. Guan, Y. Tian, Low-temperature selective catalytic reduction of NO with  $\text{NH}_3$  over  $\text{Mn}_2\text{O}_3$ -doped  $\text{Fe}_2\text{O}_3$  hexagonal microsheets, *ACS Appl. Mater. Interfaces* 8 (2016) 5224–5233.
- [16] F. Gao, S. Ni, Z. Niu, X. Tang, H. Yi, C. Wang, Enhancement strategies for SCR activity,  $\text{H}_2\text{O}$  &  $\text{SO}_2$  resistances and  $\text{N}_2$  selectivity on upgraded  $\text{HMnO}_x/\text{Co}/\text{MnCeO}_x/\text{NF}$  catalysts, *J. Environ. Chem. Eng.* 9 (2021), 106190.
- [17] X. Tang, C. Wang, F. Gao, R. Zhang, Y. Shi, H. Yi, Acid modification enhances selective catalytic reduction activity and sulfur dioxide resistance of manganese-cerium-cobalt catalysts: Insight into the role of phosphotungstic acid, *J. Colloid Interface Sci.* 603 (2021) 291–306.

[18] X. Tang, C. Wang, F. Gao, Y. Ma, H. Yi, S. Zhao, Y. Zhou, Effect of hierarchical element doping on the low-temperature activity of manganese-based catalysts for NH<sub>3</sub>-SCR, *J. Environ. Chem. Eng.* 8 (2020), 104399.

[19] J.W. Shi, G. Gao, Z. Fan, C. Gao, B. Wang, Y. Wang, Z. Li, C. He, C. Niu, Ni<sub>y</sub>Co<sub>1-y</sub>Mn<sub>2</sub>O<sub>x</sub> microspheres for the selective catalytic reduction of NO<sub>x</sub> with NH<sub>3</sub>: the synergetic effects between Ni and Co for improving low-temperature catalytic performance, *Appl. Catal. A Gen.* 560 (2018) 1–11.

[20] Q. Zhao, Z. Yan, C. Chen, J. Chen, Spinel: controlled preparation, oxygen reduction/evolution reaction application, and beyond, *Chem. Rev.* 117 (2017) 10121–10211.

[21] F. Gao, X. Tang, H. Yi, S. Zhao, W. Zhu, Y. Shi, Mn<sub>2</sub>NiO<sub>4</sub> spinel catalyst for high-efficiency selective catalytic reduction of nitrogen oxides with good resistance to H<sub>2</sub>O and SO<sub>2</sub> at low temperature, *J. Environ. Sci.* 89 (2020) 145–155.

[22] Y. Shi, H. Yi, F. Gao, S. Zhao, Z. Xie, X. Tang, Evolution mechanism of transition metal in NH<sub>3</sub>-SCR reaction over Mn-based bimetallic oxide catalysts: structure-activity relationships, *J. Hazard. Mater.* 413 (2021), 125361.

[23] X. Wang, Z. Lan, K. Zhang, J. Chen, L. Jiang, R. Wang, Structure-activity relationships of AMn<sub>2</sub>O<sub>4</sub> (A = Cu and Co) spinels in selective catalytic reduction of NO<sub>x</sub>: experimental and theoretical study, *J. Phys. Chem. C* 121 (2017) 3339–3349.

[24] F. Gao, C. Chu, W. Zhu, X. Tang, H. Yi, R. Zhang, High-efficiency catalytic oxidation of nitric oxide over spherical MnCo spinel catalyst at low temperature, *Appl. Surf. Sci.* 479 (2019) 548–556.

[25] Y. Shi, X. Tang, H. Yi, F. Gao, S. Zhao, J. Wang, K. Yang, R. Zhang, Controlled synthesis of spinel-type mesoporous Mn-Co rods for SCR of NO<sub>x</sub> with NH<sub>3</sub> at low temperature, *Ind. Eng. Chem. Res.* 58 (2019).

[26] C. Yang, X. Tang, H. Yi, F. Gao, S. Zhao, R. Zhang, W. Zhu, Comparison of selective catalytic reduction performance of Mn-Co Bi-metal oxides prepared by different methods, *ChemistrySelect* 5 (2020) 9409–9416.

[27] F. Gao, X. Tang, H. Yi, S. Zhao, J. Wang, Y. Shi, X. Meng, Novel Co- or Ni-Mn binary oxide catalysts with hydroxyl groups for NH<sub>3</sub>-SCR of NO<sub>x</sub> at low temperature, *Appl. Surf. Sci.* 443 (2018) 103–113.

[28] W. Chen, R. Zou, X. Wang, Toward an atomic-level understanding of the catalytic mechanism of selective catalytic reduction of NO<sub>x</sub> with NH<sub>3</sub>, *ACS Catal.* 12 (2022) 14347–14375.

[29] F. Gao, X. Tang, H. Yi, S. Zhao, C. Li, J. Li, Y. Shi, X. Meng, A review on selective catalytic reduction of NO<sub>x</sub> by NH<sub>3</sub> over Mn-based catalysts at low temperatures: catalysts, mechanisms, kinetics and DFT calculations, *Catalysts* 7 (2017) 199.

[30] W. Hu, J. He, X. Liu, H. Yu, X. Jia, T. Yan, L. Han, D. Zhang, SO<sub>2</sub>- and H<sub>2</sub>O-tolerant catalytic reduction of NO<sub>x</sub> at a low temperature via engineering polymeric VO<sub>x</sub> species by CeO<sub>2</sub>, *Environ. Sci. Technol.* 56 (2022) 5170–5178.

[31] X. Liu, P. Wang, Y. Shen, L. Zheng, L. Han, J. Deng, J. Zhang, A. Wang, W. Ren, F. Gao, D. Zhang, Boosting SO<sub>2</sub>-resistant NO<sub>x</sub> reduction by modulating electronic interaction of short-range Fe–O coordination over Fe<sub>2</sub>O<sub>3</sub>/TiO<sub>2</sub> catalysts, *Environ. Sci. Technol.* 56 (2022) 11646–11656.

[32] Z. Si, Y. Shen, J. He, T. Yan, J. Zhang, J. Deng, D. Zhang, SO<sub>2</sub>-induced alkali resistance of FeVO<sub>4</sub>/TiO<sub>2</sub> catalysts for NO<sub>x</sub> reduction, *Environ. Sci. Technol.* 56 (2022) 605–613.

[33] X. Liu, P. Wang, Y. Shen, S. Bi, W. Ren, D. Zhang, Boosting SO<sub>2</sub>-tolerant catalytic reduction of NO<sub>x</sub> via selective adsorption and activation of reactants over Ce<sup>4+</sup>-SO<sub>4</sub><sup>2-</sup> pair sites, *ACS Catal.* 12 (2022) 11306–11317.

[34] Z. Zhang, R. Li, M. Wang, Y. Li, Y. Tong, P. Yang, Y. Zhu, Two steps synthesis of CeTiO<sub>x</sub> oxides nanotube catalyst: Enhanced activity, resistance of SO<sub>2</sub> and H<sub>2</sub>O for low temperature NH<sub>3</sub>-SCR of NO<sub>x</sub>, *Appl. Catal. B Environ.* 282 (2021), 119542.

[35] X. Li, Z. Wang, J. Sun, R. Oh, J. Feng, D. Shi, W. Zhao, S. Liu, Influence of CeO<sub>2</sub> morphology on WO<sub>3</sub>/CeO<sub>2</sub> catalyzed NO selective catalytic reduction by NH<sub>3</sub>, *J. Energy Inst.* 93 (2020) 1511–1518.

[36] X. Wu, X. Yu, Z. Huang, H. Shen, G. Jing, MnO<sub>x</sub>-decorated VO<sub>x</sub>/CeO<sub>2</sub> catalysts with preferentially exposed {110} facets for selective catalytic reduction of NO<sub>x</sub> by NH<sub>3</sub>, *Appl. Catal. B Environ.* 268 (2020), 118419.

[37] B. Shen, Y. Wang, F. Wang, T. Liu, The effect of Ce-Zr on NH<sub>3</sub>-SCR activity over MnO<sub>x(0.6)</sub>/Ce<sub>0.5</sub>Zr<sub>0.5</sub>O<sub>2</sub> at low temperature, *Chem. Eng. J.* 236 (2014) 171–180.

[38] B. Liu, J. Liu, L. Xin, T. Zhang, Y. Xu, F. Jiang, X. Liu, Unraveling reactivity descriptors and structure sensitivity in low-temperature NH<sub>3</sub>-SCR reaction over CeTiO<sub>x</sub> catalysts: a combined computational and experimental study, *ACS Catal.* 11 (2021) 7613–7636.

[39] X. Zhao, S. Ma, Z. Li, F. Yuan, X. Niu, Y. Zhu, Synthesis of Ce<sub>n</sub>TiO<sub>x</sub> flakes with hierarchical structure and its enhanced activity for selective catalytic reduction of NO<sub>x</sub> with NH<sub>3</sub>, *Chem. Eng. J.* 392 (2020), 123801.

[40] S. Zhao, H. Ding, J. Chen, C. Yang, X. Xian, Facile synthesis of CNTs@TiO<sub>2</sub> composites by solvothermal reaction for high-rate and long-life lithium-ion batteries, *J. Phys. Chem. Solids* 152 (2021), 109950.

[41] N.L.N. Broge, F. Søndergaard-Pedersen, M. Roelsgaard, X. Hassing-Hansen, B. B. Iversen, Mapping the redox chemistry of common solvents in solvothermal synthesis through *in situ* X-ray diffraction, *Nanoscale* 12 (2020) 8511–8518.

[42] W. Liu, G. Zhao, M. An, L. Chang, Solvothermal synthesis of nanostructured BiVO<sub>4</sub> with highly exposed (010) facets and enhanced sunlight-driven photocatalytic properties, *Appl. Surf. Sci.* 357 (2015) 1053–1063.

[43] Y. Zhang, X. Zhou, Z. Liu, Q. Liu, G. Zhu, K. Dai, B. Li, B. Sun, Z. Jin, X. Li, Green synthesis of monodispersed LaCO<sub>3</sub>OH microgears with novel plum blossom-like structure via a glycerol-mediated solvothermal method, *RSC Adv.* 5 (2015) 21925–21930.

[44] K. Zheng, Y. Li, B. Liu, F. Jiang, Y. Xu, X. Liu, Ti-doped CeO<sub>2</sub> stabilized single-atom rhodium catalyst for selective and stable CO<sub>2</sub> hydrogenation to ethanol, *Angew. Chem. Int. Ed.* 61 (2022), e202210991.

[45] T. Zhang, Y. Zhang, P. Ning, H. Wang, Y. Ma, S. Xu, M. Liu, Q. Zhang, F. Xia, The property tuning of NH<sub>3</sub>-SCR over iron-tungsten catalyst: role of calcination temperature on surface defect and acidity, *Appl. Surf. Sci.* 538 (2021), 147999.

[46] K. Guo, J. Ji, R. Osuga, Y. Zhu, J. Sun, C. Tang, J.N. Kondo, L. Dong, Construction of Fe<sub>2</sub>O<sub>3</sub> loaded and mesopore confined thin-layer titania catalyst for efficient NH<sub>3</sub>-SCR of NO<sub>x</sub> with enhanced H<sub>2</sub>O/SO<sub>2</sub> tolerance, *Appl. Catal. B Environ.* 287 (2021), 119982.

[47] Y. Liu, F. Gao, S. Ko, C. Wang, H. Liu, X. Tang, H. Yi, Y. Zhou, Superior catalytic performance within H<sub>2</sub>O-vapor of W-modified CoMn<sub>2</sub>O<sub>4</sub>/TiO<sub>2</sub> catalyst for selective catalytic reduction of NO<sub>x</sub> with NH<sub>3</sub>, *Chem. Eng. J.* 434 (2022), 134770.

[48] B. Zhao, W. Chen, Y. Tan, F. Li, M. Tian, Preparation of M/Ce<sub>1-x</sub>Ti<sub>x</sub>O<sub>2</sub> (M=Pt, Rh, Ru) from sol-gel method and their catalytic oxidation activity for diesel soot, *J. Rare Earths* 40 (2022) 1849–1859.

[49] J. Kennedy, M. Elayaperumal, M. Henini, M. Maaza, Photodegradation of organic pollutants RhB dye using UV simulated sunlight on ceria based TiO<sub>2</sub> nanomaterials for antibacterial applications, *Sci. Rep.* 6 (2016) 38064.

[50] F. Lu, B. Jiang, J. Wang, Z. Huang, Z. Liao, Y. Yang, J. Zheng, Promotional effect of Ti doping on the ketonization of acetic acid over a CeO<sub>2</sub> catalyst, *RSC Adv.* 7 (2017) 22017–22026.

[51] F. Fang, J. Kennedy, E. Manikandan, J. Futter, A. Markwitz, Morphology and characterization of TiO<sub>2</sub> nanoparticles synthesized by arc discharge, *Chem. Phys. Lett.* 521 (2012) 86–90.

[52] X. Lu, X. Li, F. Chen, Z. Chen, J. Qian, Q. Zhang, Biotemplating synthesis of N-doped two-dimensional CeO<sub>2</sub>-TiO<sub>2</sub> nanosheets with enhanced visible light photocatalytic desulfurization performance, *J. Alloy. Compd.* 815 (2020), 152326.

[53] Y. Shi, X. Tang, H. Yi, F. Gao, S. Zhao, J. Wang, K. Yang, R. Zhang, Controlled synthesis of spinel-type mesoporous Mn-Co rods for SCR of NO<sub>x</sub> with NH<sub>3</sub> at low temperature, *Ind. Eng. Chem. Res.* 58 (2019) 3606–3617.

[54] P. Gao, Y. Zeng, P. Tang, Z. Wang, J. Yang, A. Hu, J. Liu, Understanding the synergistic effects and structural evolution of Co(OH)<sub>2</sub> and Co<sub>3</sub>O<sub>4</sub> toward boosting electrochemical charge storage, *Adv. Funct. Mater.* 32 (2022), 2108644.

[55] D. Yan, R. Chen, Z. Xiao, S. Wang, Engineering the electronic structure of Co<sub>3</sub>O<sub>4</sub> by carbon-doping for efficient overall water splitting, *Electrochim. Acta* 303 (2019) 316–322.

[56] Y. Li, Y. Yang, X. Shu, D. Wan, N. Wei, X. Yu, M.B.H. Breese, T. Venkatesan, J. M. Xue, Y. Liu, S. Li, T. Wu, J. Chen, From titanium sesquioxide to titanium dioxide: oxidation-induced structural, phase, and property evolution, *Chem. Mater.* 30 (2018) 4383–4392.

[57] M. Sridharan, T. Maiyalagan, G. Panomsuwan, R. Techapiesancharoenkij, Enhanced electrocatalytic activity of cobalt-doped ceria embedded on nitrogen, sulfur-doped reduced graphene oxide as an electrocatalyst for oxygen reduction reaction, *Catalysts* 12 (2022) 6.

[58] M. Wagner, B. Meyer, M. Setvin, M. Schmid, U. Diebold, Direct assessment of the acidity of individual surface hydroxyls, *Nature* 592 (2021) 722–725.

[59] S. Jayasubramanian, S. Balasundari, P.A. Rayjada, R.A. Kumar, N. Satyanarayana, P. Muralidharan, Enhanced electrochemical performance of MnCo<sub>2</sub>O<sub>4</sub> nanorods synthesized via microwave hydrothermal method for supercapacitor applications, *J. Mater. Sci. Mater. Electron.* 29 (2018) 21194–21204.

[60] K.M. Racik, K. Guruprasad, M. Mani, M. Joseph, T. Maiyalagan, V. Antony Raj, Enhanced electrochemical performance of MnO<sub>2</sub>/NiO nanocomposite for supercapacitor electrode with excellent cycling stability, *J. Mater. Sci. Mater. Electron.* 30 (2019).

[61] B. Jain, A.K. Singh, A. Hashmi, M.A.B.H. Susan, J.P. Lellouche, Surfactant-assisted cerium oxide and its catalytic activity towards Fenton process for non-degradable dye, *Adv. Compos. Hybrid. Mater.* 3 (2020) 430–441.

[62] L. Chen, B.Y. He, S. He, T.J. Wang, C.L. Su, Y. Jin, Fe-Ti oxide nano-adsorbent synthesized by co-precipitation for fluoride removal from drinking water and its adsorption mechanism, *Powder Technol.* 227 (2012) 3–8.

[63] C.X. Gao, Q.F. Liu, D.S. Xue, Preparation and characterization of amorphous  $\beta$ -FeOOH nanowire arrays, *J. Mater. Sci. Lett.* 21 (2002) 1781–1783.

[64] B. Yan, H. Zhu, Controlled synthesis of CeO<sub>2</sub> nanoparticles using novel amphiphilic cerium complex precursors, *J. Nanopart. Res.* 10 (2008) 1279–1285.

[65] Y. Guo, S. Mei, K. Yuan, D.J. Wang, H.C. Liu, C.H. Yan, Y.W. Zhang, Low-temperature CO<sub>2</sub> methanation over CeO<sub>2</sub>-supported Ru single atoms, nanoclusters, and nanoparticles competitively tuned by strong metal-support interactions and H-spillover effect, *ACS Catal.* 8 (2018) 6203–6215.

[66] T.W. van Deelen, C. Hernández Mejía, K.P. de Jong, Control of metal-support interactions in heterogeneous catalysts to enhance activity and selectivity, *Nat. Catal.* 2 (2019) 955–970.

[67] W. Chandane, S. Gajare, R. Kagne, M. Kukade, A. Pawar, G. Rashinkar, B. Tamhankar, Sulfated tin oxide (SO<sub>4</sub><sup>2-</sup>/SnO<sub>2</sub>): an efficient heterogeneous solid superacid catalyst for the facile synthesis of 2,3-dihydroquinolin-4(1H)-ones, *Res. Chem. Intermed.* 48 (2022) 1439–1456.

[68] Z. Liu, F. Yu, K. Pan, X. Zhou, R. Sun, J. Tian, Y. Wan, J. Dan, B. Dai, Two-dimensional vermiculite carried CuCoCe catalysts for CO-SCR in the presence of O<sub>2</sub> and H<sub>2</sub>O: experimental and DFT calculation, *Chem. Eng. J.* 422 (2021), 130099.

[69] K.A. Moltved, K.P. Kepp, The chemical bond between transition metals and oxygen: electronegativity, d-orbital effects, and oxophilicity as descriptors of metal-oxygen interactions, *J. Phys. Chem. C* 123 (2019) 18432–18444.

[70] Y. Wang, C. Wöll, IR spectroscopic investigations of chemical and photochemical reactions on metal oxides: bridging the materials gap, *Chem. Soc. Rev.* 46 (2017) 1875–1932.

[71] Z. Wang, J. Liu, Y. Yang, Y. Yu, X. Yan, Z. Zhang, Regenerable  $\text{Co}_x\text{Mn}_{3-x}\text{O}_4$  spinel sorbents for elemental mercury removal from syngas: experimental and DFT studies, *Fuel* 266 (2020), 117105.

[72] Y. Gao, D.R. Kong, Z.Y. Zhang, X.F. Zhang, Z.P. Deng, L.H. Huo, S. Gao, Spinel  $\text{CoMn}_2\text{O}_4$  hollow nanospheres for very wide linear and sensitive detection of hydrogen peroxide, *J. Alloy. Compd.* 897 (2022), 163158.

[73] C. Ruan, Z.Q. Huang, J. Lin, L. Li, X. Liu, M. Tian, C. Huang, C.R. Chang, J. Li, X. Wang, Synergy of the catalytic activation on Ni and the  $\text{CeO}_2\text{-TiO}_2/\text{Ce}_2\text{Ti}_2\text{O}_7$  stoichiometric redox cycle for dramatically enhanced solar fuel production, *Energy Environ. Sci.* 12 (2019) 767–779.

[74] H. Wang, X.K. Gu, X. Zheng, H. Pan, J. Zhu, S. Chen, L. Cao, W.-X. Li, J. Lu, Disentangling the size-dependent geometric and electronic effects of palladium nanocatalysts beyond selectivity, *Sci. Adv.* 5 (2019), eaat6413.

[75] S. Mo, Q. Zhang, J. Li, Y. Sun, Q. Ren, S. Zou, Q. Zhang, J. Lu, M. Fu, D. Mo, J. Wu, H. Huang, D. Ye, Highly efficient mesoporous  $\text{MnO}_2$  catalysts for the total toluene oxidation: oxygen-vacancy defect engineering and involved intermediates using *in situ* DRIFTS, *Appl. Catal. B Environ.* 264 (2020), 118464.

[76] C. Wang, F. Gao, S. Ko, H. Liu, H. Yi, X. Tang, Structural control for inhibiting  $\text{SO}_2$  adsorption in porous  $\text{MnCe}$  nanowire aerogel catalysts for low-temperature  $\text{NH}_3$ -SCR, *Chem. Eng. J.* 434 (2022), 134729.

[77] L. Miao, X. Tang, S. Zhao, X. Xie, C. Du, T. Tang, H. Yi, Study on mechanism of low-temperature oxidation of n-hexanal catalysed by 2D ultrathin  $\text{Co}_3\text{O}_4$  nanosheets, *Nano Res.* 15 (2022) 1660–1671.

[78] A. Mumtaz, N.M. Mohamed, M. Mazhar, M.A. Ehsan, M.S. Mohamed Saheed, Core-shell vanadium modified titania@ $\beta$ - $\text{In}_2\text{S}_3$  hybrid nanorod arrays for superior interface stability and photochemical activity, *ACS Appl. Mater. Interfaces* 8 (2016) 9037–9049.

[79] G. Ou, Y. Xu, B. Wen, R. Lin, B. Ge, Y. Tang, Y. Liang, C. Yang, K. Huang, D. Zu, R. Yu, W. Chen, J. Li, H. Wu, L.-M. Liu, Y. Li, Tuning defects in oxides at room temperature by lithium reduction, *Nat. Commun.* 9 (2018) 1302.

[80] W. Hu, Y. Liu, R.L. Withers, T.J. Frankcombe, L. Norén, A. Snashall, M. Kitchin, P. Smith, B. Gong, H. Chen, J. Schieler, F. Brink, J. Wong-Leung, Electron-pinned defect-dipoles for high-performance colossal permittivity materials, *Nat. Mater.* 12 (2013) 821–826.

[81] D.N. Mueller, M.L. Machala, H. Bluhm, W.C. Chueh, Redox activity of surface oxygen anions in oxygen-deficient perovskite oxides during electrochemical reactions, *Nat. Commun.* 6 (2015) 6097.

[82] A. Nenning, A.K. Opitz, C. Rameshan, R. Rameshan, R. Blume, M. Hävecker, A. Knop-Gericke, G. Rupprechter, B. Klotzter, J. Fleig, Ambient pressure XPS study of mixed conducting perovskite-type SOFC cathode and anode materials under well-defined electrochemical polarization, *J. Phys. Chem. C Nanomater Interfaces* 120 (2016) 1461–1471.

[83] H. Sun, Z. Xu, D. Zhang, L. Peng, X. Lai, Effects of charge rearrangement on interfacial contact resistance of  $\text{TiO}_2$ /graphite from first-principles calculations, *Appl. Surf. Sci.* 635 (2023), 157640.

[84] J. Kim, H. Choi, D. Kim, J.Y. Park, Operando surface studies on metal-oxide interfaces of bimetal and mixed catalysts, *ACS Catal.* 11 (2021) 8645–8677.

[85] X. Zheng, Y. Li, Y. Zheng, L. Shen, Y. Xiao, Y. Cao, Y. Zhang, C. Au, L. Jiang, Highly efficient porous  $\text{Fe}_x\text{Ce}_{1-x}\text{O}_{2-\delta}$  with three-dimensional hierarchical nanoflower morphology for  $\text{H}_2\text{S}$ -selective oxidation, *ACS Catal.* 10 (2020) 3968–3983.

[86] G. Li, K. Shen, L. Wang, Y. Zhang, H. Yang, P. Wu, B. Wang, S. Zhang, Synergistic degradation mechanism of chlorobenzene and  $\text{NO}_x$  over the multi-active center catalyst: the role of  $\text{NO}_2$ , Brønsted acidic site, oxygen vacancy, *Appl. Catal. B Environ.* 286 (2021), 119865.

[87] D. Cabaret, A. Bordage, A. Juhin, M. Arfaoui, E. Gaudry, First-principles calculations of X-ray absorption spectra at the K-edge of 3d transition metals: an electronic structure analysis of the pre-edge, *Phys. Chem. Chem. Phys.* 12 (2010) 5619–5633.

[88] L.E. Gevers, L.R. Enakonda, A. Shahid, S. Ould-Chikh, C.I.Q. Silva, P.P. Paalanen, A. Aguilera-Tapia, J.L. Hazemann, M.N. Hedhili, F. Wen, J. Ruiz-Martinez, Unraveling the structure and role of Mn and Ce for  $\text{NO}_x$  reduction in application-relevant catalysts, *Nat. Commun.* 13 (2022) 2960.

[89] Y. Liu, W. Sheng, Z. Wu, Synchrotron Radiation and Its Applications Progress in Inorganic Materials, 2021, p. 901.

[90] X. Wang, D. Liu, J. Li, J. Chen, H. Zhang, Clean synthesis of  $\text{Cu}_2\text{O}@\text{CeO}_2$  core@shell nanocubes with highly active interface, *NPG Asia Mater.* 7 (2015) e158–e158.

[91] M. Luo, J. Chen, L. Chen, J. Lu, Z. Feng, C. Li, Structure and redox properties of  $\text{Ce}_x\text{Ti}_{1-x}\text{O}_2$  solid solution, *Chem. Mater.* 13 (2001) 197–202.

[92] W. Zhu, X. Tang, F. Gao, H. Yi, R. Zhang, J. Wang, C. Yang, S. Ni, The effect of non-selective oxidation on the  $\text{Mn}_2\text{Co}_3\text{O}_8$  catalysts for  $\text{NH}_3$ -SCR: positive and non-positive, *Chem. Eng. J.* 385 (2020), 123797.

[93] L. Li, L. Zhang, K. Ma, W. Zou, Y. Cao, Y. Xiong, C. Tang, L. Dong, Ultra-low loading of copper modified  $\text{TiO}_2/\text{CeO}_2$  catalysts for low-temperature selective catalytic reduction of NO by  $\text{NH}_3$ , *Appl. Catal. B Environ.* 207 (2017) 366–375.

[94] Z.B. Xiong, X.K. Qu, Y.P. Du, C.X. Li, J. Liu, W. Lu, S.M. Wu, Selective catalytic reduction of  $\text{NO}_x$  with  $\text{NH}_3$  over cerium-tungsten-titanium mixed oxide catalyst: Synergistic promotional effect of  $\text{H}_2\text{O}_2$  and  $\text{Ce}^{4+}$ , *J. Mater. Res.* 35 (2020) 2218–2229.

[95] D. Meng, Q. Xu, Y. Jiao, Y. Guo, Y. Guo, L. Wang, G. Lu, W. Zhan, Spinel structured  $\text{Co}_3\text{Mn}_6\text{O}_8$  mixed oxide catalyst for the selective catalytic reduction of  $\text{NO}_x$  with  $\text{NH}_3$ , *Appl. Catal. B Environ.* 221 (2018) 652–663.

[96] J. Liu, X. Li, R. Li, Q. Zhao, J. Ke, H. Xiao, L. Wang, S. Liu, M. Tadé, S. Wang, Facile synthesis of tube-shaped Mn-Ni-Ti solid solution and preferable Langmuir-Hinshelwood mechanism for selective catalytic reduction of  $\text{NO}_x$  by  $\text{NH}_3$ , *Appl. Catal. A Gen.* 549 (2018) 289–301.

[97] L. Chen, J. Li, M. Ge, DRIFT study on cerium-tungsten/titania catalyst for selective catalytic reduction of  $\text{NO}_x$  with  $\text{NH}_3$ , *Environ. Sci. Technol.* 44 (2010) 9590–9596.

[98] X. Tang, Y. Shi, H. Yi, F. Gao, S. Zhao, K. Yang, R. Zhang, W. Ji, Y. Ma, C. Wang, Facile fabrication of nanosheet-assembled  $\text{MnCo}_2\text{O}_4$  hollow flower-like microspheres as highly effective catalysts for the low-temperature selective catalytic reduction of  $\text{NO}_x$  by  $\text{NH}_3$ , *Environ. Sci. Pollut. Res.* 26 (2019) 35846–35859.

[99] F. Liu, W. Shan, Z. Lian, L. Xie, W. Yang, H. He, Novel  $\text{MnWO}_4$  catalyst with remarkable performance for low temperature  $\text{NH}_3$ -SCR of  $\text{NO}_x$ , *Catal. Sci. Technol.* 3 (2013) 2699–2707.

[100] M.M. Azis, H. Härelind, D. Creaser, On the role of  $\text{H}_2$  to modify surface  $\text{NO}_x$  species over  $\text{Ag-Al}_2\text{O}_3$  as lean  $\text{NO}_x$  reduction catalyst: TPD and DRIFTS studies, *Catal. Sci. Technol.* 5 (2015) 296–309.

[101] G. Li, B. Wang, Z. Wang, Z. Li, Q. Sun, W.Q. Xu, Y. Li, Reaction mechanism of low-temperature selective catalytic reduction of  $\text{NO}_x$  over Fe-Mn oxides supported on fly-ash-derived SBA-15 molecular sieves: structure-activity relationships and *in situ* DRIFT analysis, *J. Phys. Chem. C* 122 (2018) 20210–20231.

[102] M.E. Bartram, R.G. Windham, B.E. Koel, Coadsorption of nitrogen dioxide and oxygen on platinum(111), *Langmuir* 4 (1988) 240–246.

[103] F. Liu, H. He, Y. Ding, C. Zhang, Effect of manganese substitution on the structure and activity of iron titanate catalyst for the selective catalytic reduction of NO with  $\text{NH}_3$ , *Appl. Catal. B Environ.* 93 (2009) 194–204.

[104] L. Chen, S. Ren, Y. Jiang, L. Liu, M. Wang, J. Yang, Z. Chen, W. Liu, Q. Liu, Effect of Mn and Ce oxides on low-temperature  $\text{NH}_3$ -SCR performance over blast furnace slag-derived zeolite X supported catalysts, *Fuel* 320 (2022), 123969.

[105] J. Xiang, L. Wang, F. Cao, K. Qian, S. Su, S. Hu, Y. Wang, L. Liu, Adsorption properties of NO and  $\text{NH}_3$  over  $\text{MnO}_x$  based catalyst supported on  $\gamma\text{-Al}_2\text{O}_3$ , *Chem. Eng. J.* 302 (2016) 570–576.

[106] H. Kubota, C. Liu, T. Toyao, Z. Maeno, M. Ogura, N. Nakazawa, S. Inagaki, Y. Kubota, K.-i Shimizu, Formation and reactions of  $\text{NH}_4\text{NO}_3$  during transient and steady-state  $\text{NH}_3$ -SCR of  $\text{NO}_x$  over H-AFX zeolites: spectroscopic and theoretical studies, *ACS Catal.* 10 (2020) 2334–2344.

[107] X. Tang, Y. Shi, F. Gao, S. Zhao, H. Yi, Z. Xie, Promotional role of Mo on  $\text{Ce}_{0.3}\text{FeO}_x$  catalyst towards enhanced  $\text{NH}_3$ -SCR catalytic performance and  $\text{SO}_2$  resistance, *Chem. Eng. J.* 398 (2020), 125619.

[108] C. Wang, X. Tang, H. Yi, F. Gao, S. Ni, R. Zhang, Y. Shi, MnCo nanoarray *in-situ* grown on 3D flexible nitrogen-doped carbon foams as catalyst for high-performance denitrification, *Colloids Surf. A Physicochem. Eng. Asp.* 612 (2021), 126007.

[109] M. Waqif, P. Bazin, O. Saur, J.C. Lavalle, G. Blanchard, O. Touret, Study of ceria sulfation, *Appl. Catal. B Environ.* 11 (1997) 193–205.

[110] H. Fu, X. Wang, H. Wu, Y. Yin, J. Chen, Heterogeneous uptake and oxidation of  $\text{SO}_2$  on iron oxides, *J. Phys. Chem. C* 111 (2007) 6077–6085.

[111] L. Wei, S. Cui, H. Guo, X. Ma, L. Zhang, DRIFT and DFT study of cerium addition on  $\text{SO}_2$  of manganese-based catalysts for low temperature SCR, *J. Mol. Catal. A Chem.* 421 (2016) 102–108.

[112] D. Tong, Y. Li, Z. Zhang, M. Li, B. Chen, X. Niu, Y. Zhu, Boosting resistance to  $\text{H}_2\text{O}$  and  $\text{SO}_2$  in low-temperature  $\text{NH}_3$ -SCR denitrification reaction by W addition in  $\text{Cu}_{0.1-m}\text{W}_m\text{TiO}_x$  ( $m = 0.05–0.09$ ) due to modulating the synergistic effect of oxidation property and acidity, *Fuel* 347 (2023), 128443.

[113] W. Wang, Y. Liu, T. Xue, J. Li, D. Chen, T. Qi, Mechanism and kinetics of titanium hydrolysis in concentrated titanyl sulfate solution based on infrared and Raman spectra, *Chem. Eng. Sci.* 134 (2015) 196–204.

[114] W. Xu, H. He, Y. Yu, Deactivation of a  $\text{Ce}/\text{TiO}_2$  catalyst by  $\text{SO}_2$  in the selective catalytic reduction of NO by  $\text{NH}_3$ , *J. Phys. Chem. C* 113 (2009) 4426–4432.

[115] C. Sun, H. Liu, W. Chen, D. Chen, S. Yu, A. Liu, L. Dong, S. Feng, Insights into the Sm/Zr co-doping effects on  $\text{N}_2$  selectivity and  $\text{SO}_2$  resistance of a  $\text{MnO}_x\text{-TiO}_2$  catalyst for the  $\text{NH}_3$ -SCR reaction, *Chem. Eng. J.* 347 (2018) 27–40.

[116] E. Ito, R.J. Ultermans, P.M. Lught, M.H.W. Burgers, M.S. Rigutto, H. van Bekkum, C.M. van den Bleek, Selective reduction of  $\text{NO}_x$  with ammonia over cerium-exchanged mordenite, *Appl. Catal. B Environ.* 4 (1994) 95–104.

[117] F. Li, C. Shi, X. Wang, G. Cui, D. Wang, L. Chen, The important role of oxygen defect for NO gas-sensing behavior of  $\alpha\text{-Fe}_2\text{O}_3$  (0 0 1) surface: Predicted by density functional theory, *Comput. Mater. Sci.* 146 (2018) 1–8.

[118] S. Wang, R. Ackermann, C.W. Spicer, J.D. Fast, M. Schmeling, J. Stutz, Atmospheric observations of enhanced  $\text{NO}_2\text{-HONO}$  conversion on mineral dust particles, *Geophys. Res. Lett.* 30 (2003).

[119] Y. Cheng, G. Zheng, C. Wei, Q. Mu, B. Zheng, Z. Wang, M. Gao, Q. Zhang, K. He, G. Carmichael, U. Pöschl, H. Su, Reactive nitrogen chemistry in aerosol water as a source of sulfate during haze events in China, *Sci. Adv.* 2 (2016), e1601530.

[120] C. Du, L. Kong, A. Zhanzakova, S. Tong, X. Yang, L. Wang, H. Fu, T. Cheng, J. Chen, S. Zhang, Impact of adsorbed nitrate on the heterogeneous conversion of  $\text{SO}_2$  on  $\alpha\text{-Fe}_2\text{O}_3$  in the absence and presence of simulated solar irradiation, *Sci. Total Environ.* 649 (2019) 1393–1402.